



Swansea University
Prifysgol Abertawe



Swansea University E-Theses

Filiform and pitting corrosion of aluminium alloys.

Holder, Adam Edward

How to cite:

Holder, Adam Edward (2011) *Filiform and pitting corrosion of aluminium alloys..* thesis, Swansea University.
<http://cronfa.swan.ac.uk/Record/cronfa42994>

Use policy:

This item is brought to you by Swansea University. Any person downloading material is agreeing to abide by the terms of the repository licence: copies of full text items may be used or reproduced in any format or medium, without prior permission for personal research or study, educational or non-commercial purposes only. The copyright for any work remains with the original author unless otherwise specified. The full-text must not be sold in any format or medium without the formal permission of the copyright holder. Permission for multiple reproductions should be obtained from the original author.

Authors are personally responsible for adhering to copyright and publisher restrictions when uploading content to the repository.

Please link to the metadata record in the Swansea University repository, Cronfa (link given in the citation reference above.)

<http://www.swansea.ac.uk/library/researchsupport/ris-support/>



Swansea University
Prifysgol Abertawe

**Filiform and Pitting Corrosion of
Aluminium Alloys**

Adam Edward Holder

Submitted to the University of Wales in fulfilment of the
requirements for the degree of Doctor of Engineering

2011



ProQuest Number: 10821384

All rights reserved

INFORMATION TO ALL USERS

The quality of this reproduction is dependent upon the quality of the copy submitted.

In the unlikely event that the author did not send a complete manuscript and there are missing pages, these will be noted. Also, if material had to be removed, a note will indicate the deletion.



ProQuest 10821384

Published by ProQuest LLC (2018). Copyright of the Dissertation is held by the Author.

All rights reserved.

This work is protected against unauthorized copying under Title 17, United States Code
Microform Edition © ProQuest LLC.

ProQuest LLC.
789 East Eisenhower Parkway
P.O. Box 1346
Ann Arbor, MI 48106 – 1346

Abstract

The aim of this work is to investigate the localised corrosion behaviour of aluminium alloy AA6111 and the relationship between artificial ageing and corrosion susceptibility for the alloy.

Filiform corrosion (FFC) on AA6111 is investigated in the first chapter. Scanning Kelvin Probe (SKP) potentiometry is used to measure the effect of artificial ageing and the presence of a deformed surface layer on the open circuit potential of the bare surface of AA6111 sheet in humid air. The SKP is then used to follow the kinetics of chloride-induced FFC and to map the evolving potentials which are characteristic of the FFC localised corrosion cell. It was shown that abrasion of AA6111 introduces a deformed surface layer which exhibits a significantly more negative potential than the bulk alloy. When FFC is initiated on polymer coated AA6111 in the presence of the deformed surface layer the observed attack is rapid and superficial; a slower and more deeply penetrating attack occurs in its absence. AA6111 is relatively resistant to FFC in the T4 temper but susceptibility increases as a result of artificial ageing.

In the second chapter the methods used to initiate and propagate FFC in the first chapter were adapted and then evaluated on their ability to predict the FFC performance of a set of coated architectural aluminium sheet products. The method is shown to perform well when compared to standard accelerated corrosion tests.

In the final chapter the Scanning Vibrating Electrode Technique (SVET) is used to investigate the localised corrosion of AA6111 in the T4 condition and after artificial ageing for between 0.17 and 56 hours at 185°C. Pitting corrosion was the dominant corrosion type. AA6111 is shown to be relatively resistant to pitting corrosion in the T4 temper but susceptibility increases as a result of artificial ageing.

Declaration

This work has not previously been accepted in substance for any degree and is not being concurrently submitted in candidature for any degree.

Signed

Date: 07/07/11

STATEMENT 1

This thesis is the result of my own investigations, except where otherwise stated. Where correction services have been used, the extent and nature of the correction is clearly marked in a footnote(s).

Other sources are acknowledged by giving explicit references. A bibliography is appended.

Signed

Date: 07/07/11

STATEMENT 2

I hereby give consent for my thesis, if accepted, to be available for photocopying and for inter-library loan, and for the title and summary to be made available to outside organisations.

Signed

Date: 07/07/11

Acknowledgements

Thanks to Professor Neil McMurray, Dr Geraint Williams and Dr Andrew Coleman for their supervision and help in completing this work.

Thanks to my family and friends for their patience and support.

Contents

Chapter 1: Introduction and Literature Review.....	7
1.1 Aluminium	7
1.1.1 Primary Aluminium Production.....	7
1.1.2 Recycling.....	9
1.1.3 Alloying.....	9
1.1.4 Alloy Designations.....	12
1.1.5 Processing.....	14
1.2 Aluminium Alloy AA6111.....	21
1.3 Corrosion.....	25
1.3.1 Electrochemistry.....	25
1.4 Corrosion of Aluminium and its Alloys.....	33
1.4.1 Oxide layer.....	33
1.4.2 Intergranular Corrosion.....	35
1.4.3 Pitting Corrosion.....	36
1.4.4 Filiform Corrosion.....	39
1.5 Heat Treatment, Precipitation and their Effect on Corrosion.....	43
1.6 Deformed Surface Layers	63
1.6.1 Morphology	63
1.6.2 Formation	65
1.6.3 Thermal Stability	66
1.6.4 Precipitation in the DSL and Corrosion Susceptibility	66
1.6.5 Etching.....	69
1.7 Environment.....	69
1.7.1 Humidity	70
1.7.2 Oxygen.....	70
1.7.3 Temperature.....	70
1.7.4 pH	71
1.7.5 Electrolyte	71
1.8 Standard Accelerated Filiform Corrosion Tests.....	71
1.9 Electrochemical Techniques.....	73
1.9.1 Scanning Vibrating Electrode Technique.....	74

1.9.2	Scanning Kelvin Probe	76
Chapter 2:	Filiform Corrosion of Aluminium Alloy AA6111.....	79
2.1	Introduction.....	79
2.2	Experimental Procedure.....	82
2.2.1	Materials.....	82
2.2.2	Preparation of Samples	83
2.2.3	Time-Lapse Photography.....	86
2.2.4	Polarisation Measurements	87
2.2.5	Defects.....	87
2.2.6	Initiation	88
2.2.7	Scanning Kelvin Probe	88
2.2.8	Scanning Electron Microscopy	95
2.3	Results and Discussion	95
2.3.1	Optical Time-lapse Photography	95
2.3.2	SKP Potentiometric Characterisation of Intact AA6111 Surfaces	99
2.3.3	Potentiodynamic Polarisation Experiments	107
2.3.4	SKP Potentiometry of FFC on DSL Bearing AA6111.....	113
2.3.5	SKP Potentiometry of FFC on Bulk AA6111	119
2.3.6	Filiform Corrosion Kinetics	126
2.3.7	Mechanism of Surface Active FFC	128
2.3.8	Mechanism of Successive Pitting FFC.....	131
2.3.9	Filiform Corrosion on Pure Aluminium.....	133
2.4	Conclusions.....	134
Chapter 3:	Accelerated Corrosion Testing	136
3.1	Introduction.....	136
3.2	Experimental	137
3.2.1	Materials.....	137
3.2.2	Accelerated Applied Acid Test.....	138
3.2.3	Outdoor Field Test.....	141
3.2.4	Cyclic Cabinet Test.....	141
3.2.5	Lockheed Test.....	142
3.3	Results and discussion.....	142
3.3.1	Preliminary Test Results	142
3.3.2	Test Evaluation Criteria	144

3.4	Conclusions.....	160
Chapter 4:	Localised Corrosion of Aluminium Alloy AA6111	161
4.1	Introduction.....	161
4.2	Experimental	163
4.2.1	Materials.....	163
4.2.2	Heat Treatments.....	163
4.2.3	Grinding and Polishing.....	163
4.2.4	Hardness Measurements	163
4.2.5	Scanning Vibrating Electrode Technique.....	164
4.2.6	SVET Experiments.....	167
4.2.7	SVET Current Flux Detection	168
4.2.8	Total Equivalent Aluminium Loss Calculation	169
4.3	Results and discussion.....	170
4.3.1	SVET Output Analysis	170
4.3.2	Hardness.....	172
4.3.3	Corrosion Morphology	172
4.3.4	Corrosion Kinetics.....	175
4.3.5	Influence of ageing on susceptibility.....	182
4.3.6	Microscopy	186
4.4	Conclusions.....	188

Chapter 1: Introduction and Literature

Review

1.1 Aluminium

Aluminium is the most abundant metallic element in the earth's crust and has been widely used in engineering for over one hundred years. A viable method for extraction from its ore was developed towards the end of the 19th century. The development of the automotive industry, the electricity network and later the aeronautical industry created a significant market for aluminium and its alloys.

1.1.1 Primary Aluminium Production

1.1.1.1 Mining

Aluminium very rarely occurs as a free metal because of its reactivity. It occurs in ores of aluminium hydroxide, in particular bauxite. Bauxite deposits are formed when the more soluble components of rock leach out as it weathers leaving behind the less soluble components. Heavy rainfall is required for this process to occur so tropical and sub-tropical regions tend to be the best sources. Around 80% of bauxite comes from surface mining of blanket mines, the remaining 20% is from underground excavation. The bauxite is usually of an acceptable quality when mined in this way and does not require extensive processing; generally all that is needed is the removal of clay. The bauxite used for the production of aluminium typically contains 35 to 60% aluminium oxide.

1.1.1.2 Refining

The next stage is to produce alumina from the bauxite. This is done using the Bayer process [1] which starts with the dissolution of bauxite in sodium hydroxide at high pressure and temperature. The solution that remains consists of sodium aluminate and undissolved bauxite residues which contain iron, silicon and titanium. These bauxite residues sink to the bottom of the tank and are then removed. The sodium aluminate solution from the top of the tank is pumped into a precipitator where fine alumina particles are added. These particles sink to the bottom of the precipitator tank and are transferred to a calciner. Within the calciner, which is essentially a rotary kiln, temperatures of around 1100°C are used to drive off the chemically combined water. The result of this process is alumina in the form of a pure white powder.

1.1.1.3 Smelting

The final stage in aluminium production is smelting. This is done by the electrolytic Hall-Heroult process [1, 2]. The alumina is dissolved in an electrolyte of molten sodium aluminium fluoride known as cryolite. This is done within a large carbon lined steel container, the 'pot'. Electricity from a low voltage but very high current source is passed through the cryolite between a carbon anode and the carbon lining of the pot. The alumina is reduced during the process allowing pure, molten aluminium to gather at the bottom of the pot. This is then siphoned off, taken to a holding furnace and cleaned before casting.

Around 15kWh are required to produce each kilogram of aluminium from alumina. This is a large improvement on the 20kWh required half a century ago but it still adds a significant amount to the cost of production and to the impact on the environment [1]. Smelting facilities are usually located where there is an abundant and inexpensive source of electricity such as near a hydroelectric power station and

often power will be generated specifically for the purpose. The aluminium produced by the normal production process has a purity of between 99% and 99.9%, the remainder is made up of impurity elements such as iron and silicon. For special applications purities of up to 99.99% may be required and further refinement processes are available to accommodate this [2].

1.1.2 Recycling

Recycling is the alternative to mining, refining and smelting. This method of obtaining the metal is used wherever possible because it uses only 5% of the energy required to produce virgin aluminium. It is partly due to the low melting point of 660°C that recycling of aluminium is so energy efficient. Aluminium beverage cans are easy and economical to recycle with some countries achieving extremely high can recycling rates (92% in Sweden [1]). Levels of normal alloying elements such as iron, silicon and copper are usually higher in secondary aluminium as are levels of contaminant elements such as lead, bismuth, zinc and tin [3]. These levels can be controlled to some extent by adjusting the amount of waste aluminium being taken from certain sources. For many applications secondary aluminium can be applied just as successfully as primary aluminium.

1.1.3 Alloying

Pure aluminium has a low density of 2.7g/cm^3 which is approximately a third of that of steel, but a tensile strength of about 90 Mpa, this can be increased to around 180 MPa by cold rolling. The corrosion resistance is high and it is a good conductor of both heat and electricity. It is highly reflective and has an attractive appearance. It is non-toxic, recyclable and easily fabricated [2]. Despite these valuable attributes, its commercial application is limited by its relatively low strength. Its main uses in the pure form are in fields such as cryo-electrics, cryo-magnetics and the manufacture of semi-conductors. Strength can be increased significantly by alloying the

aluminium with small amounts of other elements and this gives rise to a much wider range of applications [4].

There are a number of elements which can be added to aluminium to improve its strength and other mechanical and physical properties. Some common additions and their effects are detailed below. [2, 4, 5]

1.1.3.1 Silicon

Silicon is an impurity in electrolytically produced primary commercial aluminium at levels of around 0.01% to 0.15% but can also be an alloying addition. It combines with magnesium to produce magnesium silicide (Mg_2Si) in the heat-treatable AA6000 series alloys; a metastable form of this phase is often the main hardening phase in these alloys. Silicon also improves corrosion resistance in most aluminium alloys. It also helps with casting as it improves the fluidity of the molten alloy and reduces susceptibility to hot-crevicing.

1.1.3.2 Iron

Iron is an impurity element in aluminium, it has high solubility in the molten state. When solid the solubility drops to just 0.04%, so most of the iron in aluminium comes out of solution and combines with aluminium or with alloying elements to produce intermetallic second phase particles.

1.1.3.3 Manganese

Manganese is an impurity element in primary aluminium in trace amounts but is also an addition to some alloys. In solid solution or as a finely precipitated intermetallic phase it will increase the strength of the alloy. Manganese can cause a decrease in ductility and it is often limited to 1% for this reason. In copper containing alloys such as those in the AA6000 series it raises the recrystallisation temperature.

1.1.3.4 Magnesium-Silicon

Magnesium and silicon are added to the AA6000 series alloys in quantities of up to 1.5%. They are often added in the approximate ratio of 1.73wt.% magnesium to 1wt.% silicon to produce Mg_2Si (this ratio is the equivalent of 2 magnesium atoms to 1 silicon atom). The maximum solubility of this phase is 1.85wt.%. The age hardening process leads to precipitation of Guiner-Preston zones which develop into very fine precipitates, both of which will increase the strength of the alloy.

1.1.3.5 Chromium

Chromium is present in commercial purity aluminium in trace amounts but even in quantities as small as 5 ppm it has a large effect on electrical resistivity. Chromium diffuses slowly and in wrought alloys will form phases in fine dispersions which inhibit the nucleation and growth of grains. Chromium can therefore be used to control microstructure by preventing grain growth or recrystallisation.

1.1.3.6 Nickel

When more than 0.04% nickel is added to aluminium it begins to form insoluble intermetallic particles because this is beyond its limit of solid solubility. These intermetallics decrease the ductility of the alloy but increase its strength as long as the addition is no more than 2%. Nickel additions to aluminium-copper and aluminium-silicon systems are used to improve the retention of strength and hardness at elevated temperatures. Nickel also decreases the coefficient of thermal expansion.

1.1.3.7 Copper

Copper is an important addition to aluminium alloys because of its high solubility and its contribution to the alloy's strength. Copper is sometimes added as a major alloying addition up to around 10wt%. This allows strength to increase by

precipitation hardening. It can also be used in smaller quantities in combination with other alloying elements such as magnesium and silicon. Generally the presence of copper in an alloy is detrimental to its corrosion properties; it tends to precipitate at grain boundaries increasing susceptibility to intergranular corrosion, pitting corrosion, stress corrosion and filiform corrosion.

1.1.4 Alloy Designations

Alloys are classified according to their major alloying additions and into two main groups, wrought and cast. The alloys studied in this thesis are wrought alloys and so the wrought alloy series along with their major alloying elements, main properties and applications are specified in Table 1.1 below.

Table 1.1 Wrought aluminium series designations with their major alloying additions, properties and applications [5, 6]

Series	Primary Alloying Elements	Properties	Applications
1000	None	Easily fabricated, corrosion resistant, high thermal and electrical conductivity, low strength and hardness.	Chemical, electrical, lithography.
2000	Copper	Heat treatable, high strength, non-weldable, poor corrosion resistance.	Aircraft.
3000	Manganese	Non heat-treatable, medium strength, easily fabricated and corrosion resistant.	Architectural, kitchen utensils.
4000	Silicon	Low melting point without brittleness, generally not heat treatable.	Machined parts, welding wire and brazing sheet, architectural.
5000	Magnesium	Hard, good weldability, good corrosion resistance in marine environments.	Automotive, marine environments.
6000	Magnesium and Silicon	Heat treatable, medium strength, good weldability and corrosion resistance.	Automotive, architectural extrusions.
7000	Zinc	Heat treatable, very high strength, poor corrosion resistance, non weldable.	Armoured vehicles, military bridges, aircraft structural components, motorcycles.
8000	Lithium, Tin, Iron and others	Dependent on alloying elements	Nuclear applications, bearings.

1.1.5 Processing

1.1.5.1 Rolling

Hot and cold rolling procedures that are carried out on aluminium produce a product with a thickness of between 0.006mm and 250mm. The sheet used for automotive skin panels is between these two extremes at about 1.0 to 1.6mm. All of these rolled products are rolled from a slab that is cast after smelting. Initially the cast slabs are heated to around 500°C and then they are passed through the rolling mill until they reach the required thickness. For products requiring a thickness of less than 3mm, the sheet will be rolled into coils before further reductions are applied. From this stage onwards cold rolling mills are used and annealing processes are applied where necessary to achieve the required temper condition.

The rolling process alters the microstructure and therefore the mechanical properties of aluminium, the degree of this change depends on the reduction and heat treatment applied during the rolling process [7]. Cold rolling usually results in an increase in the strength of the material as a result of work hardening.

1.1.5.2 Heat treatment and Precipitation

The heat treatable alloys contain soluble alloying elements that exceed the equilibrium solid solubility limit at, and slightly above, room temperature. Large increases in strength can, in some cases, be obtained by precipitation heat treatment. As a result of precipitation heat treatment, the alloy will ideally contain a high concentration of fine precipitated particles which impede the movement of dislocations.

In order for an alloy to be precipitation hardenable the solute element needs to have decreasing solubility with decreasing temperature. The binary phase diagram for aluminium and copper (Figure 1.1) shows a solvus with a positive slope i.e. the

solid solubility of copper decreases with decreasing temperature so we can take this as an example.

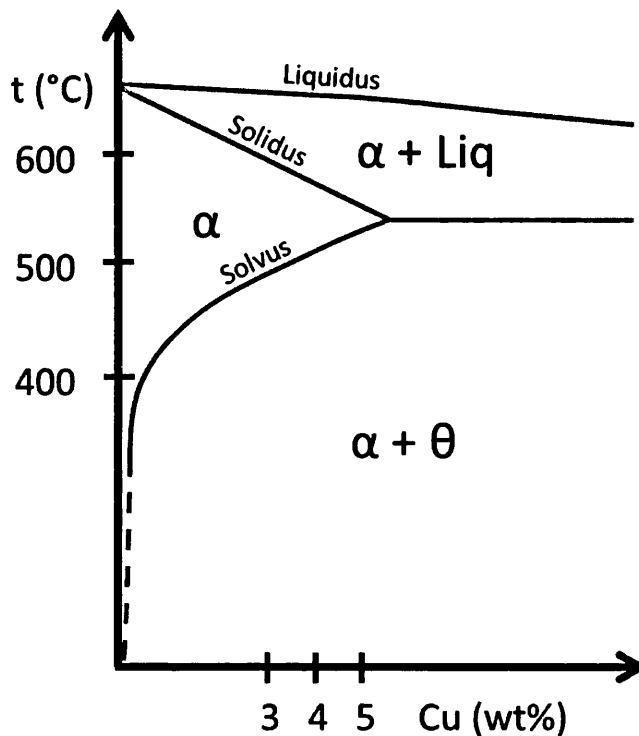


Figure 1.1 Schematic of the low copper portion of the Al-Cu equilibrium phase diagram modified from Murray [8]

Precipitation hardening is a three stage process. The first step is called solutionising which involves heating the alloy to a temperature between the solvus and the solidus. This produces a uniform solid solution of the copper in aluminium (α). Once the alloy has been held at the elevated temperature for long enough for this to have occurred, the second step, quenching is performed. Quenching involves rapid cooling of the alloy, usually to room temperature. The fast rate of change of temperature means that the behaviour of the alloy is not as predicted by the equilibrium phase diagram because there isn't time for the diffusion necessary for the precipitation of the second phase (θ). At room temperature the alloy consists of a supersaturated solid solution (SSSS). The final step of the process is ageing, this involves heating the alloy and holding it at an intermediate temperature (still below

the solvus) at which diffusion occurs at a rate sufficient for the formation of fine precipitates of the second phase. The precipitation of second phase particles is dependent upon both temperature and the length of time the alloy is held at that temperature. Figure 1.2 shows the development of second phase particles in an alloy when it is held at a constant and elevated temperature and the relationship between the ageing time and the alloy's strength and hardness.

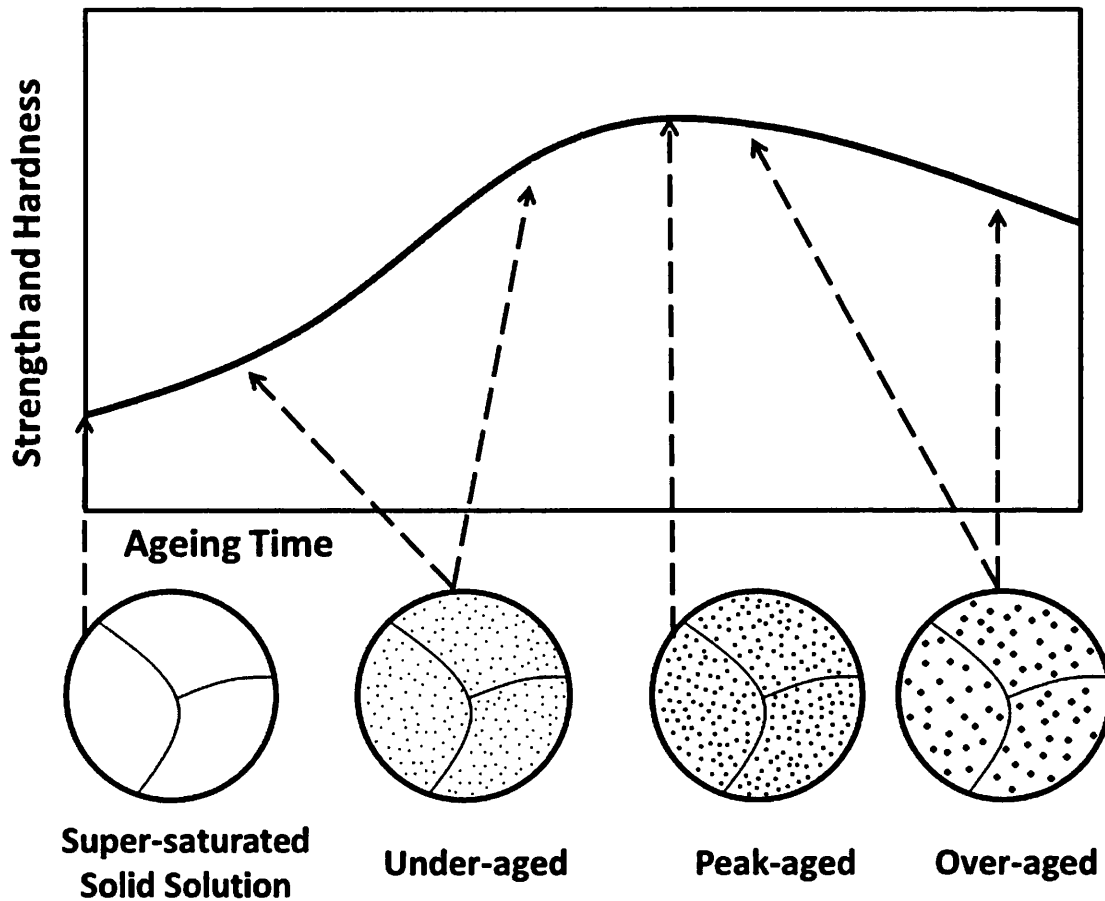


Figure 1.2 Schematic showing the development of precipitates and change in hardness in a heat treatable alloy as a result of ageing

Initially the alloy is a supersaturated solid solution and the hardness is relatively low. Once ageing begins small and under-developed precipitates will form. The alloy is then regarded as 'underaged' until the precipitates reach the optimum size and distribution for strengthening, and the alloy is said to be 'peak aged'. Peak ageing is as a result of the optimum number, size and distribution of intermediate

metastable precipitates forming. With further ageing the precipitates coalesce and coarsen and the alloy loses strength; it is now termed 'overaged'.

Different phases will form during ageing depending on the heat treatment temperature. Each phase has a range of temperatures at which it will form and outside of which it will be unstable.

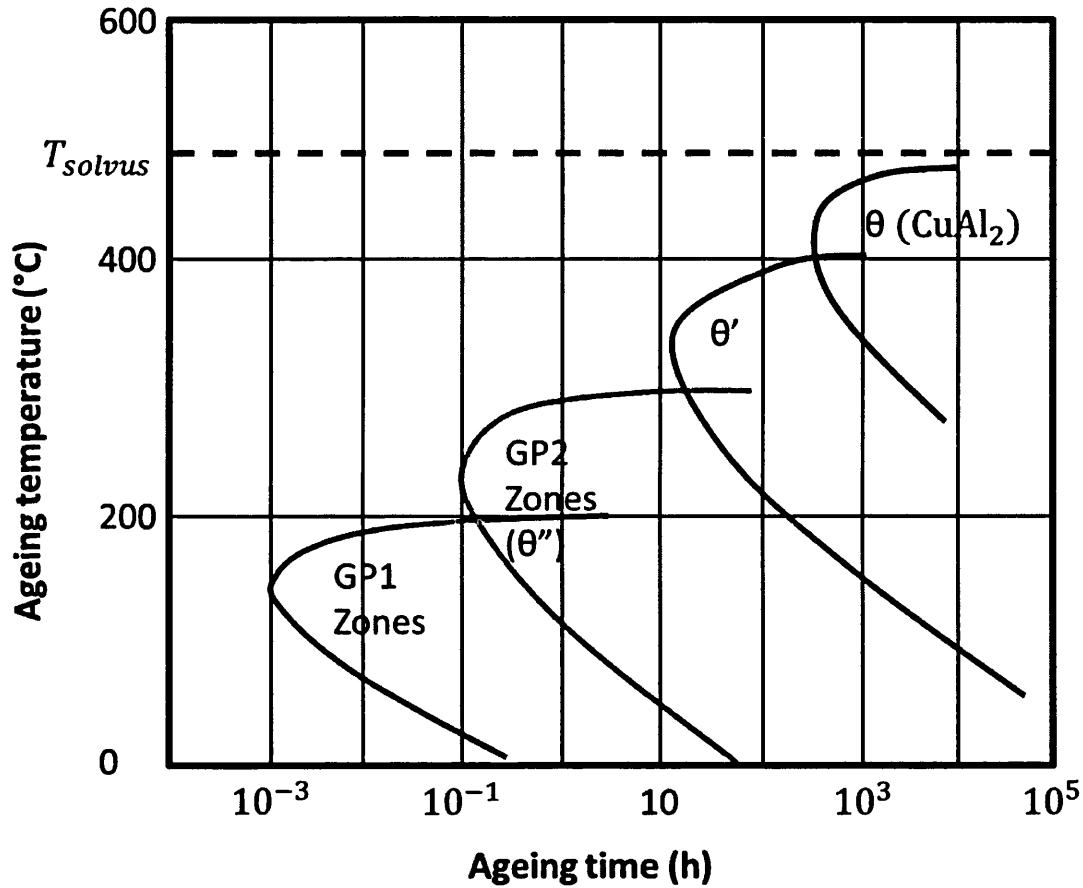


Figure 1.3 Time Temperature Transformation (TTT) diagram for a binary Al-Cu alloy.

Figure 1.3 is a time, temperature, transformation (TTT) diagram for a hypothetical binary aluminium-copper alloy. This shows the phases which should be present in the alloy for an ageing treatment at a certain temperature for a certain time. The first phases, which form as the alloy begins to age, are fully coherent with the matrix and have low interfacial energy; these are known as GP zones. They are also disc shaped and their orientation relative to the matrix lattice is such as to minimise

their strain energy. The first GP zone, GP1 is followed by GP2 (θ'') and θ' , these are known as the transition phases, finally the equilibrium $CuAl_2$ phase, θ forms replacing the transition phases. As the precipitation sequence progresses from GP1 to θ , the level of coherence decreases and the energy barrier to nucleation increases. θ has a crystal structure which is incoherent with the matrix and therefore the interfaces between the θ phase and the matrix are high energy and the energy barrier to nucleation is high. Despite being the equilibrium phase, θ requires the most energy to form and so precipitates of this phase are the last to form.

1.1.5.2.1 Temper Designations

Temper designations are associated with particular thermo-mechanical protocols. The designations have the format of a 'T' followed by a one or two digit number, these are shown in Table 1.2.

Table 1.2 Temper designations [9]

Temper Designation	Treatment Sequence
T1	Cooled from an elevated temperature shaping process and naturally aged to a substantially stable condition.
T2	Cooled from an elevated temperature shaping process, cold worked and naturally aged to a substantially stable condition.
T3	Solution heat treated, cold worked and naturally aged to a substantially stable condition.
T4	Solution heat treated and naturally aged to a substantially stable condition.
T5	Cooled from an elevated temperature shaping process and then artificially aged.
T6	Solution heat treated and then artificially aged.
T7	Solution heat treated and stabilised.
T8	Solution heat treated, cold worked and then artificially aged.
T9	Solution heat treated, artificially aged and then cold worked.
T10	Cooled from an elevated temperature shaping process, cold worked and then artificially aged.

1.1.5.3 Surface Treatments

A series of surface treatments is carried out to provide a stable surface layer to protect the alloy from corrosion.

Anodising is an electrolytic conversion process which enhances the natural oxide layer on aluminium. Fast anodising in sulphuric or phosphoric acid can be applied as a coil line treatment [3].

An alternative to electrolytic conversion is chemical conversion in which the aluminium surface oxide is replaced by a salt-like amorphous or crystalline layer. Traditionally this is based on hexavalent chromium, Cr^{6+} , resulting in a film which has a self-healing ability when scratched or otherwise damaged and this therefore provides excellent corrosion protection. Hexavalent chromium is now restricted by legislation because of its toxic and carcinogenic nature and so alternatives have been, and are being, developed.

Chrome-free alternatives based on fluorotitanic and fluorozirconic acid can provide a good surface coverage of titanium oxide or zirconium oxide and these layers also provide good paint adhesion and corrosion protection. These treatments can work well but controlling them can be more difficult than controlling traditional chrome-based treatments and fluoride itself is a very aggressive and toxic substance.

Another chemical conversion process is zinc-phosphatisation whereby a dense layer of zinc-phosphate crystals is formed on the surface.

An alternative to conversion processes is organic film deposition where a coating such as silane is applied to the surface. These coatings work well providing there is a good bond between the aluminium and the film and this is achieved by ensuring the aluminium surface is in a well cleaned initial condition.

Paint finishing is the final stage of surface treatment, providing barrier protection and an attractive appearance. The paint finish may consist of a number of layers of

different products; for example a primer, a sealer and a topcoat are often used for automotive body panels.

1.2 Aluminium Alloy AA6111

AA6111 is an aluminium alloy with major alloying additions of magnesium, silicon and copper. This thesis details work on both the filiform corrosion and the pitting corrosion of this material. The composition limits are shown in Table 1.3 as weight percentages. Other elements should not exceed 0.05 wt% each or a total of 0.15wt%.

Table 1.3 Composition of AA6111

Si	Fe	Cu	Mn	Mg	Cr	Zn	Ti	Al
0.6-1.1	0.40	0.50-0.9	0.10 - 0.45	0.50 - 1.0	0.10	0.15	0.10	Bal.

Aluminium alloys of the AA6000 series Al-Mg-Si-(Cu) are now being used extensively in the manufacture of automotive body panels. The reason for their increased popularity is the need for improved fuel efficiency and reduced emissions by reducing vehicle weight. At the same time these alloys provide sufficient strength to meet quality and safety requirements. Replacing steel with aluminium in the body-in-white (BIW) can reduce its weight by up to 47%. Further weight reductions can be realised because lighter suspension, brake and engine components are required to achieve the same level of performance [10]. For automotive body panels the most important qualities are a good balance between initial formability and strength after paint baking as well as a high surface quality after pressing and a good paint finish; AA6000 series alloys fit these criteria well [11].

AA6000 series alloys are initially direct chill (DC) cast into ingots which are approximately 600mm thick, around 2m wide and up to 9m long. Their rolling

surfaces are then scalped to remove the outer layer which is physically and compositionally irregular. The ingots are then homogenised at 500°C or higher and held at this temperature to get rid of any coring effects and to dissolve the soluble phases present. Homogenisation can take up to 48 hours [12]. The hot ingots are then transferred to the hot rolling mills. Typically a four-high single reversing breakdown mill is used to reduce the ingot to a slab of thickness 25-40mm; this is known as the transfer gauge. Next a tandem hot rolling mill reduces the thickness to a few millimetres so that it can be rolled into a coil. [10, 12, 13]. Finally the sheet is allowed to cool before being cold-rolled to its final gauge; for automotive sheet this is approximately 1mm. Cold rolling leads to a work hardening effect which reduces the formability of the material and so it is sometimes necessary to introduce annealing sessions to allow recrystallisation to occur to achieve the required product specifications [13]. Automotive aluminium sheet of heat-treatable alloys such as AA6111 and AA6016 is subsequently solution heat treated to obtain good formability and maximise its potential for age hardening [12]. The sheet is unwound from the coil and passed through a continuous annealing line as a single sheet where the furnace can heat it to the solutionising temperature of around 540°C very rapidly. The sheet is then quenched on-line.

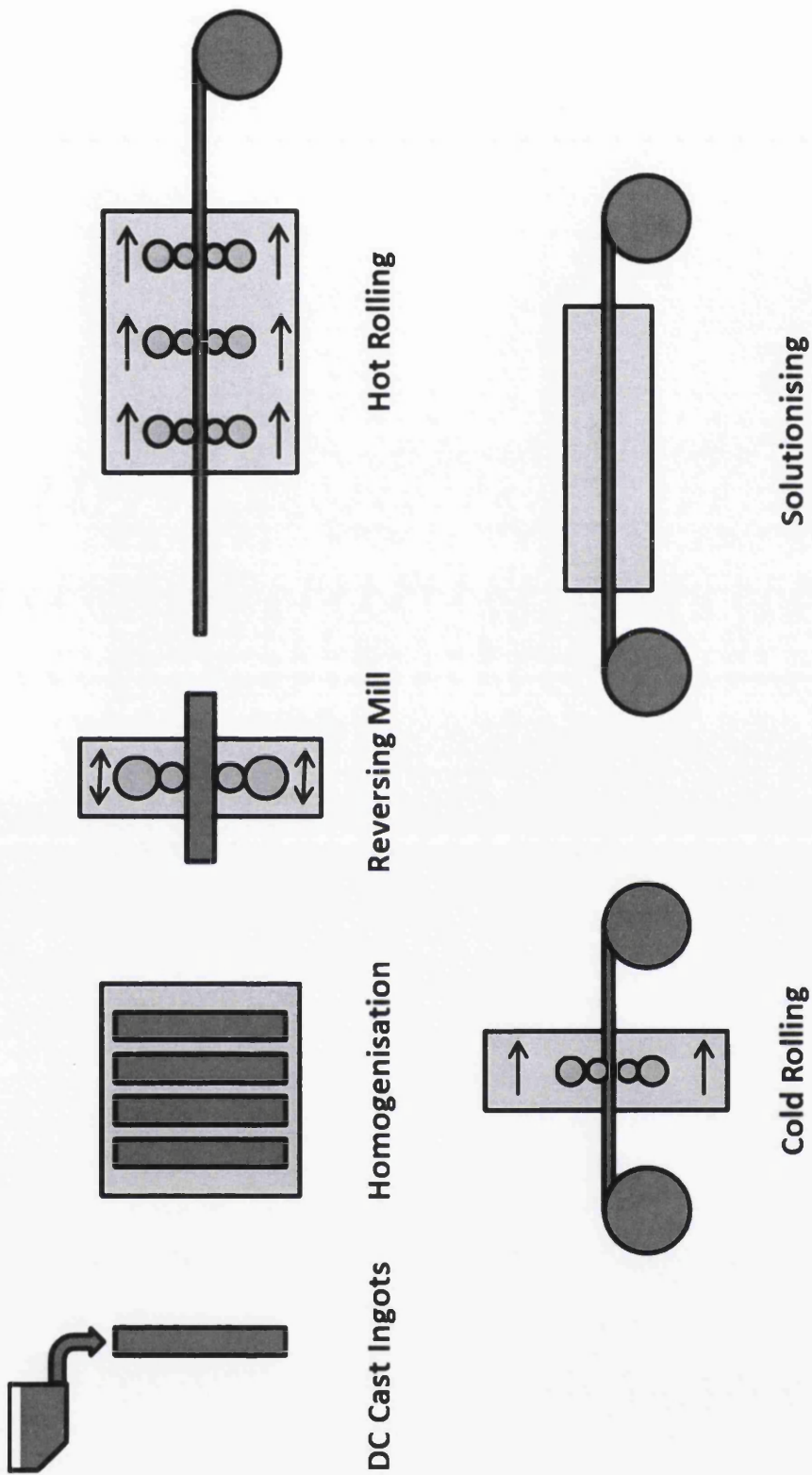


Figure 1.4 Typical processing route for automotive sheet of the heat treatable alloy AA6111

Aluminium alloys generally have lower ductility, lower R-value and lower Young's modulus than steels [14] so the automotive manufacturer needs to modify their forming procedures to suit aluminium. If the same methods and shapes used for steel sheet are applied to aluminium sheet then it can be vulnerable to tearing, cracking and spring-back. One example of a novel forming method suited to aluminium is high temperature blow-forming where an increase in ductility is achieved by heating the material. This method has been successfully applied to the manufacture of small batches of panels such as the front fender of the Honda Legend [15].

Ageing occurs after forming during the thermal curing of the paint; this is known as the paint bake process. This process consists of heating the formed product to between 160°C and 200°C for 20 to 30 minutes. In North America where panel gauges are around 1mm or less, the aluminium alloy of choice is AA6111. In the T4 temper, AA6111 has a strength of around 150MPa which increases to around 220MPa as a result of the paint baking process. In Europe panel gauges are generally thicker and so the lower strength AA6016 alloy is preferred. The strength of AA6016 in the T4 temper is around 120MPa and its strength increases to around 190MPa after the paint baking process [16]. The age hardening potential of these alloys is, however, not fully exploited by the paint bake process [17]. Much longer heat treatments would usually be required to reach the peak hardness (T6) condition. The main reason for the higher strength of AA6111 is that it contains much more copper (0.5-0.9wt%) than AA6016 however this is also the main cause of its inferior corrosion resistance.

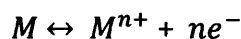
1.3 Corrosion

Corrosion can be defined as the reaction of a solid with its environment; this is sometimes restricted to those reactions which result in a deterioration of the properties of the material [18]. Corrosion is most commonly associated with metals. Corrosion can lead to mechanical failure but can also cause failure by causing an unacceptable level of cosmetic damage to a product. There is a vast global economic loss associated with corrosion which is made up of the cost of prevention, repair and replacement as well as lost revenues.

1.3.1 Electrochemistry

Almost all metals will naturally form an oxide layer when exposed to air. These oxides will usually dissolve in aqueous solutions but the solubility depends on the metal, the nature of the oxide layer and also the pH of the solution. Lower pH solutions will more easily dissolve the oxide than those with a more neutral pH. Until it is dissolved the oxide layer acts as a barrier to prevent dissolution of the metal surface and therefore has a large influence on corrosion. When a metal is being protected by an oxide layer it is said to be in a passive state. When the oxide layer breaks down and the bare metal is exposed to the solution it is said to be active because corrosion begins. Metal cations will go into solution leaving excess electrons in the metal, this can be represented as:

Equation 1.1:



The metal, M has no charge until a metal cation, M^{n+} goes into solution leaving n excess electrons behind in the metal. The accumulation of excess electrons in the metal and excess cations in the solution results in an increasing potential difference between the metal and the solution which is known as the electrode potential. The presence of the electrode potential slows the dissolution of the metal and causes

the redeposition of metal cations back onto it. Eventually the rates of the forward reaction (dissolution of the metal) and the reverse reaction (the redeposition of metal cations) become equal. The potential at this point is termed the reversible potential, E_r . The value of E_r is given by the following equation.

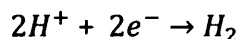
Equation 1.2:

$$E_{r.M^{n+}/M} = E_{M^{n+}/m}^0 + \frac{RT}{nF} \log a_{M^{n+}}$$

Here R is the gas constant, T is the absolute temperature, F is the Faraday constant, n is the number of electrons transferred for every metal cation dissolved and $a_{M^{n+}}$ is the activity of the dissolved metal cations. When the potential reaches E_r , there is no further net dissolution of metal.

In most real situations the potential of the metal does not drop down to the reversible potential, it remains more positive because other reactions take excess electrons away from the metal. In acidic solutions electrons react with adsorbed hydrogen cations to liberate hydrogen gas by the following reaction:

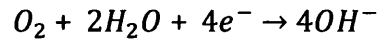
Equation 1.3



Because the above hydrogen evolution reaction accepts excess electrons it allows the metal dissolution reaction to continue. Hydrogen evolution is also a reversible reaction and the reversible potential for hydrogen evolution will be reached at a certain partial pressure of hydrogen. In most circumstances hydrogen can escape from the system so the partial pressure of hydrogen will not increase and the potential continues to be more negative than the reversible potential for hydrogen evolution. This means that there will continue to be a reduction of hydrogen cations and so the oxidation of the metal can continue to occur.

When the solution is neutral the rate of hydrogen evolution (Equation 1.3) is so low that it does not influence the overall corrosion process significantly. Instead excess electrons are consumed by a reaction that produces hydroxyl ions:

Equation 1.4:



Here electrons react with oxygen that has adsorbed onto the metal surface from the solution and the water to produce hydroxyl ions. The reversible potential for this reaction is not normally reached. The potential is usually more negative than the reversible potential and so the reaction can continue.

In summary; the net dissolution of the oxide-free surface of a metal in an aqueous solution will proceed until the reaction reaches equilibrium with the reverse reaction (at the reversible potential) however this equilibrium is usually avoided because another reaction occurs which consumes electrons. In an acidic solution this reaction is often the evolution of hydrogen and in a neutral solution it will often be the production of hydroxyl ions.

The dissolution of metal is an oxidation reaction, it involves a loss of electrons, and the areas of the surface of the metal where this is occurring are called anodes. Hydrogen evolution and hydroxyl ion production are both reduction reactions, they involve a gain of electrons. The areas of the surface of the metal where these reactions occur are called cathodes. The high electrical conductivity of metals allows electrons to move from anodes to cathodes so that the anodes and cathodes can occur in separate locations. It is the distribution of anodes and cathodes that defines two distinct classes of corrosion, localised corrosion and general corrosion. Where anodes and cathodes can be seen to be at separate locations, localised corrosion is occurring, otherwise it is general corrosion. It is localised corrosion that will be studied in this thesis.

1.3.1.1 Corrosion Potentials

As all of the reactions involved in corrosion involve the movement of charge, either associated with electrons or with ions, the rate of corrosion can be determined by measuring the current. The rate of movement of electrons or ions into or out of the solution, i.e. the current, depends on the potential difference between the corroding metal and the solution.

The rates of the anodic and cathodic reactions depend on the potential of the metal (assuming the potential of the solution remains constant). When this potential becomes more positive the anodic reaction rate increases and the cathodic reaction rate decreases. When the potential of the metal becomes more negative the cathodic reaction rate increases and the anodic reaction rate decreases.

1.3.1.2 Reference Electrodes

The reference electrode is designed to provide a stable and reproducible potential and the type most commonly used is the standard calomel electrode (SCE). The potential difference between the SCE and the metal gives a standardised measurement of potential. Another type of reference electrode is the standard hydrogen electrode (SHE), this is rarely used in practice but potentials are often quoted in volts vs. SHE. The potential measured against the SCE or any other standard reference electrode used in an experiment can be easily converted so that it can be quoted as a potential against the SHE. The relationship between the two potential measurements is as follows (Equation 1.5).

Equation 1.5

$$\text{Potential vs SHE} = \text{Potential vs SCE} + 0.244V$$

The potential difference between the corroding metal and the solution is known as the Galvani potential (Φ) and this potential measured relative to a reference electrode is known as the electrode potential (E).

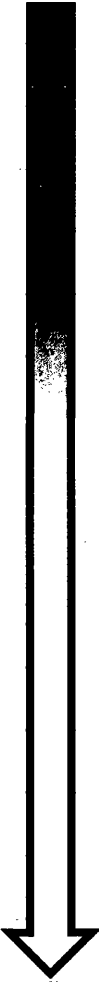
The relationship between the electrode potential, E , and the standard potential, E_0 is given by the Nernst equation

Equation 1.6:

$$E = E_0 - \frac{RT}{nF} \ln Q$$

where R is the gas constant ($8.31 \text{ J mol}^{-1}\text{K}^{-1}$), T is the temperature (K), n is the number electrons participating in the reaction, F is Faraday's constant and Q is the reaction quotient which is the quotient of the molar concentrations of the oxidant and reductant.

Table 1.4 Standard electrode potentials versus the SHE for a number of electrode reactions

Electrode Reaction		Standard electrode Potential (V vs SHE)
$\text{Au}^{3+} + 3\text{e}^{-} = \text{Au}$		1.42
$\text{O}_2 + 4\text{H}^{+} + 4\text{e}^{-} = 2\text{H}_2\text{O}$		1.229
$\text{Pt}^{2+} + 2\text{e}^{-} = \text{Pt}$		1.2
$\text{Ag}^{+} + \text{e}^{-} = \text{Ag}$		0.8
$\text{Fe}^{3+} + \text{e}^{-} = \text{Fe}^{2+}$		0.771
$\text{O}_2 + 2\text{H}_2\text{O} + 4\text{e}^{-} = 4\text{OH}^{-}$		0.401
$\text{Cu}^{2+} + 2\text{e}^{-} = \text{Cu}$		0.34
$2\text{H}^{+} + 2\text{e}^{-} = \text{H}_2$		0 (Reference)
$\text{Pb}^{2+} + 2\text{e}^{-} = \text{Pb}$		-0.126
$\text{Sn}^{2+} + 2\text{e}^{-} = \text{Sn}$		-0.136
$\text{Ni}^{2+} + 2\text{e}^{-} = \text{Ni}$		-0.25
$\text{Co}^{2+} + 2\text{e}^{-} = \text{Co}$		-0.277
$\text{Cd}^{2+} + 2\text{e}^{-} = \text{Cd}$		-0.403
$\text{Fe}^{2+} + 2\text{e}^{-} = \text{Fe}$		-0.44
$\text{Cr}^{3+} + 3\text{e}^{-} = \text{Cr}$		-0.744
$\text{Zn}^{2+} + 2\text{e}^{-} = \text{Zn}$		-0.763
$\text{Al}^{3+} + 3\text{e}^{-} = \text{Al}$		-1.662
$\text{Mg}^{2+} + 2\text{e}^{-} = \text{Mg}$		-2.363
$\text{Na}^{+} + \text{e}^{-} = \text{Na}$		-2.714
$\text{K}^{+} + \text{e}^{-} = \text{K}$	-2.924	

1.3.1.3 Kinetics of Corrosion

As discussed earlier, anodes and cathodes can be present at different locations on the same piece of corroding metal at the same time. Wagner and Traud's additivity principle [19] states that the total current flowing from the polyelectrode into any external circuit will be the algebraic sum of the individual currents due to individual couples. So, in the absence of net electrical current flowing into or out of the metal, that is under conditions of free corrosion;

Equation 1.7:

$$\sum i_{anodic} = - \sum i_{cathodic} = i_{corr}$$

Where i_{anodic} is the partial current due to anodic processes, $i_{cathodic}$ is the partial current due any cathodic processes and i_{corr} is the rate of corrosion expressed as a current. In this steady state condition the potential is known as the free corrosion potential E_{corr} .

Tafel [20] showed the relationship between current density, i , and potential, E , to be

Equation 1.8:

$$i_{anodic} = ke^E$$

and

Equation 1.9:

$$-i_{cathodic} = ke^E$$

Hence, if E is plotted against $\log i$ a straight line will result and this is known as a Tafel plot. If the Tafel plots for the anodic and cathodic processes are combined on one graph it is called an Evans diagram. The point of intersection of the two Tafel plots, where the anodic and cathodic current are equal, is defined as the free

corrosion current i_{corr} . The corresponding value of E , E_{corr} , can then be determined from the diagram.

If a range of potentials is applied to the metal surface and the current recorded, the potential can be plotted against the log of the current to give a 'polarisation curve'.

Figure 1.5 shows a typical polarisation curve obtained in this way.

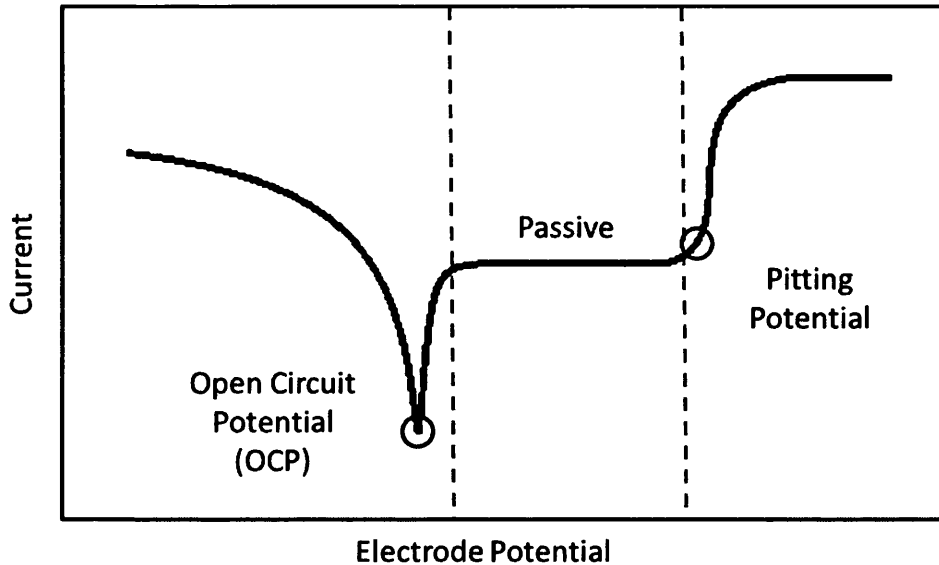


Figure 1.5 Polarisation curve

The approximately straight sections, the Tafel slopes, of both the anodic and the cathodic curves are extrapolated until they intersect. As above, the point of intersection gives the corrosion potential (E_{corr}) and the corrosion current (i_{corr}).

The rate of corrosion can now be calculated using Faraday's law:

Equation 1.10:

$$m = \left(\frac{Q}{F}\right) \left(\frac{M}{z}\right)$$

m = Mass of the substance liberated at the anode

Q = Total electric charge passed through the substance

$F = 96485 \text{ C mol}^{-1}$ (Faraday constant)

$z =$ valency number of ions of the substance (number of electrons transferred for each ion)

1.4 Corrosion of Aluminium and its Alloys

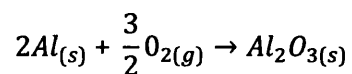
Aluminium has excellent resistance to corrosion when exposed to a wide range of environments and consequently has a wide range of applications from food containers to large ship superstructures. It is a very reactive metal; with magnesium and beryllium being the only structural metals that are more reactive.

1.4.1 Oxide layer

The high corrosion resistance of aluminium is possible due to its ability to become passive by the formation of an amorphous protective oxide film which is electrically insulating, strongly adherent and self-healing. This is because aluminium reacts readily and rapidly with oxygen in the environment.

When formed in air at room temperature the thickness of the oxide layer on aluminium is usually less than 5 nm. In its simplest form the oxide film formation can be described by the chemical reaction

Equation 1.11:



Under different conditions much thicker layers can be formed, for example at high temperatures, in steam or in water near its boiling point. If the temperature increases to around 500°C then the amorphous film of aluminium oxide will be broken by the growth of crystalline alumina.

Theoretically, when the surface of the aluminium is very smooth the film will be continuous. In most environments, damage to the oxide layer is instantly repaired maintaining corrosion resistance of the material. However under certain conditions repair cannot occur and corrosion of the exposed aluminium metal will follow. There is a dynamic relationship between forces acting to break down the oxide layer and those acting to regrow it. In contact with acids such hydrochloric and hydrofluoric acids and alkalis such as sodium hydroxide the oxide film dissolves.

Below (Figure 1.6) is a representation of conditions of pH and potential in which the absence or presence of the oxide layer is favoured. Diagrams of this type were invented by Marcel Pourbaix, the boundaries are calculated using the Nernst equation.

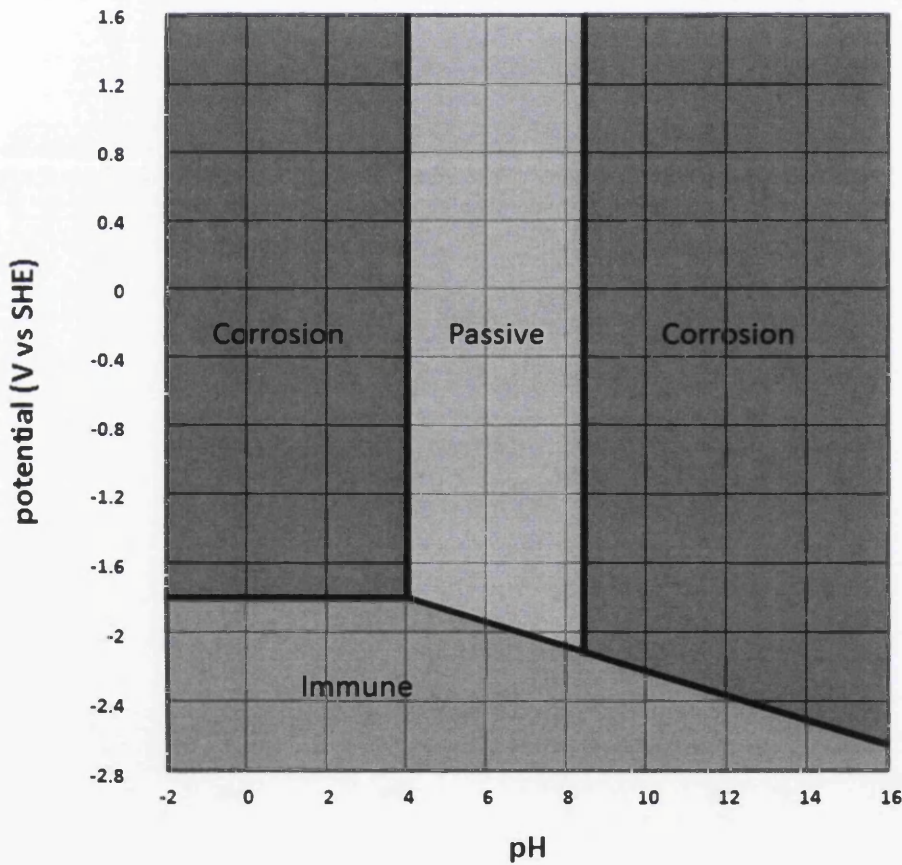


Figure 1.6 Pourbaix diagram

In the passive region there may be a tendency for corrosion to occur but the aluminium will be protected by the oxide layer. In the immune region there is no tendency for corrosive attack of the aluminium.

1.4.2 Intergranular Corrosion

Intergranular corrosion (IGC) can be defined as the preferential attack of the grain boundaries or regions close to the grain boundaries without significant attack within grains.

During the solidification of a metal, crystals nucleate and grow into the liquid until they meet and the metal is completely solidified. The crystals within the solid metal are known as grains. Between grains the crystal orientation changes and some atoms will not match either lattice. These regions between grains are known as grain boundaries. Grain boundaries are high-diffusivity paths because they have more open structure than the grain body. It has been shown experimentally that the 'jump' frequency of solute atoms along grain boundaries is greater than in the lattice [21]. The high interfacial energy at grain boundaries also makes them preferred sites for segregation of solute atoms and precipitation of second phase particles. Microgalvanic coupling with grain boundary segregates and precipitates makes some aluminium alloys particularly susceptible to intergranular corrosion.

The size, distribution and nature of the intergranular precipitates have a significant effect on the susceptibility. A semi-continuous distribution of fine intermetallics along the grain boundary will promote IGC. Precipitation hardenable alloys tend to be particularly susceptible and this susceptibility varies with their heat treatment condition. Alloys in which the precipitates are significantly more cathodic than the matrix will be subject to preferential corrosion of the adjacent matrix, whereas in alloys in which the grain boundary precipitates are more anodic, the precipitates themselves will corrode preferentially. Solute atoms also contribute to IGC susceptibility because their diffusion towards the grain boundaries to form precipitates results in a solute depleted zone developing adjacent to the grain

boundary. This depleted zone will have a potential which is different to that of both the precipitates at the grain boundary and of the matrix. The microgalvanic coupling which drives IGC may, therefore, lead to this solute depleted zone being preferentially dissolved [22, 23].

In aluminium copper alloys, the grain boundary precipitate, $CuAl_2$, will be cathodic relative to the matrix so that the solute depleted zone will preferentially dissolve. In aluminium magnesium alloys, the grain boundary precipitate, Mg_2Al_3 , will be more anodic and so will, itself, dissolve [5].

AA6000 series alloys are generally resistant to intergranular corrosion. If intergranular precipitation does not occur or if there is insignificant difference in the potentials of the matrix and the intergranular precipitates, the alloy will generally not be susceptible to intergranular corrosion. Alloys exposed to chloride containing environments are more vulnerable to IGC attack.

Copper content is critical for these AA6000 series alloys in terms of their IGC susceptibility. IGC susceptibility has been shown [16, 24-26] to be substantially limited when the copper content is around 0.1wt.% or less. However IGC has been identified in a copper-free model alloy by Shi [27].

1.4.3 Pitting Corrosion

Pitting corrosion affects metals which form protective oxide layers such as aluminium. The resistance of the metal is reduced locally when small defects in the oxide layer allow the electrolyte to make contact with the bulk metal. The attack is not particularly visible from the surface but pits often penetrate a long way into the metal and can therefore be structurally damaging.

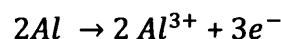
The formation of pits is generally regarded as a two stage process. The first stage is pit initiation which is the breakdown of the protective oxide layer without repair and the second stage, pit propagation, is the growth of the pit into the bulk metal.

The likelihood of initiation is partly dependent on the quality of the oxide layer. The ease with which the oxide layer is disrupted depends upon its porosity, thickness, solubility and strength. These characteristics are affected by the structure, composition and presence of defects in the metal on which the oxide forms. For example, the resistance of aluminium alloys to pitting increases with purity, so that the AA6000 series alloys are less resistant than AA1000 series alloys but more resistant than AA2000 series alloys. The halide (e.g. Cl^-) concentration of the electrolyte is also influential because the accumulation of negatively charged halide anions on the metal surface facilitates breakdown of the protective oxide layer. The oxide layer is unstable in highly acidic or alkaline solutions so that pitting will generally only occur in the pH range of approximately 4 to 9 as shown in the Pourbaix diagram for aluminium (Figure 1.6).

It is not always the case that defects in the oxide layer will lead to pitting; naturally formed oxide layers on aluminium often contain many defects which do not necessarily initiate pits.

Pit propagation is thought to be an autocatalytic process in which, following the initiation of the pit, aluminium is oxidised:

Equation 1.12:



The Al^{3+} cations will react with Cl^- anions to form $AlCl_4^-$ [28]; the hydrolysis of which results in higher acidity and Cl^- concentration in the pit [29]. The high acidity in the pit will result in a secondary cathodic reaction in the form of hydrogen evolution. Al^{3+} cations diffuse out of the pit and to the surface where the main cathodic process of hydrogen evolution or water reduction takes place on noble intermetallic particles. Aluminium hydroxide is formed and precipitates at the edges of the pit as a white corrosion product, partially blocking it and preventing the electrolyte from mixing with the aggressive pit solution. This maintains an 'occluded cell' in which the solution is able to remain much more acidic than the bulk electrolyte. However Cl^- ions can continue to diffuse through the hydroxide. Figure

1.7 shows a pit in aluminium and illustrates how the corrosion product maintains the occluded cell by partially blocking the pit.

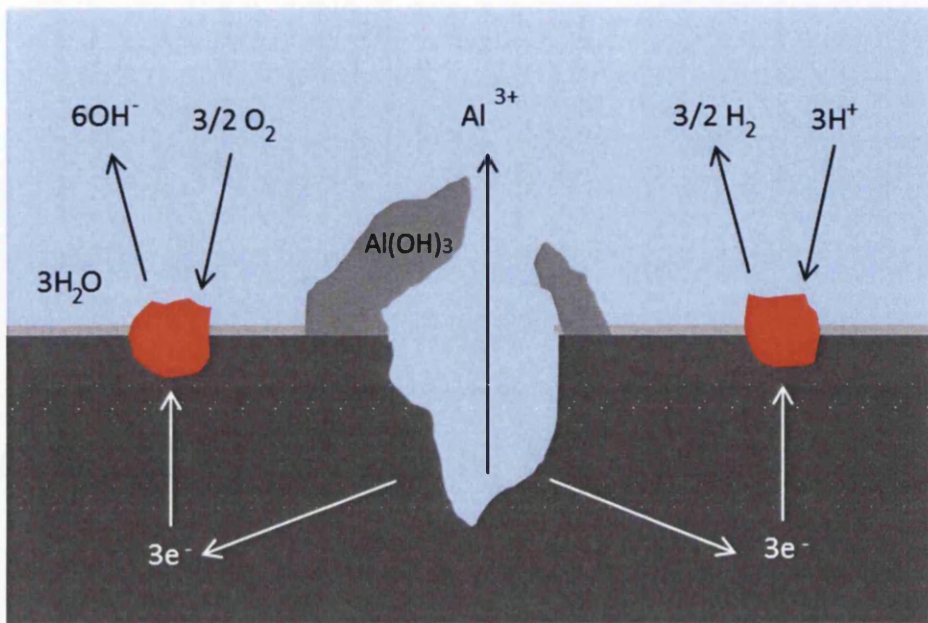


Figure 1.7 Pitting corrosion mechanism on aluminium

AA6111 is a heat-treatable alloy and so it has a heterogeneous microstructure which is developed by careful control over composition and ageing hardening heat treatment. The exact precipitation sequence for AA6111 will be discussed in detail in section 1.5 but in essence precipitates of a copper rich phase will be cathodic relative to the matrix and precipitates of a magnesium rich phase will act as anodes. Both anodic and cathodic precipitates will couple microgalvanically with the aluminium which can make the alloy susceptible to localised attack in the form of pitting.

For each combination of material and environment there is a specific potential at which the protective oxide layer breaks down and leads to stable pitting; this is called the 'pitting potential'. Slightly below the pitting potential metastable pits may form which quickly repassivate. The pitting potential can be identified by performing a polarisation experiment (see Kinetics of Corrosion 1.3.1.3); at the

pitting potential there is a sharp increase in current relative to potential. A typical polarisation curve showing this behaviour is shown in Figure 1.5.

1.4.4 Filiform Corrosion

The third type of corrosion relevant to this study is filiform corrosion (FFC). FFC is distinct from most other forms of corrosion in that it does not generally lead to deterioration in mechanical properties of the material; it is usually completely cosmetic. The first investigation into FFC was carried out in 1944 by Sharman [30]. He described the phenomenon as a 'deterioration process that gives rise to corrosion products of filamentous appearance under coating'. The problem of FFC is not confined to aluminium alloys; steel and magnesium are also affected. It was in steel that FFC was first identified and where all of the initial research was focused. Interest in FFC on aluminium developed later and this has become an active area of research.

A number of factors contribute to the development of FFC [2, 31-40]:

Material

Some metallic substrates are more prone to FFC than others, for example magnesium is particularly susceptible. The level of adhesion between the substrate and the coating is also important. The nature of the coating itself does not seem to be influential; FFC been found under a wide range of coatings.

Coating defect

FFC filaments usually initiate at breaks in the coating which expose the bare metal to the environment.

Humid environment

It is generally believed that FFC requires a relative humidity in the range 60-95%, optimally 80-85%.

Aggressive anion

Condensates containing ions such as chloride, bromide, sulphate, carbonate and nitrate have been found to facilitate FFC on aluminium alloys.

Oxygen

An oxygen containing environment is necessary; FFC has been shown not to occur in inert atmospheres.

Temperature

Ambient temperature is sufficient for FFC to occur but it has been shown that increasing the temperature can increase the corrosion rate.

FFC is usually initiated at a flaw in the coating. If the environment is relatively humid, water will penetrate the coating by osmosis, bringing with it any soluble salt it has dissolved [32, 41]. This dissolved salt and any salt that was deposited on the substrate surface before coating will collect as a liquid. Once this has happened, any additional water penetrating the coating is retained. The substrate will then begin to corrode releasing ions into the solution. The corrosion products will cause some of these initiation points to become occluded cells and the filament will start to grow due to differential aeration. The cathode will be located at the back of the cell where there is a good supply of oxygen and the oxygen depleted anode will be at the front.

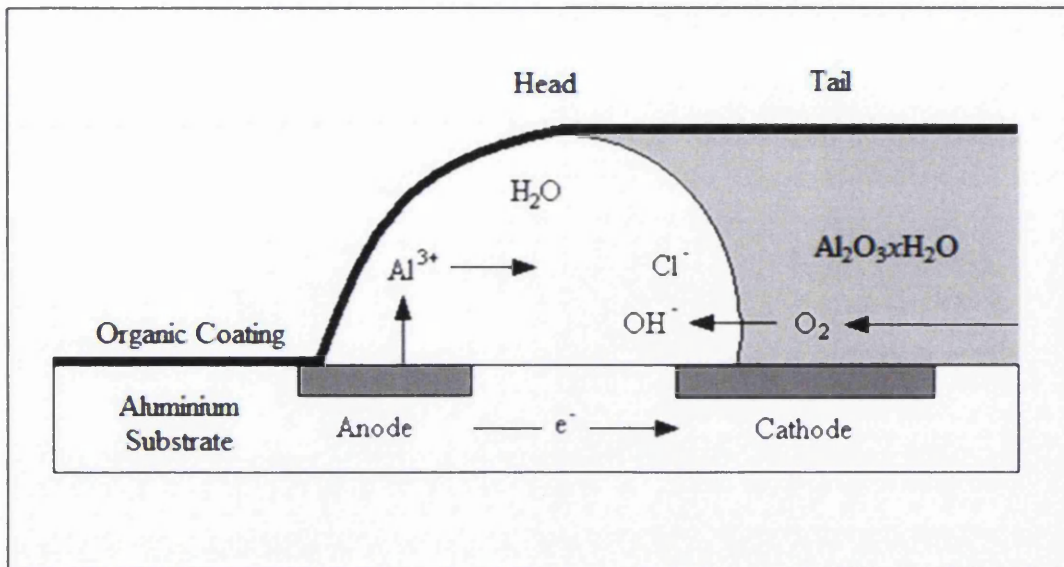
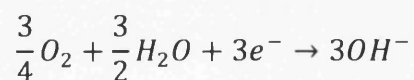


Figure 1.8 Structure and electrochemistry of an FFC filament

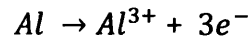
Various models have been proposed for the mechanism by which FFC propagates but it is now accepted that the one suggested by Kaesche [35] and refined by Ruggeri and Beck [33] is consistent with experimental results and observations. This mechanism is represented schematically in Figure 1.8 which shows the filament head beneath the organic coating on aluminium. The method by which oxygen is transported to the active filament head was initially widely disputed with some authors believing that diffusion through the coating itself was the main pathway, Kaesche [35] was the first to suggest that the transport of oxygen occurred through the dry and porous corrosion product in the tail. This proposal is supported by the asymmetric shape of the FFC head. The differential aeration cell at the head is maintained by the continuous supply of oxygen. The head, which is filled with the liquid electrolyte, is active whereas the tail is passive. The cathodic reaction mainly takes place at the back of the filament head as oxygen reduction:

Equation 1.13



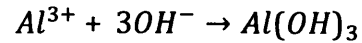
The anodic dissolution mainly takes place at the front of the head:

Equation 1.14



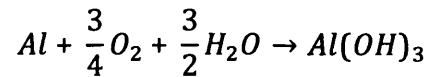
The aluminium ions are hydrated causing local acidification:

Equation 1.15



Equation 1.16

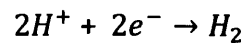
Overall:



The chloride anions are conserved at the front of the head so that aluminium dissolution continues.

As a result of bubbles being observed at the front of the head [39, 42, 43], it has been proposed that a further cathodic reaction, hydrogen evolution, takes place:

Equation 1.17



1.5 Heat Treatment, Precipitation and their Effect on Corrosion

As discussed previously, pure aluminium metal has high corrosion resistance due to the protective oxide film on its surface [44]. However, many of the alloying elements in common use have limited solid solubility and commercial alloys will usually contain second phase particles. Occasionally individual elements will precipitate to form particles but usually two or more elements will precipitate together to form intermetallic compounds. The composition, size, quantity, location and distribution of these particles all affect the corrosion behaviour. The difference in the electrochemical properties of intermetallic particles compared to the aluminium matrix is thought to be the underlying cause of many types of localised corrosion of aluminium [44].

Corrosion results from the movement of electrons from anodes to cathodes. Therefore relationships between the corrosion potentials (E_{corr}) of the alloy's constituents are important in determining the type and amount of corrosion that is likely to occur. The composition of the alloy and the heat treatments which have been applied to it will determine the phases present. The value of E_{corr} for the matrix plays the largest role in determining the overall value of E_{corr} for the alloy. Alloying elements such as copper will have a significant effect on the E_{corr} of the alloy up to their solid solubility limits. For example, an addition of 4wt% copper to pure aluminium can increase its E_{corr} by around 0.12V. Further increases in copper content do not cause significant further change in E_{corr} because it cannot dissolve and instead forms second phase particles [2]. Silicon and manganese can also increase the corrosion potential when in solid solution whereas magnesium can decrease it.

Second-phase particles play an important role on a microscopic scale. There can be a significant difference in E_{corr} between these particles and the matrix from which they precipitate and this can set up local galvanic cells between them [2]. Second phase particles on the surface of the metal will form anodes if their E_{corr} is lower than that of the matrix and cathodes if their E_{corr} is higher. For example copper,

iron and silicon, which are present as impurity elements in aluminium alloys form cathodic intermetallics: $CuAl_2$ [6], $FeAl_3$ and $AlMnSi$ [5]. Mg_2Al_3 is anodic to the matrix and can form continuous grain boundary films which can lead to corrosion which penetrates deeply into the aluminium substrate [6]. Second phase particles on the surface will also affect the protective oxide layer by causing either weaknesses or discontinuities in it. For this reason they often act as sites for the initiation of corrosion such as pitting [5, 44]. Copper content increases corrosion susceptibility of aluminium to a greater extent than any other alloying element [5].

Afseth et al [45] studied a number of binary aluminium model alloys containing Mg, Mn, Fe and Cu which were produced in the laboratory using a method that simulated standard commercial DC casting methods for sheet production. Alloying elements were added in quantities below their solid solubility limits. The alloys were tested in the as-rolled condition and after annealing for 2 hours at 450°C. Thermo-Electric Power (TEP) measurements were used to calculate the solid solution compositions of the samples. It was shown that all of the samples consisted of solid solutions in the as rolled condition. The solute compositions of the Al-0.04wt.%Fe and Al-1%Mn dropped as a result of the annealing heat treatment suggesting the precipitation of the intermetallic particles $FeAl_3$ and $MnAl_6$ respectively. The alloying elements were retained in solid solution in the other binary alloys.

A standard accelerated laboratory test was used to assess FFC susceptibility. The $FeAl_3$ intermetallics were cathodic relative to the matrix and their presence in the annealed sample gave rise to FFC susceptibility which was not seen in the as-rolled Al-0.04wt.%Fe. The Al-Mn alloys were also resistant to FFC in the conditions tested and this can be attributed to the $MnAl_6$ intermetallics having similar electrochemical properties to the aluminium solid solution matrix and therefore not creating micro-galvanic couples. The Al-Mg alloys did not exhibit any FFC in either the as-rolled or annealed condition, this might be expected because no precipitation was identified in these alloys; the alloying elements were retained in solid solution. The Al-Cu alloys did not develop precipitates either but FFC testing showed the Al-1%Cu sample to be very susceptible in both the as-rolled and

annealed conditions. SEM in combination with EDX exposed the probable cause of this susceptibility; selective dissolution of aluminium resulting in enrichment of copper in the form of copper rich or possibly pure copper particles on the surface. These particles were identified only in the corroded regions and were probably the sites for the cathodic corrosion reactions.

The authors explained this set of results with a general statement that 'microgalvanic coupling between the aluminium rich matrix and more noble second phase cathodic sites are necessary for localised corrosion, to occur on aluminium alloys'. Filiform corrosion testing carried out on as-rolled copper containing alloys based on the composition of AA3005 for another paper by the same authors [46] supported the conclusion that noble intermetallics were required to act as efficient sites for cathodic reactions for localised corrosion to occur. The presence of copper in these alloys significantly increased susceptibility to FFC and again local enrichment and re-distribution of copper caused by the selective dissolution of the aluminium rich matrix was thought to be an influential process producing copper rich sites for cathodic corrosion reactions on the surface. FFC testing was performed on the alloys in this study in both the as-rolled and caustic etched condition, the FFC resistance of the AA3005-like alloys without copper did not appear to significantly improve but the FFC resistance of the copper containing AA3005-like alloys did improve. As the caustic etching process is known to enrich copper near the surface of aluminium alloys at the metal-oxide interface this result does not appear to agree with the previous conclusion that copper enrichment leads to FFC susceptibility by providing cathodic sites. The authors propose a mechanism which relies on differentiating the process by which copper is enriched as a result of caustic etching from the process by which copper is enriched as a result of corrosion. It is explained that a thin layer of copper-enriched solid solution at the metal surface produced by caustic etching could reduce the micro-galvanic coupling effect of the copper rich particles formed by selective dissolution during corrosion. An increase in FFC resistance as a result of caustic etching of previously cold-rolled aluminium alloys is often attributed to the dissolution of the electrochemically active deformed layer.

The authors suggest that the FFC susceptibility of the AA3005-like alloys tested here is more strongly controlled by their bulk microstructural properties.

Afseth et al [45] draw another conclusion from the fact that the as received sample of the Al-0.5%Mg alloy was not found to be susceptible to FFC despite the observed (using TEM) presence of a deformed surface layer. It is stated that the presence of a deformed surface layer by itself does not give rise to FFC.

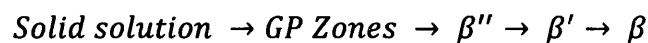
The extent and nature of corrosion on an aluminium alloy depend to a large extent on its microstructure which is determined by its composition and the mechanical and thermal processes used in its production.

Aluminium alloys of the AA6000 series are heat-treatable. When used in the T4 temper the sheet has good formability and so stamping procedures can be carried out successfully. Once the paint has been applied, the thermal paint curing procedure leads to a significant hardening response which provides a good dent resistance in the final product. The size, type and distribution of precipitates formed as a result of the thermomechanical history of these alloys will not only influence the formability and hardness of the material, they will also have a significant effect on corrosion susceptibility and so this also requires significant consideration.

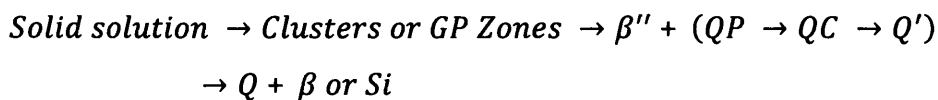
The local chemistry and therefore the corrosion susceptibility of the aluminium alloy is sensitive to the temperature and time profile of artificial ageing heat treatments. The aim of the solution heat treatment is to dissolve all of the alloying elements and rapid quenching is then required to preserve this structure as a solid solution at room temperature. It is not always possible to achieve sufficiently rapid quenching, especially when thick sections lead to uneven cooling rates. Sometimes products are deliberately quenched more slowly to prevent residual stress and distortion. Any local differences in precipitation as a result of cooling rate variations will lower corrosion resistance [2]. Overageing, which is ageing beyond the peak hardness (T6) condition, is sometimes employed to obviate the damaging effects of these localised differences in precipitation. It leads to the precipitation of incoherent precipitates whose distribution is not related to local cooling rate differences [47].

The precipitation sequence of the copper free Al-Mg-Si alloys is relatively well studied [48-50] and is shown in Equation 1.18. Magnesium silicide (Mg_2Si) is thought to be the dominant equilibrium phase [51] and this phase is usually denoted as β . There are a number of metastable phases which form as precursors to β and are denoted β'' and β' . The phase responsible for peak hardness is β'' [52]. The metastable phases form as very fine precipitates and are thought to develop from GP zones, their crystal structure and composition is debated.

Equation 1.18:



It had been assumed that the precipitation sequence in AA6000 series alloys with a significant copper content (Al-Mg-Si-Cu) such as AA6111 was similar to that in AA6000 series alloy without a significant copper content. It is now known that a quaternary AlMgSiCu phase is formed during ageing in some Al-Mg-Si-Cu alloys, this was first experimentally observed by Dix et al in 1932 [53]. This phase is the equilibrium precipitate for most of the Al-Mg-Si-Cu family of AA6000 series alloys [51] and has now been designated as Q and has been shown to coexist with β'' in these alloys [54]. Arnberg et al [55] suggested that the Q phase has a hexagonal crystal structure and has the composition $Cu_2Mg_8Si_7Al_4$. Copper content and the Mg:Si ratio will affect the precipitation sequence so that different transition phases will form in different AA6000 series alloys. Chakrabarti and Laughlin [51] identified the following precipitation sequence for a balanced alloy system:



Miao et al [56] suggested the following sequence for AA6022 (containing excess Si)
- with low copper content:



- with 0.9wt.% copper:



Perovic et al [54] aged samples of AA6111 at 180°C for 0.5, 1.5, 11 and 240 hours. In the first three of these β'' and Q phases were found to be present but in the overaged condition (240 hours at 180°C) only the Q phase was identified. A phase which appeared crystallographically identical to the Q phase was identified in AA6016 in the overaged condition but its composition was outside the range normally reported for the Q phase, containing little or no copper. In AA6111 the Mg:Si ratio in the Q phase was found to be approximately 1 whereas the phase which was reported to be similar to Q phase had an Mg:Si ratio of 1.35.

The clusters and zones formed early in the stages of the ageing sequence of Al-Mg-Si-(Cu) alloys are very difficult to study using electron microscopy because they are ultrafine. Miao and Laughlin [57] used differential scanning calorimetry (DSC) in combination with hardness measurements to examine the precipitation occurring in AA6111. All samples were initially solutionised at 560°C for 20 minutes and quenched but samples were examined in three different ageing conditions; as quenched, quenched and naturally aged for 30 days or quenched, pre-aged (at 75°C for 8 hours) and then naturally aged for 30 days. DSC was performed with a heating rate of 20°C min⁻¹, hardness measurements were made on samples which were heated at this rate and then held at a temperature in the range 50-350°C for one minute. The DSC trace for the as quenched sample showed an initial exothermic peak relating to the formation of GP zones at 100°C and a simultaneous increase in hardness. There was a sharp exothermic peak at 250°C which coincided with peak hardness and was attributed to the precipitation of β'' . The final exothermic peak occurred at 300°C and was thought to be as a result of β' and/or Q' phase formation. Precipitation of these phases was said to be mainly responsible for the decrease in hardness that was demonstrated at higher temperatures.

Interestingly the DSC trace for the sample which was in the naturally aged condition lacked the small exothermic peak at 100°C suggesting that GP zone formation had already taken place (during natural ageing). The hardness of the naturally aged sample started above the value shown after the GP zones peak for the as-quenched sample supporting the theory that GP zones had already formed and contributed to the hardness of the alloy. This finding by Miao and Laughlin [57] is significant

because where AA6000 series alloys are used for automotive body panels a large bake hardening response is beneficial. This is because formability (low hardness) is the initial requirement when shaping the sheet into panels, the panels are then painted the age hardening occurs during the paint baking process. The paint bake response (the increase in hardness as a result of curing the paint at around 180°C for 20-30 minutes) needs to be large so that the final product has good dent resistance (high hardness). This work shows that the lower paint bake response of naturally aged as compared to as-quenched material is a result of the formation of GP zones with a range of types and/or sizes.

A broad endothermic bump appeared on the DSC trace of the naturally aged sample and this coincided with a decrease in hardness. It was noted that this was probably as a result of the dissolution of at least some of the GP zones which had previously formed, it's broadness indicated that the dissolving GP zones and clusters were quite varied in terms of their type and/or size. As for the as-quenched sample a β'' peak occurred at peak hardness and then β' and/or Q' resulted in a decrease in hardness on overageing.

An endothermic bump was apparent on the DSC trace of the sample which had been pre-aged but it was smaller and at a higher temperature than the bump on the naturally aged sample. It was said that this indicated that the phases formed as a result of the pre-ageing then natural ageing were more stable than those formed by natural ageing alone and that these could act as sites for the precipitation of the main hardening phase β'' . The decrease in hardness was also smaller for the pre-aged sample. A hardness curve for the naturally aged and the pre-aged then naturally aged samples was plotted for ageing at 175°C (a normal automotive paint baking temperature), it showed that although both samples reached a similar peak hardness, pre-ageing had increased the initial hardening rate and so for a typical paint baking heat treatment of 20-30 minutes it would lead to the attainment of a higher post paint-bake hardness [57].

The intergranular corrosion susceptibility of AA6000 series alloys is sensitive to the ratio of magnesium to silicon it contains. Theoretically, when the atomic ratio is 2:1

the Mg_2Si constituent is formed and there is not any excess magnesium or silicon remaining. In this case the intergranular corrosion susceptibility is relatively low. When the magnesium to silicon ratio is less than 2:1, there is excess silicon, which is insoluble and highly cathodic and leads to much higher susceptibility [2]. It is thought that the metastable precursors to β may have a Mg to Si ratio which is about half of that of the stable phase [52]. Automotive alloys usually contain excess silicon because this increases the paint-bake hardening response [58]. In copper containing AA6000 series alloys with an excess of Si relative to the Q phase composition ($Al_5Cu_2Mg_8Si_6$), precipitation of phases such as Si may cause increased IGC [24]. However if the Si precipitates are in contact with water they will not necessarily be effective cathodes due to the presence of an insulating layer of SiO_2 [59]. Depletion of (cathodic) silicon in the matrix either side of the grain boundary makes it active and liable to corrosion by microgalvanic action. Where Q phase precipitation occurs at grain boundaries the effect is exacerbated because they are also cathodic relative to the depleted zone [24]. Eckermann et al [60] found that in AA6111 exposed to a 1M NaCl solution, $MgSi$ particles were selectively de-alloyed of Mg for a period of approximately 20 minutes and that this process controlled the open circuit potential of the surface during that time. The Si-rich $MgSi$ remnant was found to be cathodically active.

Alloy composition, in particular the amounts of copper, magnesium and silicon, cooling rate after solutionisation and the duration and temperature of ageing heat treatments are all factors that affect the precipitation in heat treatable AA6000 series aluminium alloys. It is difficult to discuss these factors independently because they all interact with each other to determine the nature of the precipitation that occurs. The type, size, spacing and location of the precipitates will all subsequently influence the corrosion behaviour of the alloy. Limited work has been done on AA6111 itself but work on other AA6000 series alloys and on similar model alloys also contribute useful insight. Below is a review of some of the most relevant work.

A particularly useful series of papers [16, 24-26, 61] will be examined in detail below. Table 1.5 lists the composition of each of the alloys studied in these papers.

Table 1.5 Composition of AA6000-series-like alloys studied in [16, 24-26, 61]

Alloy		Mg	Si	Fe	Mn	Cu	Cr	Ti	Zn	Al	
Atomic wt.		24.305	28.086	55.845	54.938	63.546	51.996	47.867	65.380	26.982	
High Cu	[16]	wt.%	0.5200	0.6000	0.2100	0.2100	0.1200	0.0200	0.0100	0.0040	98.3060
		at.%	0.5788	0.5780	0.1017	0.1034	0.0511	0.0104	0.0057	0.0017	98.5693
Low Cu	[16]	wt.%	0.5700	0.9300	0.2000	0.5900	0.0005	0.0300	0.0100	0.0060	97.6635
		at.%	0.6353	0.8970	0.0970	0.2909	0.0002	0.0156	0.0057	0.0025	98.0557
Model Alloy	[25]	wt.%	0.5700	0.6200	0.2100	0.2100	0.1300	0.0010	0.0100	0.0070	98.2420
		at.%	0.6344	0.5972	0.1017	0.1034	0.0553	0.0005	0.0057	0.0029	98.4988
Model Alloy	[24]	wt.%	0.5700	0.6200	0.2100	0.2100	0.1300	0.0010	0.0100	0.0100	98.2390
		at.%	0.6344	0.5972	0.1017	0.1034	0.0553	0.0005	0.0057	0.0041	98.4976
A	[26]	wt.%	0.5500	0.6000	0.2000	0.1500	0.1700	0.0200	0.0100	0.0200	98.2800
		at.%	0.6122	0.5780	0.0969	0.0739	0.0724	0.0104	0.0057	0.0083	98.5424
B	[26]	wt.%	0.5400	0.6000	0.2200	0.1500	0.0200	0.0300	0.0100	0.0100	98.4200
		at.%	0.6006	0.5775	0.1065	0.0738	0.0085	0.0156	0.0056	0.0041	98.6077
A	[61]	wt.%	0.5000	0.5900	0.2200	0.1500	0.0200	0.0300	0.0000	0.0000	98.4900
		at.%	0.5561	0.5679	0.1065	0.0738	0.0085	0.0156	0.0000	0.0000	98.6717
B	[61]	wt.%	0.5200	0.6000	0.2100	0.1400	0.1800	0.0200	0.0000	0.0000	98.3300
		at.%	0.5788	0.5779	0.1017	0.0689	0.0766	0.0104	0.0000	0.0000	98.5856
C	[61]	wt.%	0.6100	0.8000	0.2600	0.2100	0.7000	0.0200	0.0000	0.0000	97.4000
		at.%	0.6814	0.7733	0.1264	0.1038	0.2991	0.0104	0.0000	0.0000	98.0056

Effect of low Cu content and heat treatment on IGC of model AlMgSi Alloys [16]

Svenningsen et al [16] studied the effect of copper content and heat treatment on the IGC of two model AlMgSi alloys. One of the alloys contained only 0.0005wt.% copper and the other contained 0.12wt.% copper, these alloys were referred to as ‘low Cu’ and ‘high Cu’ respectively, their composition is shown in Table 1.5. The alloys also contained magnesium and silicon in different ratios, in the low Cu alloy the atomic Mg:Si ratio was 0.71, this ratio was 1.00 in the high Cu alloy. Comparing the atomic Mg:Si ratio of these alloys to the stoichiometric composition of magnesium silicide it can be seen that both contain excess silicon. The low Cu alloy contains 2.82 times more silicon than that required for the stoichiometric formation of magnesium silicide and the high Cu alloy contains 2.00 times the required amount. As explained previously, the metastable precursors to the Mg₂Si (β) phase contain a larger proportion of silicon than the stable phase [52] and so these alloys are suited to the precipitation of the precursor phases without much surplus magnesium or silicon. Samples were either air cooled or water quenched after

extrusion from a die-exit temperature of around 560°C. This is the approximate solutionising temperature used with AA6000 series alloys so it would be expected that all phases would be dissolved during extrusion.

Field emission scanning electron microscopy (FE-SEM) was used in combination with energy-dispersive x-ray spectroscopy (EDX) to characterise the grain-boundary microstructure. FE-SEM of air-cooled samples of the low and high copper alloys revealed large grain boundary and in-grain precipitates after electropolishing. EDX analysis of the grain boundary precipitates resulted in the identification of AlMgSiCu and MgSi phases. AlMgSiCu particles were found in only the high Cu alloy whereas MgSi particles were found in both. A comparison of the Mg:Si and Cu:Si ratios with those for Mg₂Si (β phase) and Al₄Mg₈Si₇Cu₂ (Q phase) suggested that these may have been the two phases present although it was noted that the electropolishing technique can lead to the chemical modification of the surface. FE-SEM of water quenched and naturally aged samples did not reveal any grain boundary precipitates however subsequent artificial ageing to the T6 condition (5 hours @ 185°C) appeared to lead to the formation of small precipitates. The same artificial ageing treatment on the air cooled samples did not affect their grain boundary precipitates in terms of size, composition or density.

All of the sample variants except the water quenched low Cu T6 sample showed some degree of susceptibility to intergranular corrosion and pitting during field testing. The high Cu alloy was shown to be more susceptible than the low Cu alloy. Study of the corrosion propagation with respect to time indicated that corrosion of the high Cu alloy continued throughout the 24 month test period, in contrast, the propagation of corrosion of the low Cu alloy slowed down and sometimes stopped. The accelerated test data in this study was obtained following BS 11846 method B [62] on samples cut from the extruded profiles. This involves the degreased, alkaline and desmuted samples being immersed in an acidified sodium chloride solution. These results reinforced the finding that the high Cu alloy was more susceptible, in fact in this test the low Cu alloy was found to be essentially resistant to localised corrosion.

The IGC susceptibility of the high Cu alloy was found to be particularly sensitive to its thermal history. Air cooled high Cu samples were the most susceptible but they became less susceptible as a result of artificial ageing. In contrast the IGC susceptibility of water quenched samples was increased.

The preferential precipitation of the cathodic copper containing Q phase at grain boundaries and microgalvanic coupling with the adjacent copper depleted zone is often the proposed mechanism for IGC in AA6000 series alloys. This preferential precipitation occurred in the high Cu air cooled samples because there was sufficient time for diffusion to occur, in the water quenched specimens there was less time for the diffusion of solute atoms to occur and so no Q phase particles could be seen at grain boundaries. Ageing of water quenched samples to the T6 condition provided sufficient energy for some diffusion to occur towards the energetically favourable grain boundaries. The reduction in IGC susceptibility of air cooled specimens as a result of ageing was not explained by this study.

Effect of high temperature heat treatment on IGC of AlMgSi(Cu) model alloy [25]

A slow post-solutionising cooling rate was identified as a factor which increased the intergranular corrosion susceptibility of the higher copper (0.12wt.% Cu) alloy in [16]. In this study [25] Svenningsen et al investigate this phenomenon further using an alloy with a similar composition to the 'high Cu' alloy in [16], the compositions of both alloys are shown in Table 1.5. This time slow cooling rates are simulated by holding the samples at temperatures between 250°C and 450°C for between 10 seconds and 10^4 seconds immediately after solutionising for 30 minutes at 540°C. Corrosion testing was, again, carried out following BS 11846 method B [62].

For all samples that were held at 450°C the corrosion mode was etching. The sample held at 400°C for 10 seconds also etched but intergranular corrosion and pitting occurred on samples held for longer times at this temperature. Samples held at 350°C, 300°C and 250°C all exhibited intergranular corrosion for short hold times and pitting for long hold times. For the samples held at 300°C and 250°C it was shown that the severity of IGC attack initially decreased with increasing holding

time. Intermediate holding times resulted in samples which were highly resistance to localised corrosion, neither IGC or pitting was observed on these samples.

A possible explanation for this effect was put forward; a narrow noble film developed at grain boundaries in the samples which were held for short times and the continuity of this film resulted in the sharp and narrow intergranular corrosion which was observed in these samples after corrosion testing. It is suggested that this film may have been made discontinuous as a result of grain boundary precipitates coarsening in samples held for longer times and that these discrete particles were less detrimental in terms of IGC susceptibility. Another hypotheses was put forward; the cathodic Q phase particles which are thought to be responsible for the alloy's corrosion susceptibility can be passivated by a layer of SiO₂. Neither of these theories could be proven using FE-TEM in this study.

It is also possible that coarsening of precipitates within the matrix reduces the corrosion potential gradient between itself and any grain boundary solute depleted zones thus reducing the driving force for corrosion by microgalvanic coupling.

Effect of artificial ageing on IGC of extruded AlMgSi alloy with small Cu content

[24]

A third study by Svenningsen et al [24] on the same alloy as [25] investigates the effect of artificial ageing on the IGC susceptibility of the alloy. The composition of the alloy is shown in Table 1.5. The ageing heat treatments are applied to an extruded plate of the alloy in the T4 condition. The die exit temperature was recorded as being 575°C-580°C and the extrusions were subsequently cooled in ambient air. Again the die exit temperature is similar to or above the normal solutionising temperature for these materials and so a solid solution would be expected to have formed before the samples were cooled. Ageing heat treatments were applied after 3 months of natural ageing. Three different ageing temperatures were used and for each ageing temperature a number of samples were prepared with different ageing times. One set of samples was aged at 140°C for between 5000 and 1720000 seconds, another at 185°C for between 500 and 86400 seconds and a final set at 220°C for between 100 and 86400 seconds. As in the previous

papers the corrosion testing was carried out in accordance with British Standard BS-ISO 11846 [62]. FE-TEM with EDX was used to characterise the grain boundary microstructure and to find evidence for the mechanisms controlling the changes in IGC and pitting susceptibility of the alloy as a result of various artificial ageing procedures.

As in [25] microscopy results showed that IGC susceptibility was initially high in this air-cooled material and that this susceptibility decreased with ageing time at each of the three temperatures. These results contrast with a number of studies cited by Svenningsen et al [63-70] which found the IGC susceptibility of air cooled samples to increase as a result of artificial ageing to the T6 condition. An intermediate ageing time for each temperature resulted in a material which was resistant to localised corrosion under the corrosion test conditions. At longer times pitting was introduced. Hardness measurements were used to indicate the degree of age hardening that had occurred after each heat treatment. For each of the three ageing temperatures the highest corrosion resistance approximately coincided with the maximum hardness. This is a very interesting finding which could be exploited by manufacturers for whom the combination of high strength and corrosion resistance is highly sought after.

FE-TEM revealed large and discrete Mg_2Si and Q phase particles at grain boundaries as described in [16] and [25]. One of the main additional findings of this work was that a thin (nanometer scale) copper rich film existed away from the copper rich Q phase particles. Away from the Mg_2Si and Q phase Cu was the only other element found to have been enriched at the grain boundaries, this was revealed by EDX analysis. The copper rich film was less evident on the overaged samples compared to samples in the T4 and T6 conditions and this is thought to be the reason for the increased IGC resistance of these samples.

The knife-edge intergranular attack which was seen on air cooled samples was attributed not only to the presence of the noble Q phase particles as it is thought that these discrete particles would not result in such a sharp and continuous attack morphology. The thin Cu rich film discovered in this work is thought to provide the

continuous noble pathway necessary for this to occur. It is explained that the copper rich film may be a precursor to the *Q* phase.

The proposed mechanism of the attack is propagation along the regions rendered anodic adjacent to the copper rich film. It is also explained that it is possible that copper from the *Q* phase and the film dissolve in the chloride containing and acidic electrolyte and redeposit on the exposed grain walls. The discontinuity in the copper rich film resulting from its coarsening in underaged and peak aged samples is thought to arrest the propagation of IGC making them more resistant. Overageing leads to increased precipitation of *Q* phase particles within grains which leads to solute depletion within in the matrix and reduces the potential gradient between it and the solute depleted zones adjacent to the grain boundaries. Thus the driving force for IGC is reduced and pitting becomes the dominant mechanism. Similar results were found by other authors [66, 71, 72].

Effect of Thermomechanical History on Intergranular Corrosion of Extruded AlMgSi(Cu) Model Alloy [26]

This study by Svenningsen et al [26] used one low copper alloy and one higher copper alloy as in [16], the difference is that here the alloys have similar quantities of the other alloying elements whereas in [16] the silicon and manganese quantities were different. The composition of these alloys is shown in Table 1.5. The aim was to isolate copper content as a factor, so that its effect on the IGC susceptibility of these alloys could be tested more stringently. A further aim was to find investigate the effect of ageing on water quenched samples in more detail than previously.

One set of control samples was prepared using a similar method to [16], they were water quenched or air cooled from after leaving the die at over 500°C, stretched and then naturally aged to T4 or artificially aged to T6 (5h @ 185°C). The main set of samples was cut from air cooled extrusions of alloy A and then solution heat treated (30 minutes @ 540°C). They were water quenched or air cooled and then transferred to an oil bath for artificial ageing at 185°C. As in the previous studies by this author the corrosion testing was carried out in accordance with British Standard BS-ISO 11846 [62]. Hardness measurements were made on artificially aged samples.

Microstructure was investigated using optical microscopy on metallographic cross sections. The grain boundary microstructure was observed using FE-TEM.

Results of the corrosion testing of the control samples showed that in general the low copper alloy B was resistant to IGC and the higher copper alloy A was susceptible. The susceptibility of alloy A was dependent on the post extrusion cooling method. Air cooling resulted in a severe IGC attack on this alloy after corrosion testing, the water quenched sample suffered only slight corrosion. Artificial ageing of the air cooled variant to the peak aged (T6) condition significantly reduced IGC susceptibility and made the attack more localised. Further ageing eliminated localised corrosion and overageing introduced pitting susceptibility. When the water quenched sample was aged to the T6 temper the susceptibility to IGC increased; ageing had the opposite effect. These results for the control samples support previous results by Svenningsen et al [16] in terms of the effect of copper content, quenching and ageing on IGC susceptibility.

The main set of samples which were solution heat treated before either air cooling or water quenching and artificial ageing behaved slightly differently. As before the air cooled sample was susceptible to IGC in the T4 condition and this susceptibility was reduced and eventually eliminated by artificial ageing. One difference to the equivalent control sample (which was not solution heat treated before ageing) was that overageing did not introduce pitting, instead localised IGC was reintroduced. IGC on these overaged samples was much coarser than the knife-edge attack seen on samples aged for shorter times. This change in the morphology of IGC was also seen in the water quenched samples when they were overaged but the relationship between the susceptibility and the degree of ageing was different. These samples, which were solution heat treated and water quenched before ageing, showed only uniform etching in the T4 condition but heat treatment of only 1000 seconds at 185°C led to extensive uniform IGC. Longer ageing times (>5000 seconds) reduced the IGC susceptibility but none of the applied ageing heat treatments resulted in an alloy that was resistant to localised corrosion as was found for the air cooled variant. In the peak aged and overaged conditions the alloy exhibited slight localised IGC and then pitting.

Microscopy and EDX showed that large β phase precipitates were located at the grain boundaries of alloy A and alloy B on the control samples which had been air cooled. The higher copper alloy A also contained large Q phase grain boundary precipitates. No precipitates were visible on the water quenched samples without ageing.

IGC susceptibility was attributed to the presence of Q phase grain boundary precipitates and the copper rich film identified in [24]. It is noted that microgalvanic coupling between the cathodic copper rich grain boundary precipitates and the adjacent copper depleted zone is the likely mechanism causing the susceptibility. The low copper alloy B was generally resistant to IGC despite the presence of only β phase grain boundary precipitates showing that their presence alone does not lead to IGC susceptibility.

The mechanism by which the IGC susceptible higher copper air cooled samples are made more resistant by ageing is thought to be based on the coarsening of the copper rich film to make it discontinuous as well as the increase in precipitation within grains as described in [24].

This paper describes new effects which were not covered in the previous papers [16, 24, 25]. Firstly, the main set of samples which were solution heat treated before ageing were seen to be generally more susceptible to corrosion in both the air cooled and water quenched conditions than the samples in the control set. Secondly after being made corrosion resistant at approximately peak ageing, overageing of the main set of samples did not lead to pitting, instead IGC was re-introduced. Microscopy revealed that this IGC was slightly different to the IGC seen in the underaged alloy; it was more localised and the grain boundary attack was coarser, not 'knife edge attack' as described previously and for the underaged samples in this study. It is this type of IGC that is more like pitting in nature and is controlled by bulk as well as grain boundary properties.

Intergranular Corrosion of Copper-Containing AA6xxx AlMgSi Aluminium Alloys

[61]

Larsen et al carried out a study [61] with the aim of providing detailed analysis of grain boundary microstructure of AA6000 series alloys. One of the alloys (alloy A) used was similar to the low Cu alloy in [16] and another (alloy B) to the higher Cu alloys used in [25] and [24]. An additional alloy (alloy C) with a high copper content of 0.7% was also used, this is a similar copper content to AA6111. The complete compositions of these alloys are given in Table 1.5.

Alloys A and B were extruded in a laboratory press whereas alloy C was provided as a rolled sheet and was primarily used because its high copper content facilitated compositional analysis at the grain boundary. All of the materials were solutionised at 540°C for 30 minutes and all were then water quenched. In addition to the as-quenched samples, ageing heat treatments were applied to the materials in the T4 condition to provide underaged (42 minutes at 185°C), peak aged or T6 (5 hours at 185°C) and overaged (24 hours at 185°C) samples. The heat treatment for the underaged condition is similar to that applied during 'paint baking' of automotive body sheet. Corrosion testing was carried out in accordance with British Standard BS-ISO 11846 [62].

Samples of alloy A were found to be resistant to IGC in the tempers tested. Alloy B corroded in the T4 condition but the attack was not intergranular. Alloy B was very susceptible to IGC in the underaged condition, in the T6 and overaged condition it was less susceptible, the IGC attack was more localised and did not penetrate to such a depth. These water cooled samples were not found to be completely resistant to IGC at any of the tempers tested whereas Svenningsen et al [16, 25] found that water cooled samples were resistant in the T4 condition and become slightly more susceptible when aged to the T6 condition.

The high copper alloy, 'Alloy C' was corrosion tested only in the underaged temper and was found to be highly susceptible to intergranular corrosion. SEM imaging of the samples revealed no grain boundary precipitates in the T4 or underaged conditions but they were present on the samples aged to the peak hardness and

overaged conditions. These particles were assumed to be of the Q phase. TEM characterisation which was repeated several times for each sample also found no grain boundary precipitates to be present in the T4 condition. TEM picked up small precipitates at the grain boundaries of the samples in the underaged condition, no Q' phase in-grain precipitates were found at this temper.

STEM imaging was used on the underaged tempers of alloys B and C and showed grain boundary precipitates of size 20-50nm. EDX analysis was consistent with the finding in previous work [25] that the precipitates were the quaternary Q' phase.

The presence of a copper rich grain boundary film was reported in this study for alloy B confirming the original discovery made in [24]. Again the film was only a few nanometers thick and EDX analysis showed it to contain little or no Mg or Si. In [24] it was stated that thermodynamic calculations indicated that neither elemental copper or an $AlCu$ phase should have formed at the ageing temperatures applied and so it was thought likely that the grain boundary film was composed of a precursor to the Q phase. The authors of this paper argue that it is more likely to be a non-equilibrium phase of either a supersaturated solid solution of copper or $AlCu$. The absence of Mg and Si in the grain boundary film is explained by their high mobility at grain boundaries compared to copper allowing these elements to diffuse to form the Q' phase precipitates which were identified there. Cu is 'left behind' and this preserves continuity in the film.

The presence of the copper enriched film is said to be the cause of IGC in the underaged temper. It is thought that copper depletion adjacent to grain boundaries occurs, this should act to increase the potential gradient between the grain boundary film and the adjacent matrix and exacerbate IGC. However the techniques used in this study were only able to reveal a copper depleted zone in the high copper alloy 'Alloy C'. The grain boundary film was not so apparent on samples in the peak-aged and overaged condition and this was thought to be the reason for the improved IGC resistance of these samples. The localised IGC observed was thought to be as a result of attack occurring preferentially at those grains with the most copper enrichment but not others. The extensive precipitation of Q' phase

within grains was also thought to reduce susceptibility by decreasing the dissolved copper concentration in the matrix and therefore decreasing the potential gradient between the grain boundary solute depleted zones and the solid solution in the bulk grains.

Grain boundary solute depletion was also studied in this work using EDX profiles. A sample of underaged Alloy B was found to be depleted in Si adjacent to the grain boundary but copper depletion was not detected, possibly because of the detection limits of the equipment with this relatively low copper alloy. A slight Mg depletion was detected. An EDX profile across a grain boundary of the high copper Alloy C did show clear depletion either side of the grain boundary with a copper spike in-between. Alloy B was resistant to IGC in the T4 temper but showed slight copper enrichment and also some Si enrichment at the grain boundaries. No enrichment of Si was found to be present at the precipitate-free regions of the grain boundaries of alloy B after artificial ageing. No magnesium and silicon containing phases were found to be present at the grain boundaries of any of the samples.

Table 1.6 summarises the copper content, magnesium to silicon ratio, quench rate and ageing temperature for the alloys used in the series of papers which have just been reviewed [16, 24-26, 61]. The reported corrosion susceptibility of each alloy in a range of ageing conditions is shown.

		At.%Cu	Mg:Si	Quench	T/°C	T4	Underaged	Peak	Overaged
High Cu		0.0511	1.00	AC		Uniform IGC		Localised IGC	
High Cu		0.0511	1.00	WQ	185	Slight localised corrosion		Localised IGC	
Low Cu		0.0002	0.71	AC		Slight localised corrosion		No localised corrosion	
Low Cu		0.0002	0.71	WQ		No localised corrosion		No localised corrosion	
Model Alloy		0.0553	1.06	AC	Ambient	Uniform IGC			
Model Alloy		0.0553	1.06	AC	140		Uniform IGC	Uniform IGC/Localised IGC	No localised corrosion then pitting
Model Alloy		0.0553	1.06	AC	185		Uniform IGC then localised IGC	No localised corrosion then pitting	Pitting
Model Alloy		0.0553	1.06	AC	220		Uniform IGC	No localised corrosion	Pitting
A		0.0724	1.06	AC		Uniform IGC		Localised IGC	
A		0.0724	1.06	WQ	185	Slight corrosion		Pitting and localised IGC	
B		0.0085	1.04	AC		Slight IGC at surface		No localised corrosion	
B		0.0085	1.04	WQ		No localised corrosion		No localised corrosion	
A		0.0085	0.98	WQ		No corrosion	No corrosion	No corrosion	No corrosion
B		0.0766	1.00	WQ	185	Superficially etched, no IGC	Extensive IGC	Slight localised IGC	Slight localised IGC
C		0.2991	0.88	WQ			Extensive IGC		

Table 1.6 Summary of corrosion susceptibility and condition of alloys [16, 24-26, 61]

1.6 Deformed Surface Layers

Deformed surface layers (DSLs) are usually formed as a result of either rolling or mechanically grinding aluminium. It has been reported [73] that perfect correlation has been found between field corrosion and mechanical grinding, resulting in the recommendation that such rectification should be minimised in areas that are susceptible to stone chip damage. Grinding applied to other areas is not as likely to be a problem because a break in the coating is required for corrosion to occur.

The difference in the thermo-mechanical treatment of the DSL compared to the bulk results in it having a distinct microstructure which can create dissimilar physical and electrochemical characteristics. The main feature of a deformed surface layer is its fine grain size compared to the bulk. Oxide and other inclusions can become incorporated in the DSL during its formation. When heat treatments are applied the type, size or number of intermetallic phases that precipitate in the DSL can be different to that of those that precipitate in the bulk. The nature of intermetallic particles already present near the surface of the alloy can be changed as a result of DSL formation.

1.6.1 Morphology

The two main processes that lead to the creation of DSLs are rolling during sheet production and grinding which is often applied during rectification of defects. Grinding is often used to produce DSLs in the laboratory.

In a study by Liu et al [74] a near surface deformed layer was identified after mechanical grinding and heat treating a sample of AA6111 at 180°C for 30 minutes; this layer was approximately 2µm thick and comprised very fine grains with diameters in the range 50-150nm. In automotive applications surface rectification (grinding) is often carried out on the body-in-white. The resulting deformed surface layers are several microns thick [73] and consequently are not always removed by the final cleaning and pre-treatment processes. In another study [75] an as received

sample of rolled AA8006 sheet was found to have damaged surface layer of thickness 0.3 to 0.6 μm , with bulk grain size of 5 to 50 μm and deformed layer grain size 20-200nm; the DSL grains were found to be identical to those in the bulk in terms of structure and composition and no grain boundary segregation was detected there. The deformed layer in the as-rolled AA3005-H19 alloy studied by Afseth et al [76] was found to be approximately 1 micron thick with grains sizes in the region of 50-200nm. The rolling induced DSL grain size range reported in the previous two studies is very similar to that in [74] where the DSL was produced by mechanical grinding. However, there were significant differences in the thickness of the DSLs in the three studies, the ground DSL was at least double the thickness of the rolled DSLs. It is thought that rolling-induced deformed surface layers are created during hot rolling and that subsequent cold rolling can reduce the thickness of or break up the surface layer [73]. Thinning of the DSL during cold rolling is advantageous; it results in etch cleaning operations being much more effective because the layer can be much more easily removed [73]. For a given final gauge, increasing the transfer gauge thickness will reduce the thickness of the DSL on the cold rolled final product because more of the reduction will take place during cold, as opposed to hot rolling. This allows more spreading and thinning of the DSL to occur [3]. Fishkis and Lin [77] reported the extent of the subsurface layer following hot rolling to vary between about 8 μm after the first pass to 1.5 μm after the sixth. It was reported that the majority of the surface layer development took place during the early stages of rolling and later passes resulted in less damage but the deformed layers formed earlier were distributed over a larger surface area [77].

As well as reducing the transfer gauge, substituting the traditional DC casting production method with continuous casting can reduce the problem of deformed surface layers. This method completely removes the need for hot rolling [3]. This does not, however, solve the problem of re-introduction of DSLs as a result of mechanical grinding during rectification.

1.6.2 Formation

Generally the formation of DSLs is attributed to the increased shear stress experienced at the surface of the metal during hot rolling or mechanical grinding. Hot rolling of aluminium alloy sheet results in a deformed surface layer, due to cracking, folding and re-welding, as the surface metal is smeared at the roll bite [73].

Fishkis and Lin [77] found results which substantiated the following three step process of subsurface structure formation during rolling. First the formation of surface depressions (holes) by ploughing, adhesive wear, delamination wear or transverse surface cracking in the process of rolling; secondly, the filling of holes with the wear debris consisting of metal and oxide fines mixed with lubricants; finally the covering of holes with thin metal layers during the continuing rolling process leading to a shingled surface appearance.

The difference in the nature of the intermetallic particles has also been attributed to the deformation processes that occur during rolling. In a study of AA3005 Afseth et al [78] identified a near surface region of material containing a smaller number of the larger constituent intermetallic particles than the underlying bulk but a higher density of fine, dispersoid particles. He attributed this difference to the smearing and breaking up of intermetallic particles during rolling and to enhanced secondary precipitation of fine dispersoid particles in the layer during high temperature exposure, such as hot rolling and/or annealing.

Afseth et al state that enhanced shear deformation, near the alloy surface, that occurs as a result of rolling [76] during aluminium alloy sheet production and/or as a result of surface grinding can produce a near surface layer which has characteristics different to those of the bulk. Different grain sizes, intermetallic particle distribution and oxide inclusions in the deformed surface layer were reported in another study by the same authors [79]. Small grains and microcrystalline and amorphous oxides were found [77] in the near surface layer of hot rolled magnesium containing aluminium alloys.

Another study [75] found a nano-crystalline deformed surface layer of thickness 0.3 to 0.6 μm to be present. In this case it was suggested that its formation could be due to interfacial forces generated by oxide growth following annealing.

1.6.3 Thermal Stability

Deformed surface layers on aluminium alloys tend to be thermally stable; the diameter of the grains in the DSL does not usually increase as a result of heat treatments applied after their formation. Liu et al [74] reported the nano-grained near surface deformed layer to be stable during heat treatment at 180°C. This was attributed to the large fraction of high-angle grain boundaries and the pinning action of the *Q* phase precipitates resulting in Zener drag.

Elements in solid solution and intermetallics can act as grain refiners. Oxides and lubricants mixed into the surface during rolling may pin the sub-grain structure [80]. This suggestion was also made in another study [77] which found a subsurface layer consisting of a mixture of small grained metal with micro crystalline and amorphous oxides in all the hot rolled magnesium containing aluminium alloys which were examined. Here, it was proposed that 'The small metal grain size in the surface layer was most probably stabilised through Zener pinning of the grain boundaries by the small oxide particles'. It has been suggested however [78] that cold rolling alone without the initial hot rolling step does not incorporate the oxide particles necessary for Zener pinning of the refined grain structure in the deformed surface layer.

1.6.4 Precipitation in the DSL and Corrosion Susceptibility

Heat treatments such as precipitation hardening and annealing can have different effects on the surface layer compared to the bulk. A number of studies [73, 76, 78, 79, 81, 82] have produced evidence of preferential precipitation in the deformed surface layer as a result of heat treatment.

Scamans [73] used transmission electron microscopy to show that the deformed layer grain boundaries acted as sites for the preferential precipitation of intermetallic particles during natural ageing, these were found to be Mg_2Si in the Al-Mg-Si alloy AA6016 and Q phase in the Al-Mg-Si-Cu alloy AA6111. Also on AA6111, Liu et al [74] found that precipitation in the deformed surface layer differed from that in a sample of normal grain size. On ageing at 180°C for 30 minutes, preferential precipitation of Q phase particles occurred, again preferentially at grain boundaries within the deformed surface layer, this was reported to have taken place without the development of metastable precursor phases. No precipitates were found within the DSL grains.

Both of the studies on AA6000 series alloys [73, 82] reported that corrosion susceptibility was increased as a result of the nature of precipitation within the DSL. This was attributed to micro-galvanic coupling between the cathodic grain boundary precipitates and the adjacent solute depleted zones. The depleted zones are said to act as preferred pathways for corrosion propagation. Liu et al [74] also state that micro-galvanic coupling between the Q phase precipitates and the aluminium matrix adjacent to the particles in the near surface deformed layer had increased filiform corrosion susceptibility compared with the bulk.

The precipitation within the DSL has also been reported to be different from the bulk for a number of alloys outside the AA6000 series. A group of papers by Afseth et al concentrated on the AA3005 alloy [76, 78, 79]. Again precipitation within the DSL was promoted with a dispersion of fine manganese and iron bearing intermetallics developing on heat treatment for 2 hours at 450°C. The density of intermetallic particles was greater than in the bulk grains. The DSL micro-grains were said to have contained a smaller number of the larger constituent intermetallic particles than the bulk. The enhanced precipitation was attributed to the high deformation undergone by the DSL. The work of Ambat et al [81] support the finding that there is enhanced precipitation of iron and manganese bearing intermetallics within the DSL of AA3005 after a similar heat treatment. It is suggested within this paper that these particles originate not only from nucleation and precipitation during heat treatment but also from the fragmentation of existing

particles. Leth-Olsen et al [75] suggested that there may have been magnesium enrichment within the DSL formed on an AA8006 sample which was heat treated for 2 hours at 440°C.

Studies [75, 80] have found that the purer alloys of the 1000 series are less prone to the formation of deformed surface layers following thermo-mechanical processing. It was suggested that this may be a result of the low recrystallization temperatures and/or shorter times required for recrystallization of these alloys and also that they may not have contained sufficient impurities to act as grain refiners.

Afseth et al [76, 78, 79] described the precipitation of second phases in the deformed layer as being 'deformation enhanced' and explained that it resulted in the adjacent matrix being depleted of noble alloying elements. Secondary precipitation has also been reported in a number of other studies: of manganese bearing intermetallic particles in AA3005 [79], of equilibrium phase intermetallic particles in 6000 series alloys at the grain boundaries [73], and of particular relevance to this study, of Q phase ($Cu_2Mg_8Si_7Al_4$) particles approximately 20nm in diameter in AA6111 [82], also at the grain boundaries. In the lower copper 6000 series alloy, AA6016, the grain boundary precipitates are of the Mg_2Si phase [73]. The kinetics of grain boundary precipitation in the deformed layer are reported to be significantly faster than that in the bulk [73].

Afseth et al [78] carried out corrosion testing on the commercial AA3005 alloy in the as-received condition, after etching to remove the DSL and after further cold rolling. The as-received material was found to have a high susceptibility to FFC which was increased by high temperature annealing. When the DSL was removed by etching the material had a good resistance to FFC and the sensitivity to heat treatment was removed. Subsequent heat treatment and cold rolling of the etched material re-introduced FFC susceptibility and sensitivity to heat treatment. Leth-Olsen [75] reported a similar phenomenon on AA8006 whereby re-annealing re-introduced FCC susceptibility which had previously been virtually eliminated by etching. In another study on AA3005 [79] by the same authors the mode of FFC was seen to change from successive pitting to superficial attack as a result of heat treatment. A

further study [76] which studied the effects of a range of heat treatment temperatures on FFC susceptibility showed that 350°C was a critical temperature and that heat treatment above this temperature resulted in severe FFC. A study on AA5754 by Afseth et al [79] found that this alloy did not exhibit the same behaviour and resistance to FFC was not significantly affected by annealing.

1.6.5 Etching

It is recognised that rolling-induced deformed surface layers lead to increased FFC susceptibility and as a result manufacturers have introduced an etch-cleaning process to remove the deformed layer. Afseth et al [78] found that good corrosion resistance was obtained by removing a surface layer of metal from AA3005 samples by chemical etching or mechanical polishing. In a study [75] of AA8006 which was received in a fully annealed condition, etching for 10s in 10% NaOH and then briefly dipping in concentrated nitric acid resulted in a surface with high resistance to FFC, whereas the as-received material was not resistant.

1.7 Environment

The environment in which the material is used or tested can be as important as or more important than its condition and composition. Exposure tests have shown a corrosion rate for steel of 5 µm per year in a rural region of Nigeria compared with 90 µm per year in an industrial region of the UK. Natural atmospheres can be classified as rural, urban, industrial or marine. Rural atmospheres are free from chemical pollutants; the main causes of corrosion are moisture, oxygen and carbon dioxide. The urban atmosphere has, in addition, oxides of sulphur and nitrogen. The industrial atmosphere can contain emissions of sulphur dioxide, chlorides, phosphates, nitrates etc. The marine atmosphere contains fine particles of sea salt

carried by wind. These complex environments include a number of factors which can be considered and controlled separately in the laboratory.

1.7.1 Humidity

Aluminium does not corrode unless water is present on the surface. Generally high purity water at ambient temperature will not lead to corrosion but in natural environments the water will contain impurities. There are a number of ways in which water can make contact with the metal surface and these will have different effects. Heavy rainfall can have a beneficial effect by washing away contaminants. Generally contact with water will be detrimental; if the metal is submerged in an aqueous solution, if there are isolated droplets on the surface or if a thin film condenses on the surface, then corrosion can occur. There is a critical relative humidity below which no corrosion will occur; this is approximately 60% for all metals. Above this value corrosion rates will generally increase, the type of corrosion may also change. FFC rarely occurs below about 55% RH and occurs most readily between 85 and 95% RH.

1.7.2 Oxygen

Oxygen must also be present for corrosion of aluminium to occur. Water which is in contact with the aluminium surface and with the air will contain dissolved oxygen. A thin film of moisture is easily saturated with oxygen from the atmosphere therefore the corrosion process is not limited by the cathodic reaction i.e. the reduction of oxygen or the evolution of hydrogen.

1.7.3 Temperature

Increasing temperature results in an increase in the reaction rate. Generally every 10°C rise in temperature approximately doubles the rate of reaction but in the case of corrosion this effect may be limited by the decrease in the solubility of oxygen at higher temperatures. Even though reaction rates will tend to be faster at higher

temperatures, complete drying of the surface by heating will cause the corrosion to stop altogether.

Temperature has another effect on corrosion; when the temperature falls below the dew point, the air becomes saturated and condensation will occur on the metal surfaces. Internal surfaces can be affected and these will tend to dry less easily.

1.7.4 pH

As shown in the Pourbaix diagram (Figure 1.6) the oxide film is generally stable in the pH range 4-9 and corrosion occurs in stronger acids and alkalis. There are, however some exceptions to this; aluminium is highly resistant to concentrated nitric acid and concentrated ammonium hydroxide for example.

1.7.5 Electrolyte

The contaminants present, and their concentration in the electrolyte determines its conductivity which in turn affects the rate, severity and nature of the corrosion. Metals such as aluminium, which rely on the on the formation of passive films to protect them from corrosion tend to be unstable in chloride environments. Chloride anions locally disrupt the oxide layer, often at pre-existing weak points and this can initiate pitting.

1.8 Standard Accelerated Filiform Corrosion Tests

The rate of filiform corrosion is dependent on the humidity and temperature of the environment and on the presence of salt. These factors are employed as accelerators in many of the standard tests. ASTM D 2803 [83] 'Standard Guide for Testing Filiform Corrosion Resistance of Organic Coatings on Metal' describes three tests for the susceptibility of organically coated metals to filiform corrosion. The three tests involve different methods of exposing scribed panels to salt and they are

carried out in different relative humidities. In procedure A the scribed panels are placed in a salt spray cabinet to initiate the corrosion, rinsed and placed in an environment chamber maintained at approximately 25°C and 85% relative humidity. In procedure B the scribed panels are either sprayed with, or dipped in, a salt solution, but not rinsed before being placed in the environment chamber. Procedure C is similar to procedure A, but with a temperature of approximately 40°C.

Cyclic tests involving the use of alternating wet and dry periods have been developed to more closely replicate environmental conditions and are becoming increasingly popular. Generally these tests rely on the use of specialist computer controlled cabinets which can be programmed to vary a wide range of conditions cyclically. One such system is the cyclic TNO corrosion testing chamber which was employed to test the samples provided for this study.

Painted panels are most susceptible in marine environments when they are mounted vertically, face north and are protected by an overhang which prevents rain from washing away accumulated salt deposits. Cabinet tests can be useful indicators of corrosion susceptibility under certain conditions but they fail to replicate these conditions [3].

Most tests for coated aluminium involve acidic environments. These include the Lockheed and Acetic Acid Salt Spray (AASS) tests. The Lockheed test (DIN 65472 [84]) involves scribing 5cm defects in the test panels, these defects should penetrate the coating to reach the substrate. The panels are then exposed to a vapour of chloridric acid for one hour before being placed in a humidity chamber at approximately 82% relative humidity and approximately 38°C. AASS testing involves exposure of samples to a 5% NaCl salt spray which is acidified using acetic acid to a pH of approximately 3.2. This takes place at 35°C. This procedure is described in ISO 9227 [85].

1.9 Electrochemical Techniques

Many techniques are available for investigating corrosion at solid/liquid and solid/gas interfaces. The most basic of these are DC techniques which measure the potential of a surface against time. Potentiodynamic techniques allow the current to be measured as a function of a varying applied potential.

In order to provide more information on corrosion processes, AC techniques were developed. One of these was electrochemical impedance spectroscopy (EIS) which involves applying an alternating voltage to the sample or working electrode, measuring the current and calculating the impedance. EIS does not provide spatially resolved data, it can only provide an average measurement over an area of the sample. The next step in the development of these electrochemical techniques was to enable localised measurement. Localised electrochemical impedance spectroscopy (LEIS), scanning reference electrode technique (SRET), scanning vibrating electrode technique (SVET), scanning Kelvin probe (SKP) and scanning Kelvin probe force microscopy (SKPFM), are all capable of this and make it possible to map the potentials and to resolve small anodes and cathodes on the surface of corroding metals.

LEIS is an extension of EIS except that an electrochemical probe is scanned a small distance from the surface of the sample. SRET involves scanning two closely spaced reference electrodes across the sample in solution and measuring the potential difference between them. SVET, which will be discussed in detail later, differs from SRET in that the probe vibrates relative to the sample surface; it has a reference electrode which is placed in the solution but is distant from the probe. SVET is more sensitive and is capable of higher resolution than SRET. SKP, which will also be discussed in detail later, differs from most electrochemical techniques in that no bulk electrolyte is required. SKPFM works in the same way as SKP but provides much higher resolution as a result of its smaller tip and is also capable of topographical measurement. Rohwerder and Turcu [86] reviewed existing literature and concluded that SKPFM was more prone to producing artifacts than SKP.

1.9.1 Scanning Vibrating Electrode Technique

SVET requires the sample to be immersed in an electrolyte. Points of anodic activity will develop as a result of corrosion. If we regard the associated cathode to be infinitely distant, the flow of ionic current will radiate from the anode as shown in Figure 1.9.

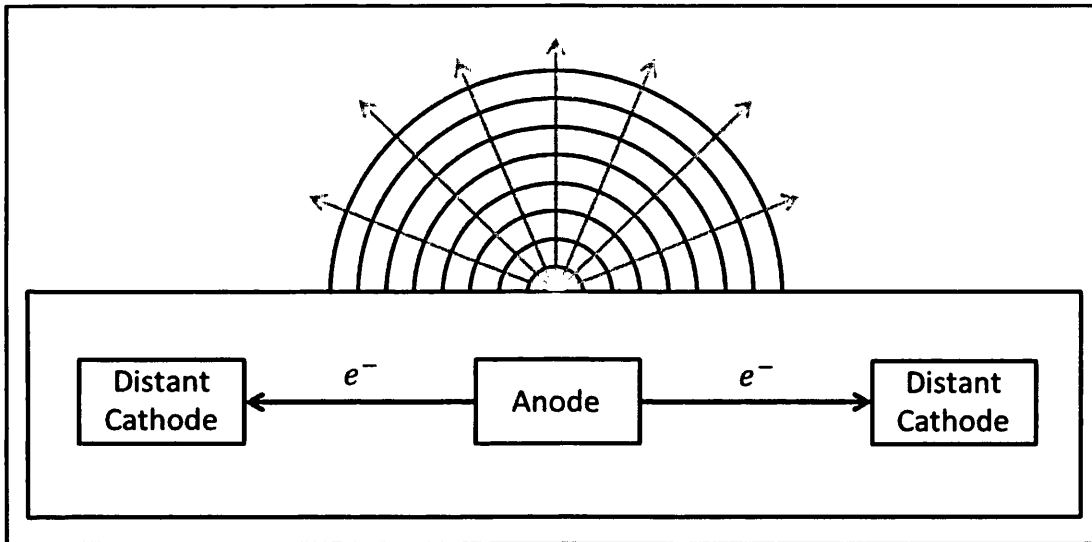


Figure 1.9 Ionic current associated with an anode when the associated cathode is infinitely distant.

The SVET tip vibrates in the electrolyte normal to the surface of the sample with fixed amplitude, frequency and average height. The resistance of the electrolyte to the ionic current is high compared to the resistance of the metal sample to the flow of electrons. This creates an ohmic potential gradient in the electrolyte. Lines of equal potential are shown in Figure 1.9. The path of the SVET tip intersects these lines creating an alternating potential signal; this signal is proportional to the vertical component of the current density in the electrolyte at the tip.

Isaacs and Vyas [87] show that the Laplace equation (Equation 1.19) can be used in combination with Ohm's law (Equation 1.20) to determine the electrical potential E :

Equation 1.19

$$\nabla^2 E = 0$$

Equation 1.20

$$i = -k\nabla E$$

where i is the current and k is the conductivity of the electrolyte.

It is only possible to find the solution of this pair of simultaneous equations for a point current source model. Isaacs [88] shows that the potential at the point (x,y,z) is given by:

Equation 1.21

$$E = \frac{i}{2\pi\sqrt{(x^2 + y^2 + z^2)}}$$

The SVET cannot measure the current density at the surface, it measures the vertical component of current density at the tip.

The normal field strength is given by:

Equation 1.22

$$F = \frac{dE}{dz}$$

so that for the point current source we get:

Equation 1.23

$$F = \frac{iz}{2\pi k(x^2 + y^2 + z^2)^{\frac{3}{2}}}$$

and the maximum field strength, F_{max} , which occurs when the tip is directly above the point current source i.e. $x = 0, y = 0$, is given by:

Equation 1.24

$$F_{max} = \frac{i}{2\pi k z^2}$$

1.9.2 Scanning Kelvin Probe

SKP is particularly useful for measuring potentials associated with filiform corrosion on polymer coated metals because there is no need for a bulk electrolyte and it is capable of functioning through the coating. It is also a non-destructive and non-contact technique so there is no interference with the sample or the corrosion processes. SKP is also an in-situ technique meaning potential measurements can be made across the scan area whilst corrosion is occurring, these scans can be repeated during the corrosion process allowing the time dependent behaviour to be recorded.

The minimum work that is required to extract an electron from within a material to just outside that material is known as the work function. The SKP measures the work function and it has been shown this can be correlated to various aspects of the condition of the surface including the corrosion potential [89, 90]. The technique can therefore be applied to a number of areas of corrosion science such as corrosion inhibition, coating degradation, corrosion initiation and localised corrosion.

Two different metals will have different work functions and each work function will be the sum of the chemical potential and the surface potential. The difference between the work functions of the metals will cause electrons to flow from the material with lower work function to the material with higher work function when they are electrically connected. Current will continue to flow until the Fermi levels are equal. The resultant potential difference between the two metal surfaces is known as the Volta potential difference. When using an SKP to study the corrosion of a sample the tip is one of the metals (usually gold) and the sample is the other metal.

The Kelvin probe tip and the sample can be regarded as forming a parallel plate capacitor. The capacitance, C , is given by:

Equation 1.25

$$C = \frac{\epsilon \epsilon_0 A}{d}$$

where ϵ_0 is the dielectric constant, ϵ is the dielectric permittivity of the air between the tip and the sample, A is the tip area, d is the distance between the tip and the sample.

The tip position varies with time, t , as it vibrates perpendicular to the sample surface, around its average position $d = d_0$ with amplitude d_1 , and frequency ω radians:

Equation 1.26

$$d = d_0 + d_1 \sin \omega t$$

This current, i , can be expressed as:

Equation 1.27

$$i = \frac{dQ}{dt} = \Delta E \frac{dC}{dt}$$

If an external voltage E_s is applied between the sample and the tip then [91]:

Equation 1.28

$$i = (\Delta\psi - E_s) \frac{dC}{dt}$$

where $\Delta\psi$ is the Volta potential difference.

In order to measure the Volta potential difference, the voltage E_s is changed until the current is nullified. This will occur when

$$E_s = \Delta\psi.$$

When the surfaces of the metals are perfect and in a vacuum, the Volta potential difference is equal to the difference in work functions and Stratmann [89, 90] demonstrated that the corrosion potential E_{corr} is given by:

Equation 1.29

$$E_{corr} = \left(\frac{\phi_1 - \phi_2}{e} \right) + \text{constant}$$

where $\phi_1 - \phi_2$ is the measured work function difference between the tip and the sample. The constant is evaluated by calibrating the SKP using a reference electrode of known equilibrium potential.

Chapter 2: Filiform Corrosion of Aluminium

Alloy AA6111

2.1 Introduction

Alloys in the AA6000 series are relatively corrosion resistant however the precipitation of second phase particles tends to increase their susceptibility to intergranular corrosion [16, 24-26, 61]. After ageing at 180°C for between 0.5 and 11h two precipitating phases coexist, monoclinic β'' (Mg_2Si) and hexagonal Q phase ($Cu_2Mg_8Si_7Al_4$)[54]. It is thought that copper rich Q phase precipitates which form at grain boundaries behave as local cathodes and couple micro-galvanically with the adjacent Cu and Si depleted zones and that this causes increased intergranular corrosion susceptibility [16, 24, 25]. After paint baking AA6000 series alloys remain in the underaged condition and it is thought that they develop an almost continuous Cu-enriched grain boundary film. This film maximises intergranular corrosion susceptibility. If further ageing occurs then the grain boundary film tends to break up producing discrete Q phase particles and intergranular corrosion susceptibility is reduced [61].

Before any selective dissolution of Mg occurs both β'' and Q phase particles exhibit Volta potentials which are lower than that of the aluminium matrix. This has been shown using Scanning Kelvin Probe Force Microscopy (SKPFM) on AA6005. In these circumstances it was shown that the Volta potential of the β'' phase is 0.2V lower and the Volta potential of the Q phase is 0.075V lower than the matrix [92]. These Volta potentials were measured in air and so cannot be used to directly predict the rate of electrochemical reactions in aqueous solution. However they do suggest that in an aqueous electrolyte of $pH < 10$, where rapid magnesium dissolution is possible, Q phase particles will initially be anodic with respect to the matrix. Dissolution of Mg and Al from these precipitates would cause them to become enriched in Cu and they would therefore be expected to switch to cathodic behaviour. The presence and amount of copper is thought to be an important factor in determining the

corrosion susceptibility of aluminium alloys and has been shown to accelerate the corrosion rate of AA2024-T3 beneath scribed paint films by promoting the cathodic reaction, the reduction of oxygen [93]. Confocal laser scanning microscopy studies of organically coated AA2024-T3 have also suggested that intermetallic particles play an important role in accelerating corrosion by providing sites for electrochemical activity beneath the disbonding coating [94].

Structural failure of AA6000 series automotive body panels is unlikely to occur as a result of bulk intergranular corrosion but filiform corrosion (FFC) can lead to serious cosmetic failure [32, 33]. Shear deformation of the surface of aluminium alloys is now well known to produce a surface microstructure very different to that of the bulk [42, 74, 77, 79-81, 95-99]. These regions contain grains which are submicron [100] in size and second phase particles which pin the grain boundaries preventing them from recrystallising. DSLs are usually only a few microns thick but cause a significant increase in the rate of FFC. It has also been shown that the precipitation of intermetallic phases is increased in DSLs when artificial ageing is performed [34, 74, 79-81, 95-99, 101]. DSLs are usually present on AA6000 series aluminium sheet after rolling as a result of the increased shear forces applied to the surface in the rolling mill [102]. In order to maintain the corrosion resistance of the sheet manufacturers usually etch them using either an alkali or acid cleaner which removes the DSL. When AA6000 series aluminium sheet is press formed to produce the automotive body panels, the manufacturer will often rectify surface defects by mechanical grinding [101]. This re-introduces a DSL to the rectified area making it susceptible to FFC once again [34, 101, 103, 104]. Work has been carried out simulating the mechanical grinding used to remove surface defects on AA6111 by abrading its surface with silicon carbide (SiC) paper. The samples produced by this method were used to study the DSL on this material and the morphology of the FFC that developed [74]. This study concluded that there was a sharp transition from the bulk material to the DSL which contained grains with diameters between 50nm and 150nm. The thickness of the DSL in this case was approximately 2 μ m. Second phase particles were not resolved by Transmission Electron Microscopy (TEM) in the bulk either before or after heat treatment at 180°C for 30 minutes. However second

phase particles were seen to have developed in the DSL after the heat treatment. These particles located at the boundaries of the micrograins and were identified as Q phase precipitates by EDX analysis. The diameter of the Q phase precipitates was approximately 20nm. It was found that the micrograins did not coarsen as a result of the heat treatment. When the heat treated DSL-bearing samples were coated, scribed, inoculated with aqueous HCl and incubated at 40°C (as described in BS EN ISO 4623,2004[105]) a rapid-onset FFC was observed which was limited to the depth of the DSL. Microscopy revealed that the mode of corrosive attack within the DSL was intergranular. The DSL was much more susceptible to FFC than the bulk and this was attributed to micro-galvanic coupling between the Q-phase grain boundary precipitates and the aluminium matrix [74].

In this work the sample preparation procedures used in the study mentioned above [74] are followed and it is assumed that the resulting DSL will have a similar morphology and dimensions. SKP potentiometry is used to measure the effect of heat treatment on the open-circuit potential of both bulk (non DSL-bearing) and DSL bearing AA6111 in humid air. The SKP is also used to follow the kinetics of chloride-induced FFC on organic coated AA6111 and to map the evolving potentials which are characteristic of the FFC localised corrosion cell. The SKP is well suited to the study of FFC because it is able to measure localised free corrosion potentials (E_{corr}) without the presence of a bulk electrolyte and through intact polymer layers [106-109]. The aim is to elucidate the mechanism(s) by which FFC occurs on AA6111 and to increase our understanding of the mechanism by which the presence of an DSL increases FFC susceptibility. SKP has already been used successfully to study filiform corrosion on AA6016 [101, 110, 111], AA6111 [106, 112] and AA2024 [38, 112-115]. FFC was initiated by applying a known amount of dilute aqueous HCl into the scribed defects in the organic coating. This method of initiation has been shown to provide good reproducibility [38, 101, 115]. All FFC kinetics are determined at 40°C so that results are comparable to previous work on AA6000 series alloys [74, 101].

2.2 Experimental Procedure

2.2.1 Materials

2.2.1.1 Metals

Aluminium alloy AA6111 (composition by weight: Al, Mg 0.76%, Fe 0.24%, Si 0.64%, Cu 0.77%, Mn 0.20%) was provided by Innoval in the form of 1mm thick A4 sized rolled sheets. The material was provided in the solutionised (at 620°C) and naturally aged T4 temper. The sheet had been alkali cleaned online to remove any DSL formed as a result of the shear forces associated with the rolling process.

Aluminium alloy AA1050 was provided by Novelis in the form of 50mm by 50mm coupons, approximately 1mm thick.

High purity aluminium (99.999wt%) was provided by Goodfellow Cambridge Limited in the form of 1mm thick, 50mm by 50mm coupons .

2.2.1.2 Polyvinyl-Butyral

Polyvinylbutyral-co-vinylalcohol-co-vinylacetate (PVB) of molecular weight 70,000 to 100,000 was obtained from the Aldrich Chemical Company in the form of a powder. PVB was chosen to allow direct comparison with previous research [101], as well as for its transparency, good adhesive properties, inertness and non-toxicity. PVB is also soluble in non-toxic solvents and here ethanol is used to dissolve the PVB powder to produce a 15.5 wt% ethanolic solution.

2.2.1.3 Other Chemicals

Sodium hydroxide, hydrochloric acid, ammonium sulphate, phenylphosphonic acid, camphorsulphonic acid, argon gas, chromic acid, phosphoric acid and nitric acid were all obtained from the Aldrich Chemical Company in analytical grade purity.

2.2.2 Preparation of Samples

The as received AA6111-T4 in the form of A4-sized aluminium sheets was degreased with acetone, and cut into 40mm x 40mm coupons.

The main method of sample preparation was as follows:

The as-received surface was removed by etching for 45 seconds in 10% (w/v) aqueous sodium hydroxide (NaOH) at 60°C. During this alkali etching process complex aluminium oxides and hydroxides are formed and some of these compounds and other intermetallics are insoluble in NaOH. It is necessary to remove them to prevent them from influencing results. For this reason the coupons were then desmutted for 30 seconds in concentrated nitric acid at approximately 25°C. This was followed by 2 minutes of abrasion with 180 grit silicon carbide (SiC) paper to introduce a DSL. For the first minute abrasion was carried out against the rolling direction and for the second in the rolling direction. The coupons which were to be used as bulk samples were again etched and desmutted, using the same method as before, to remove the abrasion induced DSL. All the samples were then rinsed with distilled water and allowed to dry in room air.

Some samples were heat treated to simulate the paint-bake process that is applied to aluminium car body panels. These samples were heated to 100°C, 180°C, 250°C or 350°C and held at that temperature for two hours and then cooled naturally in room air.

The combinations of surface and heat treatments are shown with their sample codes in Table 2.1.

Table 2.1 AA6111 Samples

Sample Name	Description	Surface Treatment	Heat Treatment
B25	'Bulk' T _{HT} = 25°C	Etch and desmut - SiC abrade - Etch and desmut	T4; Solutionised and naturally aged
B100	'Bulk' T _{HT} = 100°C	Etch and desmut - SiC abrade - Etch and desmut	Artificially aged for 2h @ 100°C
B180	'Bulk' T _{HT} = 180°C	Etch and desmut - SiC abrade - Etch and desmut	Artificially aged for 2h @ 180°C
B350	'Bulk' T _{HT} = 350°C	Etch and desmut - SiC abrade - Etch and desmut	Artificially aged for 2h @ 350°C
D25	'DSL' T _{HT} = 25°C	Etch and desmut - SiC abrade	T4; Solutionised and naturally aged
D100	'DSL' T _{HT} = 100°C	Etch and desmut - SiC abrade	Artificially aged for 2h @ 100°C
D180	'DSL' T _{HT} = 180°C	Etch and desmut - SiC abrade	Artificially aged for 2h @ 180°C
D350	'DSL' T _{HT} = 350°C	Etch and desmut - SiC abrade	Artificially aged for 2h @ 350°C

Narrow strips of adhesive tape were applied to the two edges parallel to the rolling direction. Next a glass rod was dipped in the PVB solution and placed against one of the un-taped edges of the sample before being dragged along the sample in a single movement. The bar coating method is illustrated in Figure 2.1. The coating was allowed to dry for 12 hours before the samples were placed in the SKP environment chamber. After evaporation of the ethanol from the PVB solution a dry PVB coating with a thickness of 30±5µm was left behind. The thickness was determined using a micrometer screw gauge.

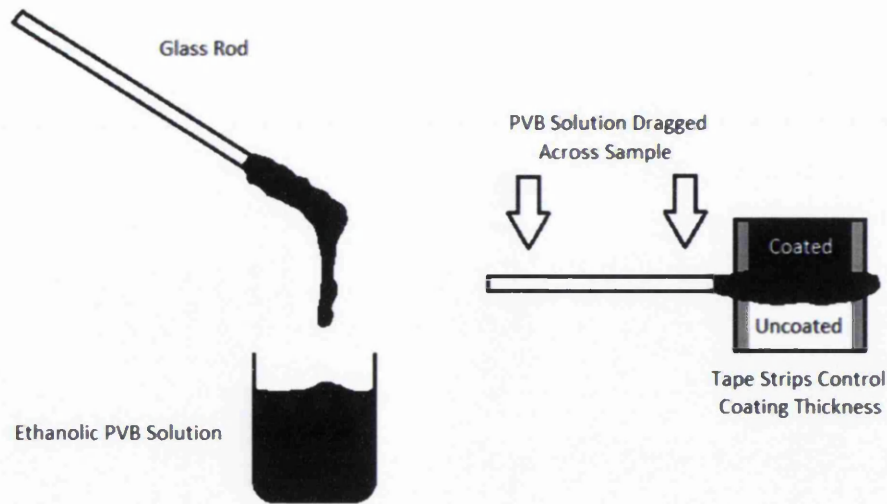


Figure 2.1 PVB Bar Coating Method

Other samples were specifically prepared for polarisation experiments. In this case samples of type B25, B180, B350, D25, D180 and D350 were prepared by the main method except that these samples were not coated. Instead, extruded poly(tetrafluoroethylene) adhesive tape (3490 3M Ltd.) was applied to the AA6111 coupons in such a way that all but a 10mm by 10mm square in the centre of the prepared side was protected from the electrolyte.

A third set of samples which comprised AA6111, AA1050 and pure aluminium 40mm by 40mm coupons was treated differently; the samples were first etched and desmuted as before and were then divided into two halves by a line drawn parallel to the rolling direction; one half was left in the as received condition, ('bulk') and the other half was abraded in the rolling direction for two minutes with 180 grit SiC paper to introduce a DSL. The method used previously, whereby the bulk condition was produced by creating and then removing the DSL, was not practical in this case because the etchant could not be prevented from affecting the DSL half of the sample.

2.2.3 Time-Lapse Photography

Saturated ammonium sulphate solution was poured into a desiccator to a level of approximately 2 cm. The gauze was placed above this and the sample was placed on the gauze. The desiccator lid was replaced with a piece of glass; an airtight seal was achieved by applying some grease where the glass sheet made contact with the desiccator rim. This allowed the desiccator to act as a humidity chamber. The camera rested, lens down, on the glass sheet. Figure 2.2 shows the setup of this apparatus. A Perspex air bath was placed over this whole apparatus to maintain the temperature at 40°C. The sample was lit using a halogen desk lamp to provide the maximum possible contrast in the images between the corroded and non-corroded area. The camera was connected to mains power. Software on a desktop computer was used to control the function of the camera via a USB cable. The software allowed the shot to be set up by setting the ISO, flash and focus. It also allowed the user to set the number of shots to be taken and the time interval between them. The usual procedure was to set the number of shots to 336 and the interval to 30 minutes. This meant that the experiment would run for 1 week allowing the corrosion to develop well. Once the experiment was over the photographs were cropped using photography software. 'Bink Video' software (version 1.9 by Rad Game tools) was then used to run the images together into a video. The frame rate was set to 8 frames per second to provide the optimum balance between the length of the video and its smoothness.

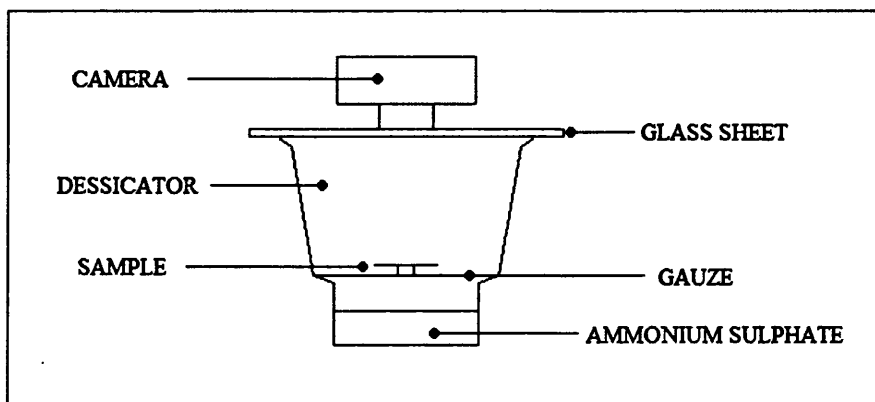


Figure 2.2 Optical time-lapse equipment setup.

2.2.4 Polarisation Measurements

Potentiodynamic polarisation experiments were carried out using a Solartron SI 1280 potentiostat and a gas-tight electrochemical cell consisting of a platinum gauze counter-electrode and a saturated calomel electrode. AA6111 samples were immersed in an electrolyte during these experiments. The electrolyte was near neutral (pH 6.0 - pH 6.5) 0.5% w/v aqueous sodium chloride. When required the electrolyte was de-aerated by sparging with argon gas. All potentiodynamic sweeps were carried out from -1.7 V vs SHE with a sweep rate of 5mV/s.

2.2.5 Defects

Defects were introduced into the PVB coated samples intended for FFC experiments. Two parallel 10mm defects, 13mm apart, running normal to the substrate rolling direction, were scribed through the PVB layer on each coupon using a scalpel. The dimensions and positions of the defects are shown in Figure 2.3 below.

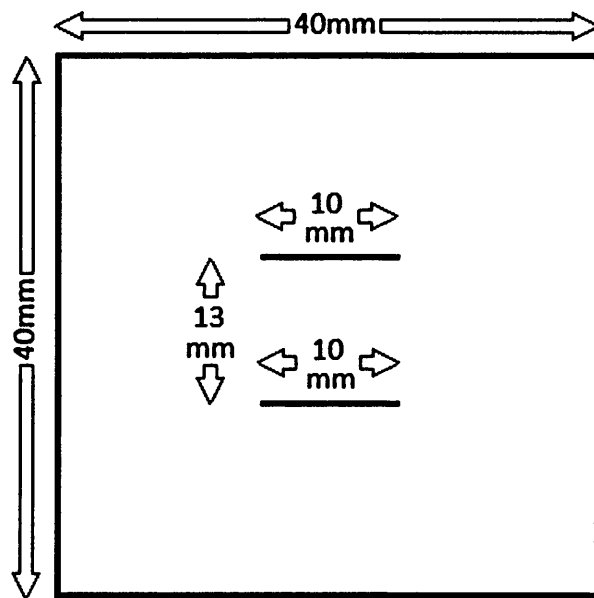


Figure 2.3 Dimensions and positions of defects on AA6111 coupons

2.2.6 Initiation

Where required, FFC was initiated using 1 μ l of 2 Molar hydrochloric acid. This was measured using a 10 μ l syringe, injected into a glass microcapillary and then introduced into the defect. Samples were then held in room air at approximately 25°C and 50% relative humidity for 30 minutes before being transferred to the SKP environment chamber.

2.2.7 Scanning Kelvin Probe

The principles of SKP potentiometry are discussed in Chapter 1. The more practical aspects are discussed below.

2.2.7.1 Construction

The SKP is used in this work was manufactured on site. The tip and sample are housed within an airtight steel environment chamber to allow humidity to be maintained (**Figure 2.6**). The environment chamber also acts as a Faraday cage to minimise the influence of external noise on the SKP signal. The environment chamber is heated by a Perspex air bath which has a thermostatically controlled heater, this air bath surrounds the environment chamber. Above the environment chamber is a magnetically driven loud speaker which faces downwards and is housed within a Mu-metal box. One end of a glass capillary tube is glued to the centre of the cone of the speaker. The lower end of this capillary tube is tapered and about half way down the tube there is a small hole machined in the side. The reference electrode (tip) of the SKP consists of a wire of 125 μ m diameter made out of 99.99% purity gold (**Figure 2.7**). One end of this wire is grounded by electrical connection to the steel environment chamber. The other end of the wire runs into the capillary tube through the hole, where it is attached to the capillary tube with

an adhesive, and out of the tapered end. The gold wire protrudes from the bottom of the capillary tube by approximately 15mm. A copper shroud surrounds the capillary tube and approximately 10mm of the protruding gold tip. The SKP probe assembly is shown in Figure 2.4 below.

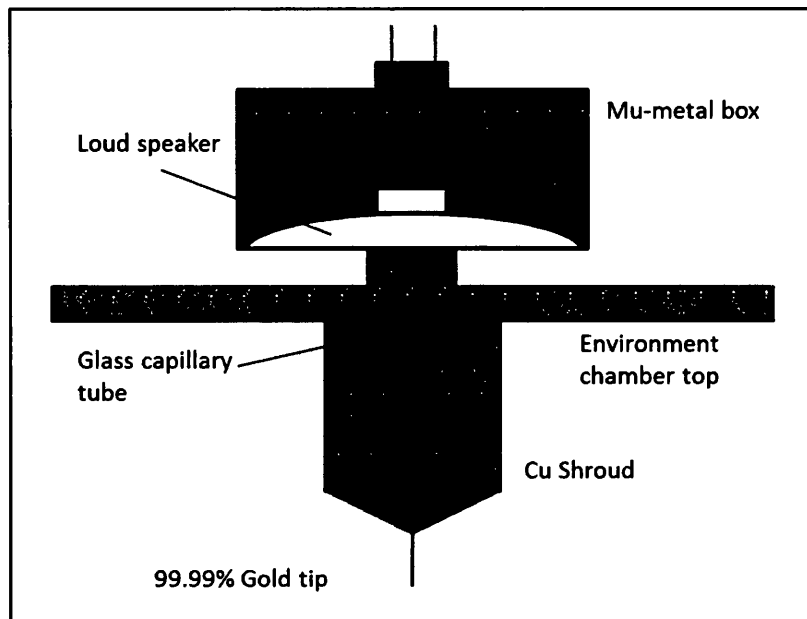


Figure 2.4 SKP probe assembly

A horizontal stage is centred beneath the tip. Nylon nuts are glued onto each sample allowing them to be screwed on to this stage. The samples are electrically connected to the SKP by a sprung steel pin which contacts the bottom of the sample through the nut. Samples can be levelled by pitch and roll adjustments controlled by two micrometer screw gauges. Levelling is important because it allows a constant tip to sample distance to be maintained during scanning. An arm connects the sample stage, through a hole machined in the side of the environment chamber, to another stage consisting of three orthogonally arranged x, y and z stepper motor driven linear bearings (Time and Precision Ltd). The stepper motor unit can be seen on the left of **Figure 2.5** below, the diagram also shows how it connects to the stage within the stainless steel environment chamber.

The lock-in amplifier (LIA) sends an alternating current to the loudspeaker at a frequency of 280Hz and this creates a sinusoidal vibration in the gold tip. The peak to peak amplitude of the vibration was 40µm and the mid-amplitude probe to

sample distance was $120\mu\text{m}$. The LIA also filters out any background interference frequencies.

The sample and the gold tip act as a parallel plate capacitor and so whenever a Volta potential difference exists between them, a charge will be present. The magnitude of this charge will be dependent on the potential difference between the plates and the distance between them. The distance between them is varied sinusoidally, as a result of the vibration of the tip and this creates an alternating current. This alternating current is amplified and converted into an alternating voltage by the trans-conductance amplifier. The LIA then produces a corresponding d.c. output which is sent to the integrator which acts as a feedback system to adjust the d.c. bias applied to the sample via the trans-conductance amplifier so as to automatically null the signal current. The magnitude of the reverse bias required is then converted into a digital signal to be stored by the computer. The magnitude of the reverse bias is equal to the Kelvin Probe Potential.

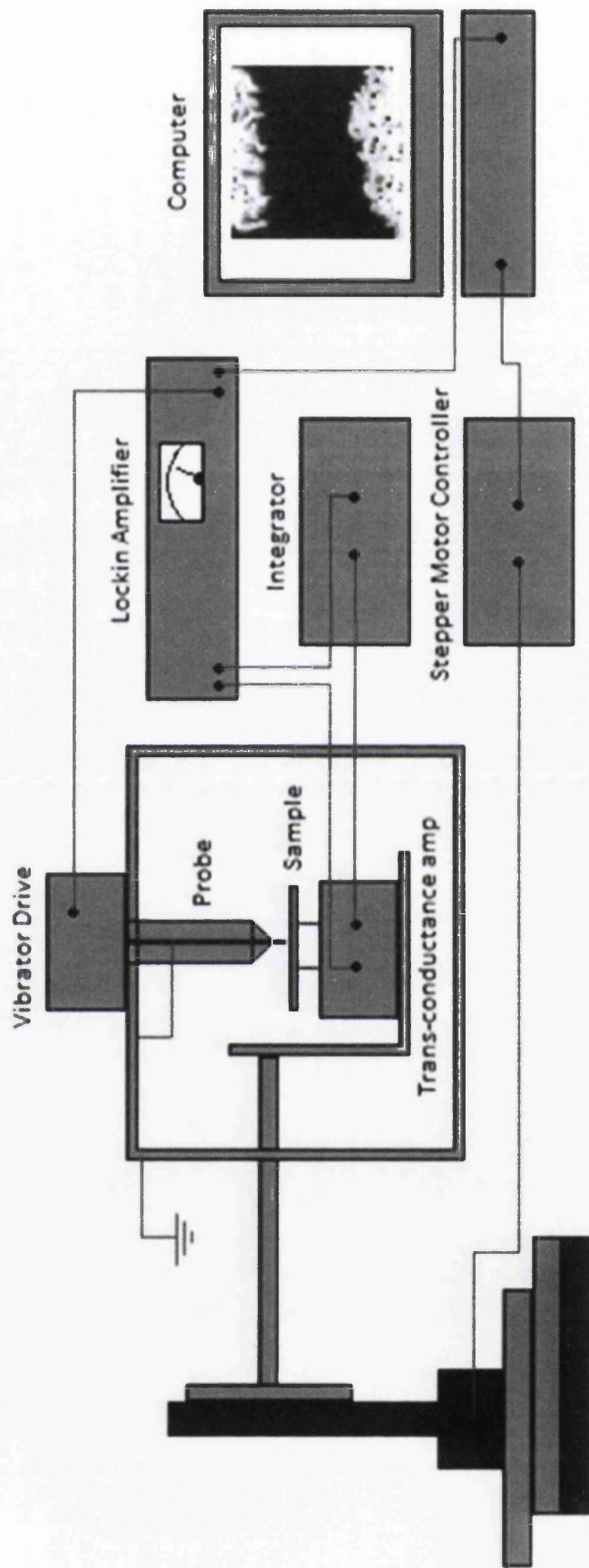


Figure 2.5 SKP equipment setup

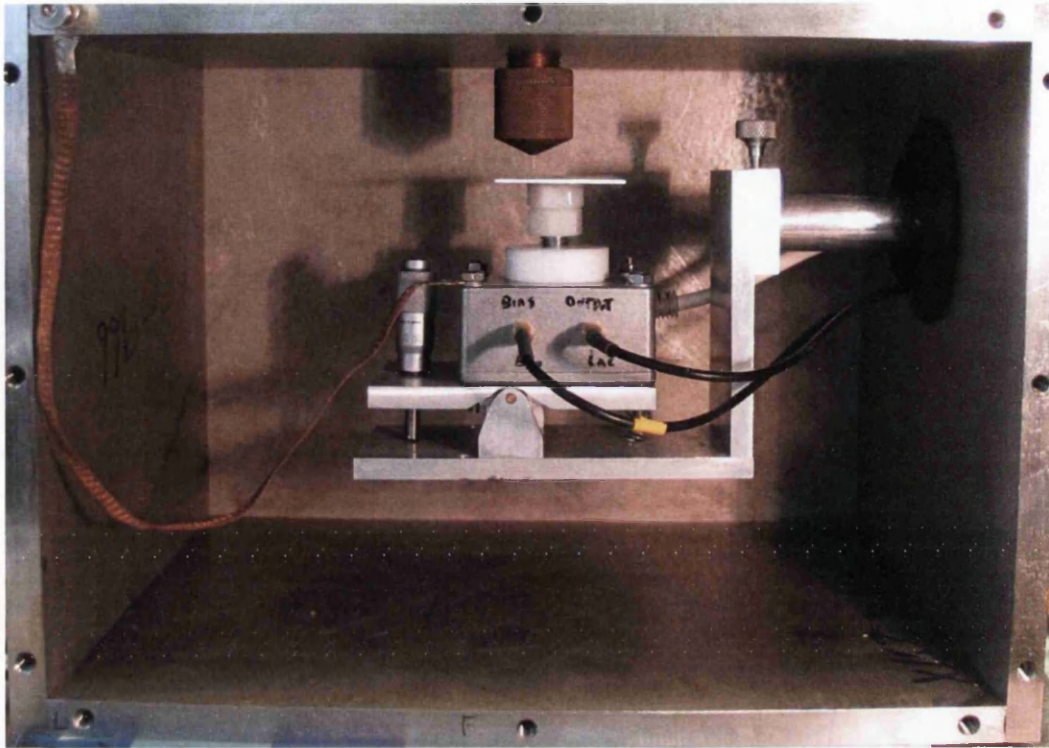


Figure 2.6 Sample, stage and tip inside the environment chamber

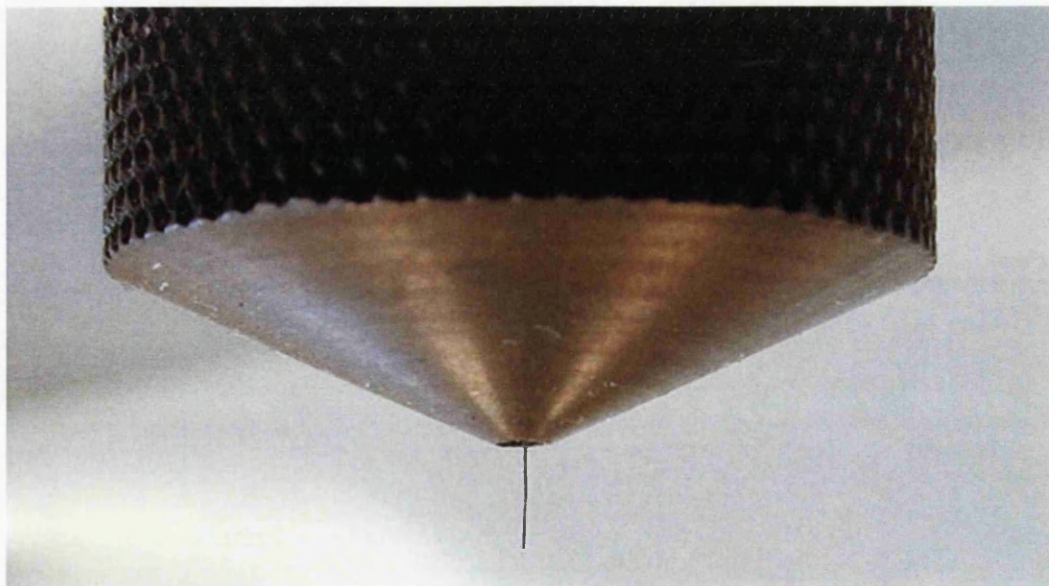


Figure 2.7 Gold SKP tip with the copper shroud

Unless otherwise stated all of the SKP measurements were made in an environment maintained at $40\pm 1^\circ\text{C}$ and $60\pm 2\%$ relative humidity. The temperature was controlled using an air bath surrounding the stainless steel environment chamber and the humidity was controlled using reservoirs of a saturated aqueous salt solution.

Scanning was started immediately after the samples had been screwed onto the stage and the environment chamber had been closed. The samples intended for the FFC experiments were scanned beneath the SKP tip such that the scan area was 12mm by 12mm. Scanning was continuous with a typical scan duration of 6 hours. The samples for the potentiometric characterisation and the half abraded samples were scanned such that the scan area was 12mm by 1mm, using the SKP for a period of 75 hours. Measurements were taken at a rate of 20 points per mm in both directions.

2.2.7.2 SKP Calibration

The SKP records the difference in localised potential between the tip and the sample, this gives us information about the magnitude of local differences in corrosion potential but it does not give absolute values for localised corrosion potential for comparison with other sets of data. In order to achieve this, the SKP needs to be calibrated.

The SKP had been previously calibrated in terms of electrode potential using Ag/Ag^+ , Cu/Cu^{2+} , Fe/Fe^{2+} and Zn/Zn^{2+} couples. Wells (8mm diameter, 1mm deep) were machined into discs (15mm diameter, 5mm thick) of the relevant metal. The wells were filled with a 0.5 mol dm^{-3} aqueous solution of the respective metal chloride salt (0.5 mol dm^{-3} nitrate salt in the case of Ag). The reference probe was positioned centrally, $120\mu\text{m}$ above calibration cell surface. Following equilibration, the Volta potential difference between the SKP reference probe and the polymer surface was measured. Metal electrode potential was simultaneously measured vs a Saturated Calomel Electrode (SCE) using a Solartron 1280 potentiostat. The process

was repeated with a 30 μm thick self-supporting film of PVB placed in contact with the electrolyte meniscus. In both cases, with and without the PVB film, there was a good linear relationship between the Volta potential difference obtained using the SKP reference probe, $\Delta\psi_{pol}^{Ref}$, and the free corrosion potential, E_{corr} , measured using the SCE with the potentiostat. The difference in $\Delta\psi_{pol}^{Ref}$ values as a result of the presence of the PVB film was found to be approximately constant at 0.22V. The value of the free corrosion potential can be calculated from the measured $\Delta\psi_{pol}^{Ref}$ value using the following equation:

Equation 2.1:

$$E_{corr} = \Delta\psi_{pol}^{Ref} + C$$

where C is a constant.

Calibration using the Cu/Cu^{2+} calibration cell (Figure 2.8) was repeated before and after each SKP experiment and C was found to have values of $0.26 \pm 0.06\text{V}$.

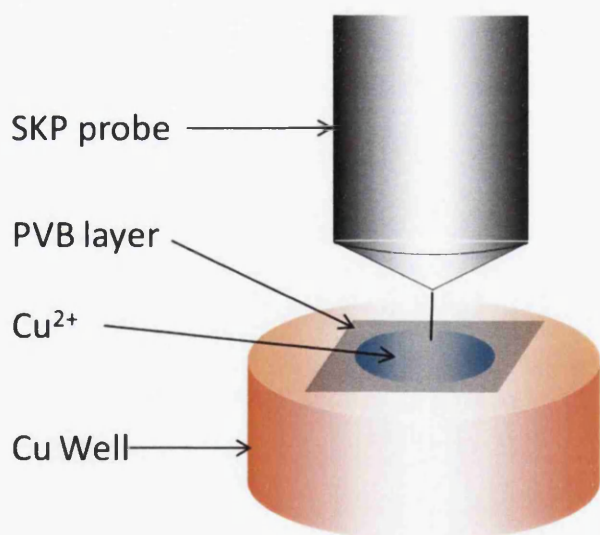


Figure 2.8 Calibration setup using the Cu/Cu^{2+} calibration cell.

2.2.8 Scanning Electron Microscopy

Where required for microscopy, the PVB was removed by immersion in ethanol for 5 minutes and the corrosion product was removed by immersion in a chromic-phosphoric acid solution at 60°C for 20 minutes. The samples were then rinsed in distilled water and allowed to dry. Micrographs were then taken using a Phillips XL30CP scanning electron microscope (SEM).

2.3 Results and Discussion

2.3.1 Optical Time-lapse Photography

Time-lapse photography was used to get an overview of the behaviour of FFC on a DSL-bearing AA6111 sample. A number of interesting filament behaviours were identified and are shown in **Figure 2.9**. The behaviours shown in these photographs are marked a - g and briefly described in **Table 2.2**. The heads of FFC filaments are known to consist of a droplet of electrolyte [32]. Feature (a) in **Figure 2.9** show this droplet. It can be seen that the large droplets accumulate soon after FFC initiation and then divide to produce multiple, smaller filament heads (b). These filament head droplets are visible even after extensive FFC has occurred (c). After 16:30hrs it is clear that the filament heads are travelling away from the defect and leaving a trail of white corrosion product behind them; this is the filament tail. Filaments tend to follow the rolling / grinding direction (e). Filaments occasionally split even after significant propagation has occurred (c) resulting in the tails creating a 'forked' shape.

The filament marked 'f' initially travels straight away from the defect parallel to the rolling / grinding direction (f(i)) but then turns sharply (f(ii)) and starts growing back towards the defect. The filament head is again following the rolling / grinding direction but is now travelling in the opposite direction. Filaments are known not to cross [116], the filament marked 'f' in **Figure 2.9** reaches a point where it would

need to change direction to avoid crossing its own tail (f(iii)). In f(iv) - f(vii) it can be seen that this filament avoids crossing, but then proceeds to follow, its original path (i.e. its own tail) closely. In the region marked 'd' from 23:30 hours to 26:30 hours, two filaments initially appear to be about to make contact but before this happens they each turn away from the other and continue on a new path.

The feature marked 'g' is a filament which initially grows away from the defect at an approximately constant rate but then stops after 77:30 hours (g(ii)). Approximately 1:30 hours after the filament stops the head is no longer visible and a light coloured region appears nearby (g(iii)). This light area then proceeds to spread out from the end of the filament (g(iv) - g(vi)). It is possible that the head electrolyte is dispersing in between the coating and the surface of the alloy.

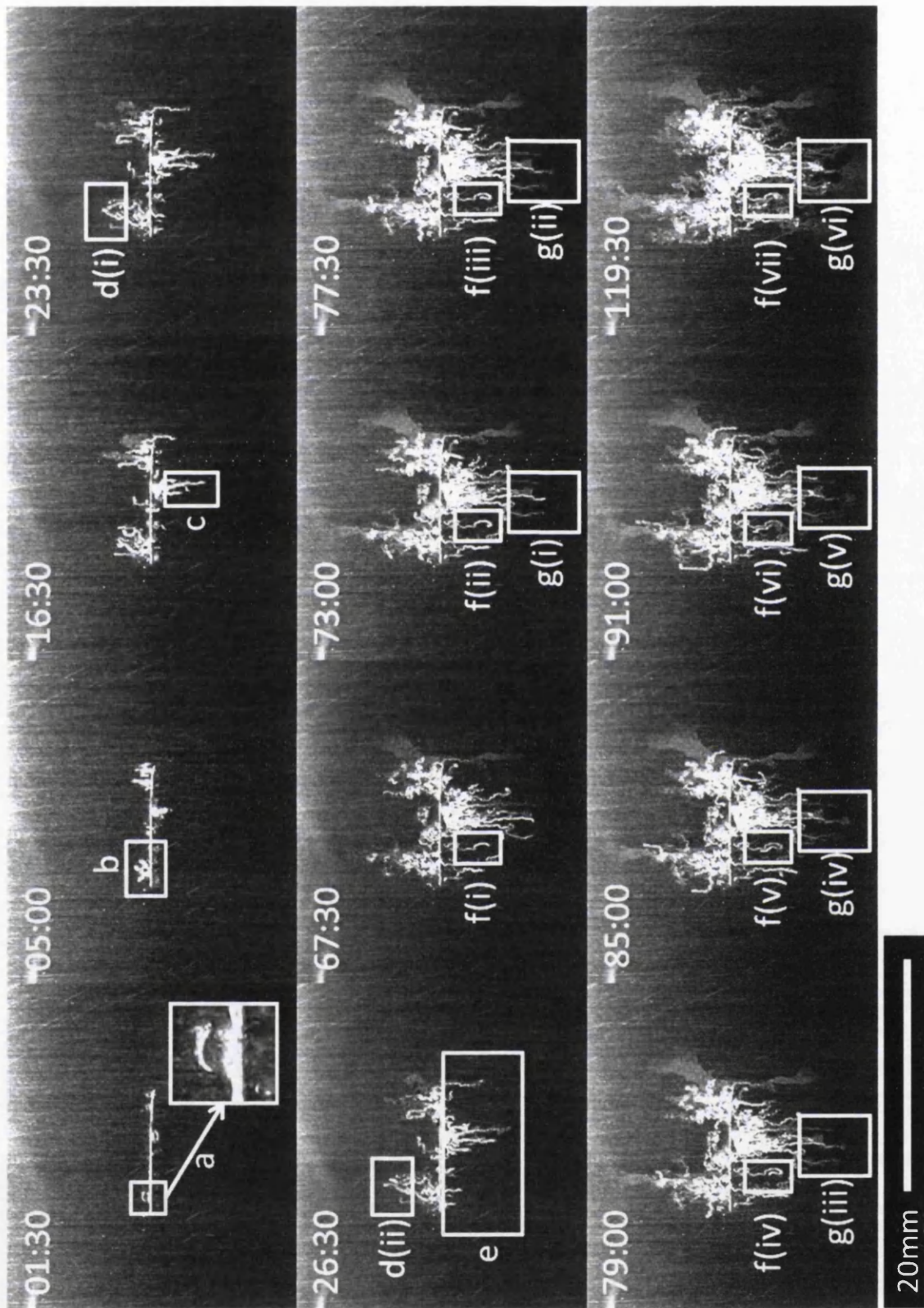


Figure 2.9 Time-lapse photographs of FFC on DSL-bearing AA6111. The time in hours and minutes since FFC initiation is shown at the top of each photograph.

Table 2.2 Summary of filament behaviours on DSL-bearing AA6111 during time-lapse experiment.

a	Electrolyte droplet next to the defect (enlarged version also shown).
b	A number of filaments branch out from the site of the droplet.
c	The main filament appears to 'fork'.
d	<p>(i) Two filaments appear to be about to meet.</p> <p>(ii) Just before, or on the point of, touching the filaments turn away from one another</p>
e	Filaments seem to have a tendency to follow the rolling / grinding direction - in straight lines.
f	<p>(i) An approximately straight filament moves away from the defect.</p> <p>(ii) The filament turns sharply.</p> <p>(iii) The filament starts to grow back towards the defect.</p> <p>(iv)- The filament continues to grow towards the defect, closely following, but not crossing the path of its original route.</p> <p>(vi)</p>
g	<p>(i) A filament grows away from the defect.</p> <p>(ii) The filament stops growing.</p> <p>(iii) A light area can be seen at the end of the filament.</p> <p>(iv)- The light area continues to grow away from the filament head and spreads out.</p> <p>(v)</p>

2.3.2 SKP Potentiometric Characterisation of Intact AA6111 Surfaces

Initially eight samples were produced using the methods described on page 76, these samples are listed in Table 2.1 along with a detailed description of their condition.

It is widely known that the presence of a DSL can lead to susceptibility to severe FFC but FFC also occurs to some degree in its absence, and so sets of both types were prepared for experimentation. These experiments were carried out in order to characterise the potentials of the intact surfaces of these samples. This allowed the effect of the surface condition and the heat treatment on the intact potential to be studied. The experiments were carried out over 75 hours to allow any time-dependent phenomena which might have occurred as a result of the warm and humid atmosphere to take place, and so that the influence of these effects on the values of $\Delta\psi_{pol}^{ref}$ could be recorded.

Values of $\Delta\psi_{pol}^{ref}$ measured by the SKP were used in conjunction with values of the constant C in Equation 2.1 to calculate values of the potential of the intact surfaces, this will be denoted ' E_{intact} '. Unique C values were obtained for each sample by implementing the calibration procedure described in the experimental procedure on page 87 before and after each experiment and then taking the mean of these two values. Values of E_{intact} are shown as a function of time (t) in Figure 2.10; time is measured from the moment that the samples are first placed into the humid and warm atmosphere in the SKP environment chamber. Each E_{intact} value plotted in this figure is calculated from the mean of 4800 $\Delta\psi_{pol}^{ref}$ measurements.

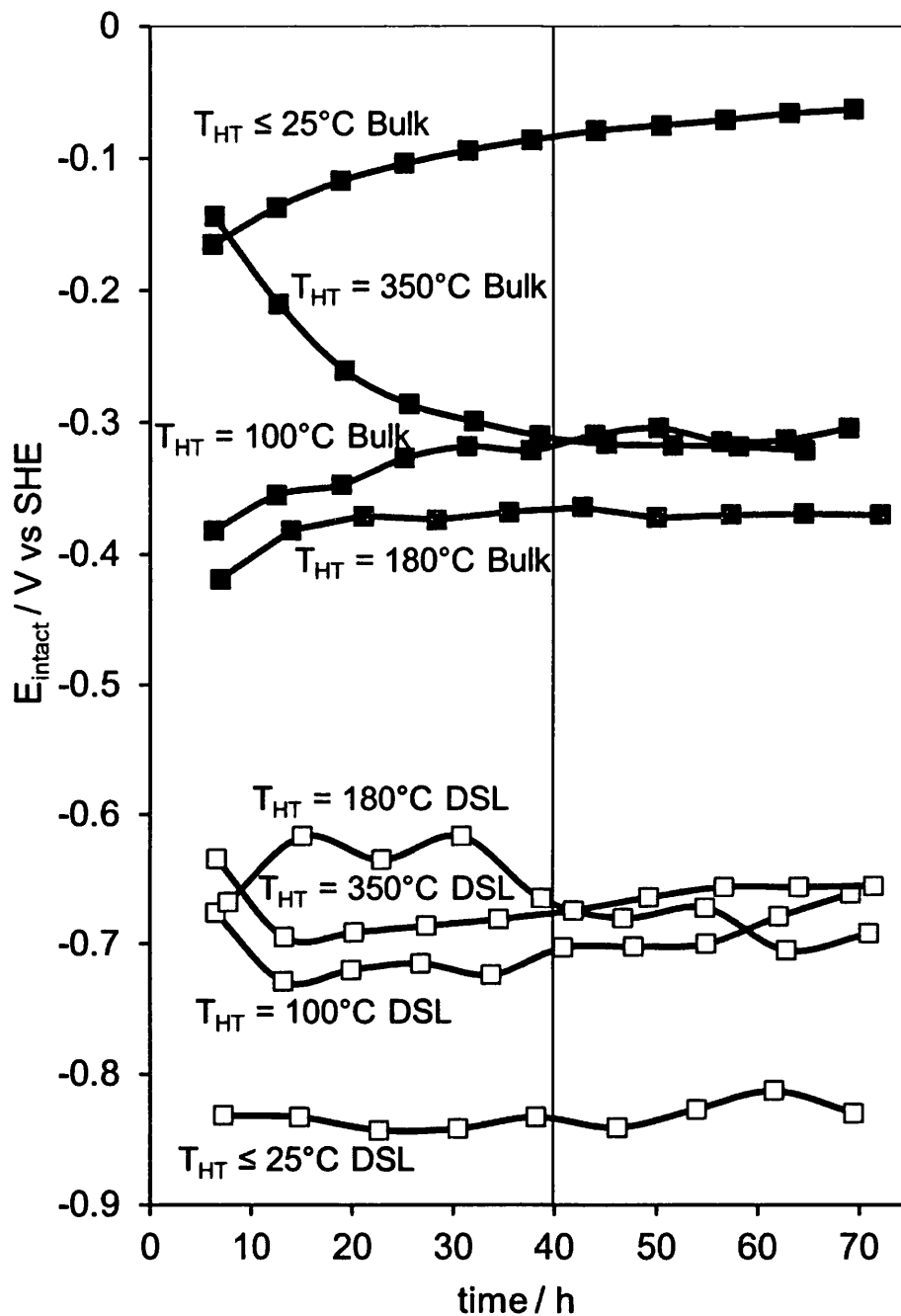


Figure 2.10 Time dependent E_{intact} for PVB coated AA6111 in air at 60% relative humidity and 40°C. Time (t) is the period elapsed since first contact with the humid SKP atmosphere. The upper family of curves (solid symbols) is obtained from samples where the DSL has been removed by caustic etching. The lower family of curves (hollow symbols) is obtained from samples bearing an abrasion-induced DSL. Post-abrasion heat treatments have been applied at a range of temperatures (T_{HT}) as indicated.

The upper family of curves, with solid marker symbols, is made up of E_{intact} data taken from bulk samples and the lower family, with hollow marker symbols, is made up of E_{intact} data from DSL bearing samples. There is significant variation in the values of E_{intact} for many of the samples in the first 40 hours. This variation decreases after 40 hours as the samples reach a steady state with the humid SKP chamber atmosphere.

Mean E_{intact} values over the stable period between 40 and 75 hours were calculated for each of the samples and these time-independent values are plotted as a function of T_{HT} in Figure 2.11. For convenience AA6111 in the as-received, T4 temper, is allocated the heat treatment temperature of 25°C (room temperature), i.e. $T_{HT} = 25^{\circ}\text{C}$. The upper curve with solid square marker symbols in Figure 2.11 is made up of time-independent E_{intact} data for bulk AA6111 samples and the lower curve (with hollow square marker symbols) is made up of E_{intact} data for DSL samples.

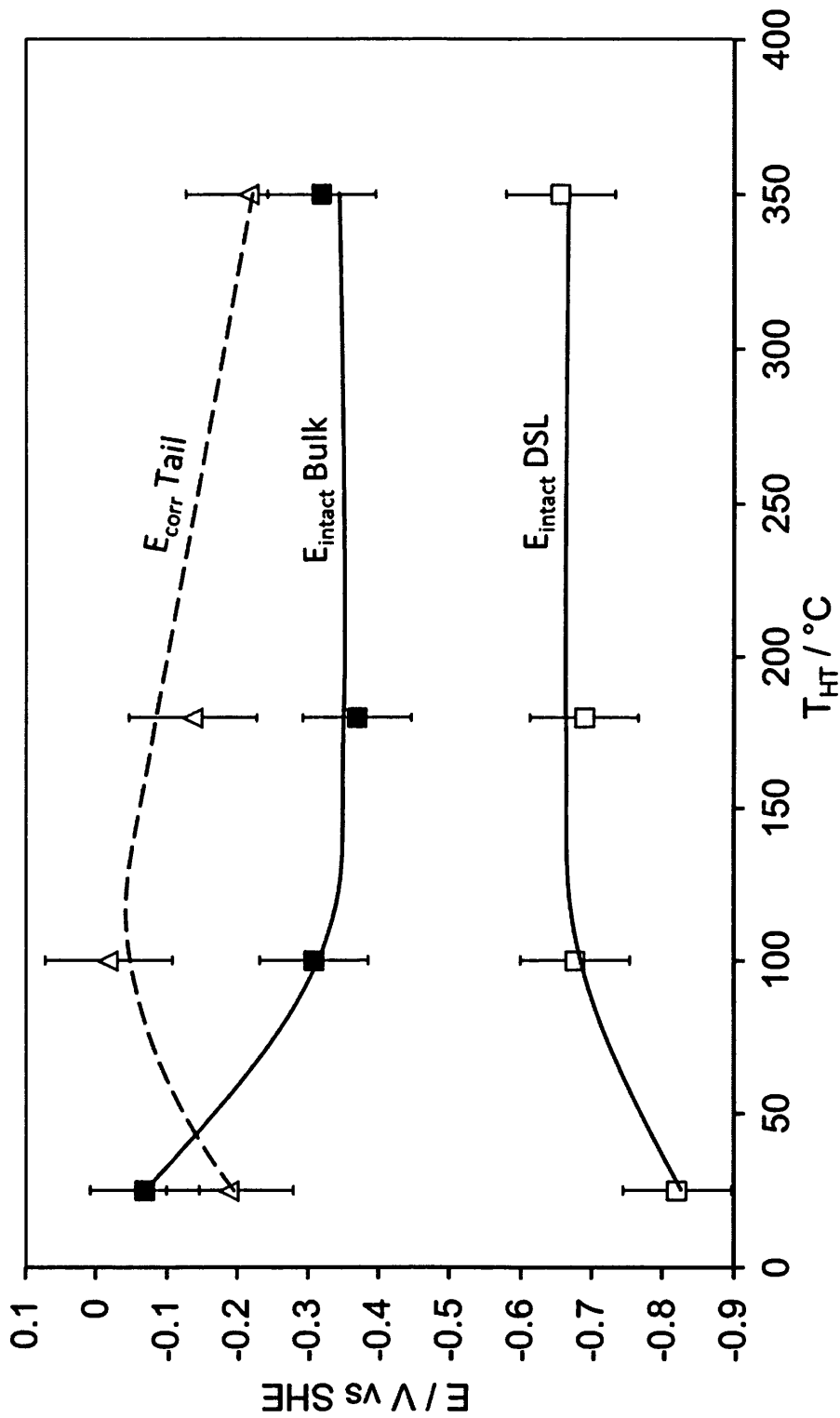


Figure 2.11 Time-independent potentials (E_{intact}) for PVB coated AA6111 plotted as a function of heat treatment temperature (T_{HT}). All time-independent values are calculated as the mean potential over the time period of 40-75 hours since first contact with the humid SKP atmosphere.

For each of the heat treatment conditions tested, the E_{intact} value is significantly lower for the DSL samples than for the bulk samples. This E_{intact} difference is greatest for the T4 sample at 0.75V but is much smaller and approximately constant for the heat treated samples. The difference is 0.37V for the $T_{HT} = 100$ samples, 0.32V for the $T_{HT} = 180$ samples and 0.34V for the $T_{HT} = 350$ samples. Hence, a decreased potential has been shown to occur as a result of the presence of a DSL irrespective of whether or not a subsequent heat treatment has been carried out.

It has been shown that during alkaline etching of the surface of aluminium alloys which contain significant levels of copper in solid solution, the surface can become enriched in copper [117]. In the case of an alloy containing 0.95at.% copper alkaline etching can produce a 2nm thick copper enriched layer directly beneath the oxide film. The open-circuit potential (OCP) of an alkaline-etched sample of this alloy was measured and compared to the OCP of a sample which had not been alkaline etched. It was found that etching caused an increase of 0.41V and this was attributed to the presence of the copper enriched layer [117]. This finding might explain the exceptionally high E_{intact} value for the B25 sample as shown in Figure 2.10 and Figure 2.11 and without this copper enrichment effect the E_{intact} difference between the B25 and the D25 sample would have been much more in line with that of the heat treated samples. The E_{intact} value recorded for B25 cannot be taken to be representative of that for an AA6111-T4 surface in the absence of a DSL where no caustic etching has been carried out. The copper enrichment effect is likely to have been reduced or eliminated in the other bulk samples B100, B180 and B350 because the copper would have probably diffused from the enriched layer to form copper rich particles during heat treatment.

Despite the above complication, it is clear that the introduction of a DSL to these AA6111 samples by abrasion results in a surface with a decreased E_{intact} . This effect is further supported by the results shown in Figure 2.12 where the sample has been prepared by etching away the DSL from only half the sample. The difference in potential between the DSL and the bulk is approximately 0.22V vs SHE which falls within the error limits for the THT=180°C sample in Figure 2.11.

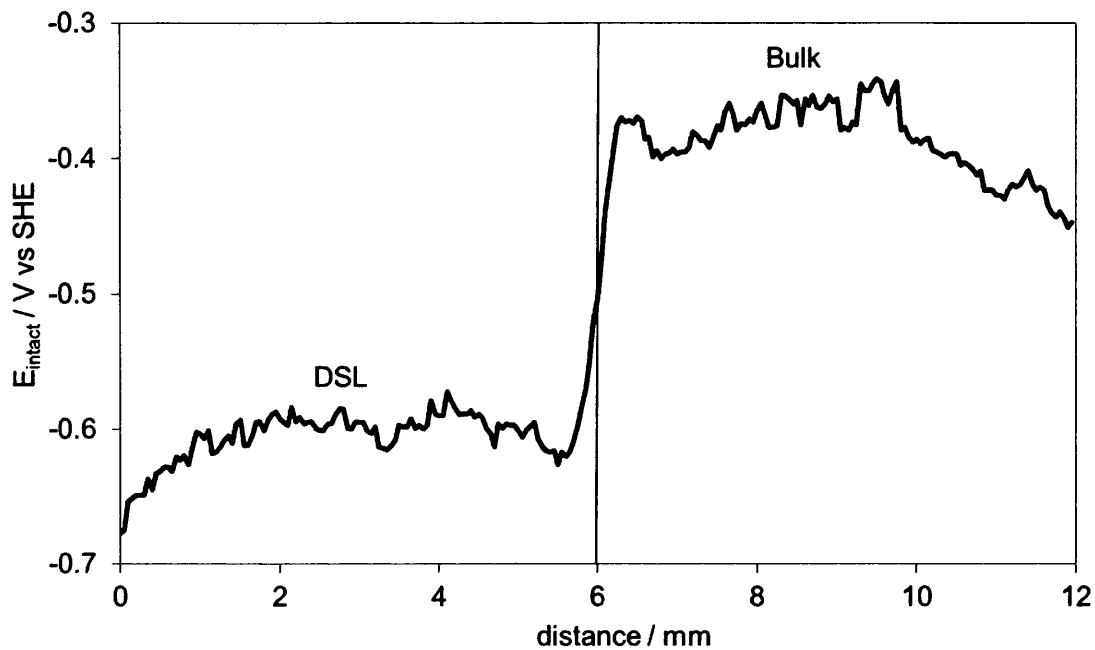


Figure 2.12 E_{intact} plotted across a half-etched and heat treated sample of AA6111 ($T_{HT}=180^{\circ}\text{C}$) which has been PVB coated. The sample was abraded to introduce a DSL and then half-etched to remove the DSL in the region indicated between 6mm and 12mm.

Another set of samples were prepared by etching in sodium hydroxide and desmutting in nitric acid (as for the main set of AA6111 samples) and then abrading half of the sample with SiC paper. The purpose of these experiments was to test whether or not the potential difference between the DSL and the bulk would occur on the purer aluminium alloy AA1050 and high purity aluminium samples.

Figure 2.13 shows three SKP maps which display E_{intact} on samples of AA6111, AA1050 and 99.999% pure aluminium which have been prepared using the etching and half abrading method described above. None of these samples have been heat treated. In each case the left 5mm has been abraded and has a decreased E_{intact} compared to the side which has been etched but not abraded.

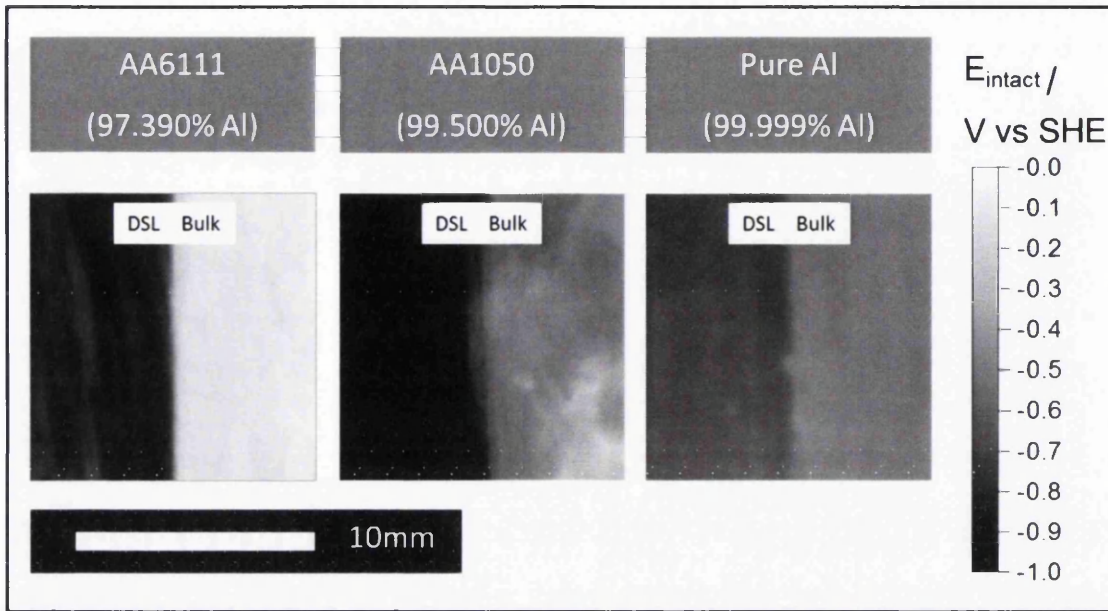


Figure 2.13 E_{intact} SKP maps for etched and half abraded AA6111, AA1050 and 99.999% pure aluminium.

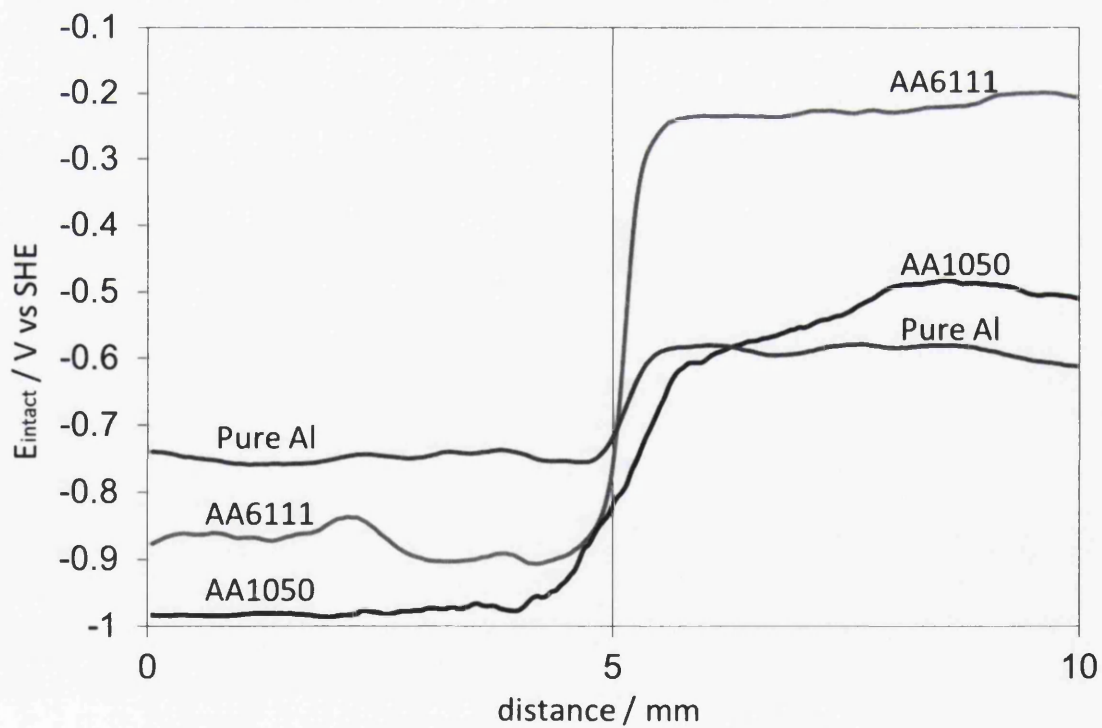


Figure 2.14 E_{intact} profiles for etched and half abraded AA6111, AA1050 and 99.999% pure aluminium.

Figure 2.14 shows values for E_{intact} taken from the samples in Figure 2.13. Each E_{intact} value plotted is the mean of the 240 readings taken across the sample parallel to the line which divides the bulk from the DSL. Mean E_{intact} values on the DSL half of each sample are relatively similar and in each case the DSL is anodically activated relative to the bulk. There is a much larger difference in the E_{intact} values of the bulk halves of the samples. The largest difference between the DSL and bulk E_{intact} values is for the least pure AA6111 sample and the smallest difference is for the 99.999% pure aluminium sample. Previous research suggests that discrete Q phase grain boundary precipitates are not present in the deformed layer of AA6111 that has not been heat treated above 25°C [74], consequently we must look for another explanation for the lower potential of the DSL bearing half of the deformed AA6111 sample shown here. This result is similar to that shown in Figure 2.11 where the enrichment of copper at the surface as a result of the etching process was identified as a possible explanation.

The difference in E_{intact} for the DSL bearing and bulk halves of the much purer AA1050 alloy and the 99.999% pure aluminium cannot be wholly explained by copper enrichment. The fact that the DSL is anodically activated even for the pure aluminium sample cannot be explained by any mechanism involving the segregation of solute atoms or room temperature natural ageing unless segregates or precipitates composed of the 10 parts per million of impurity elements has this significant effect on E_{intact} . It is more likely that aspects of the physical nature of the DSL such as the high number density, high strain energy and high misorientation of grain boundaries there creates this effect in the pure sample and contributes to this effect on the others.

The reduction in bulk potential with increasing purity is likely to be due to a cathodic deactivation as result of the decrease in the amount of cathodic intermetallics.

The difference in potential of the DSL compared to the bulk is usually explained as being the result of enhanced precipitation during heat treatment. The high purity sample develops a potential difference as a result of the introduction of a DSL

without heat treatment and with only a minimal fraction of impurity solute atoms. The small difference in potential on this sample in particular requires more explanation.

The differences in E_{intact} between bulk and DSL AA6111 samples in Figure 2.10 and Figure 2.11 can be understood on the basis of mixed potential theory. Similar results have been reported for the similarly composed, but lower copper alloy AA6016 [101]. The decreased potential of the DSL must result from it being either anodically activated or cathodically de-activated relative to the bulk. It is now generally accepted that the presence of a DSL makes the surface of aluminium more susceptible to corrosion processes such as FFC i.e that surface is made more reactive. It is therefore reasonable to argue that anodic activation is the major cause of the potential depression associated with the presence of a DSL on aluminium. Polarisation experiments may help to confirm whether anodic activation or cathodic deactivation is the dominant mechanism.

2.3.3 Potentiodynamic Polarisation Experiments

In a previous study [101] a series of polarisation experiments in dilute (0.5%), near neutral (pH6 to pH6.5) aqueous sodium chloride were carried out on AA6016. These experiments showed that the decreased potential of the DSL was primarily a result of anodic activation. A similar set of polarisation experiments was carried out in the present study on AA6111 using the same experimental techniques and electrolytes. **Figure 2.15** is a set of polarisation curves for DSL-bearing AA6111 in the de-aerated electrolyte and **Figure 2.16** is a similar set for bulk samples. **Figure 2.17** is a set of polarisation curves for DSL-bearing AA6111 in the aerated electrolyte and **Figure 2.18** shows a similar set for bulk samples. Samples were tested in the T4 condition, with $T_{HT} = 180$ and with $T_{HT} = 350$. All of the polarisation results displayed in these figures are averaged from a number of experiments.

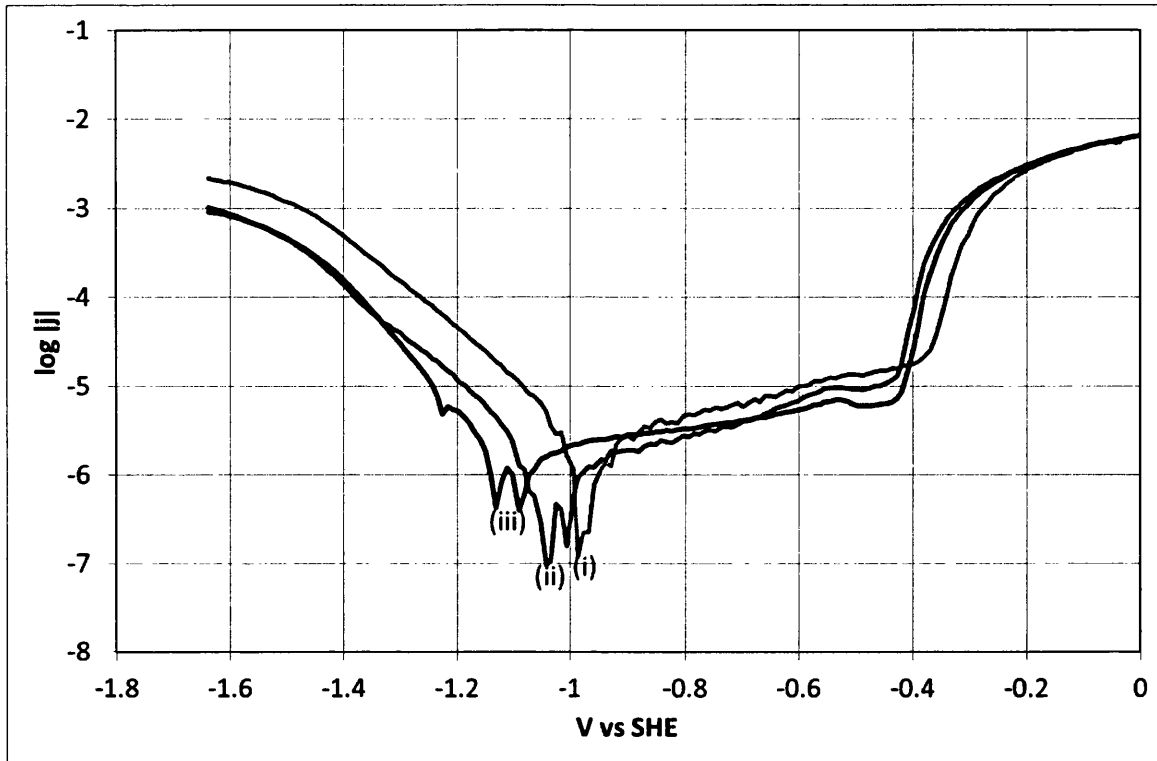


Figure 2.15 Potentiodynamic polarisation curve for a DSL-bearing AA6111 sample in de-aerated 0.5% w/v aqueous NaCl at pH6.5. THT = (i) 25°C, (ii) 180°C, (iii) 350°C.

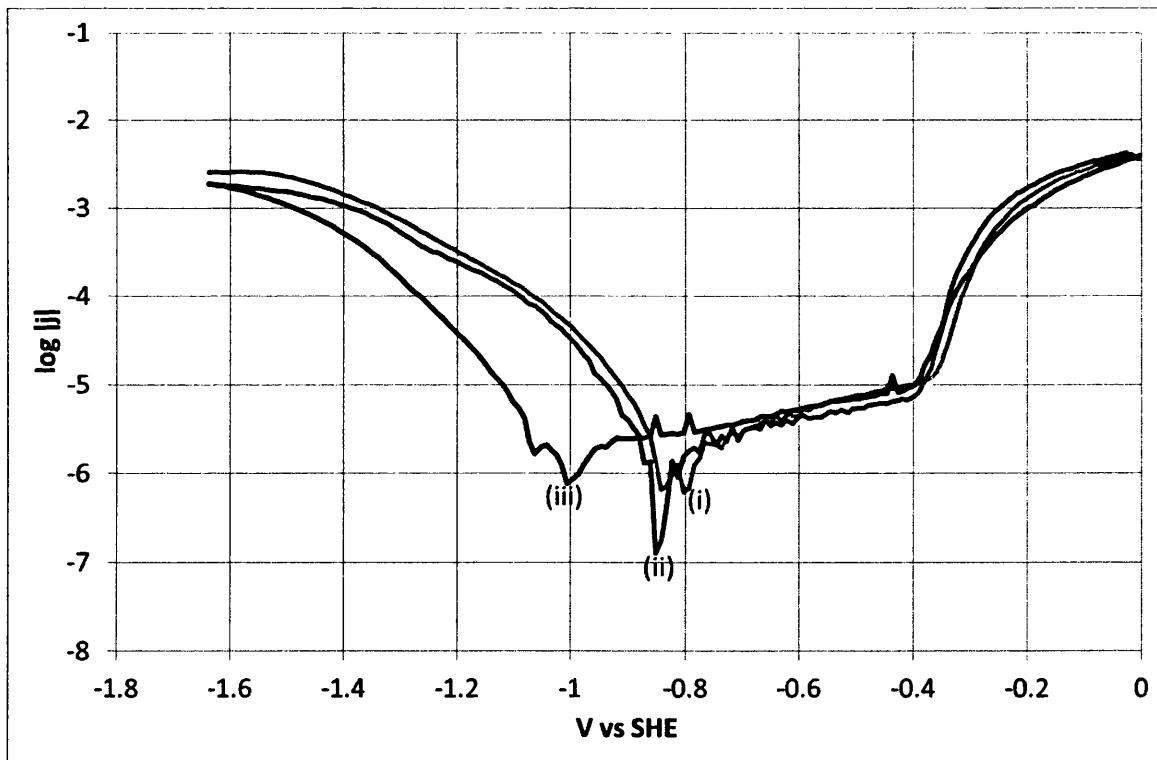


Figure 2.16 Potentiodynamic polarisation curve for a bulk AA6111 sample in de-aerated 0.5% w/v aqueous NaCl at pH6.5. THT = (i) 25°C, (ii) 180°C, (iii) 350°C.

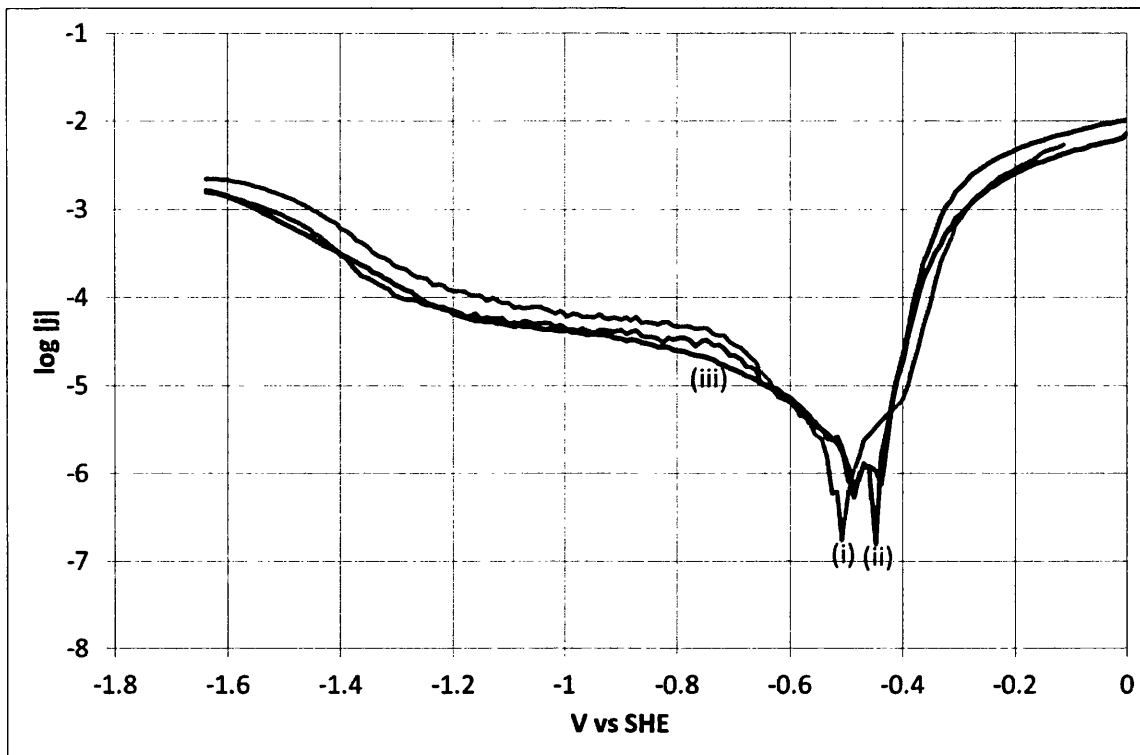


Figure 2.17 Potentiodynamic polarisation curve for a DSL-bearing AA6111 sample in aerated 0.5% w/v aqueous NaCl at pH6.5. $T_{HT} =$ (i) 25°C, (ii) 180°C, (iii) 350°C.

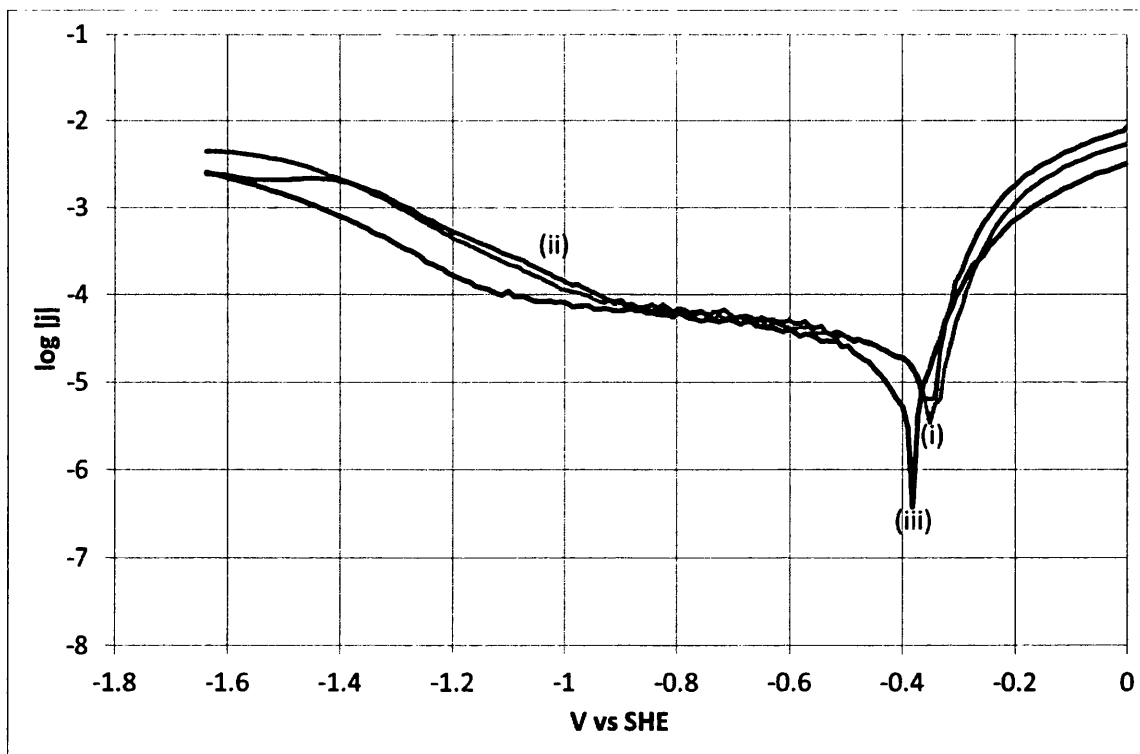


Figure 2.18 Potentiodynamic polarisation curve for a bulk AA6111 sample in aerated 0.5% w/v aqueous NaCl at pH6.5. $T_{HT} =$ (i) 25°C, (ii) 180°C, (iii) 350°C.

Average values of cathodic current density were calculated for both DSL bearing and bulk samples in the range -0.74 V vs SHE to -0.92 V vs SHE on *Figure 2.17* and *Figure 2.18*. These were plotted as a function of T_{HT} in *Figure 2.19*.

From previous work [74] it might be expected that heat treatment would result in precipitation of cathodically active Q phase and that this precipitation would be enhanced in the DSL. In this study the values of J_{ca} for neither bulk nor DSL bearing samples show any significant increase with heat treatment temperature and in fact the values of J_{ca} in the DSL decrease more rapidly than the bulk. However the growth of an oxide layer at higher heat treatment temperatures may have restricted cathodic electron transfer and this could explain the decrease in J_{ca} values shown in *Figure 2.19*.

The polarisation curves in *Figure 2.15* and *Figure 2.16* show passivity with passive current densities in the range 10^{-6} to 10^{-5} . Average values of anodic current density for both DSL and bulk samples in the range -0.46 V vs SHE to -0.77 V vs SHE were also calculated. These are plotted against THT in *Figure 2.19*.

For heat treatment temperatures below 350°C *Figure 2.19* shows anodic activation of the DSL compared to the bulk. The upper two curves in this figure show cathodic deactivation of the DSL relative to the bulk which increases with higher temperature heat treatments. The presence of anodic beta precipitates would be expected to cause an increase in J_{an} . In AA6111 precipitates of β'' would be expected to form in a normal grain-sized material when artificially aged, these would not necessarily develop in the DSL because Q phase is thought to preferentially precipitate at grain boundaries there [74]. The results presented in *Figure 2.19* for the bulk show no significant increase in J_{an} with increased T_{HT} . J_{an} for the DSL decreases.

E_b values were taken from the anodic polarisation curves in *Figure 2.15* and *Figure 2.16* and are plotted against THT in *Figure 2.20*. For AA6111 in the T4 condition E_b is approximately 0.010V lower when the DSL is present. At heat treatment temperatures above this the difference is much greater and reaches a maximum of approximately 0.045V at the 'paint bake' temperature of 180°C. *Figure 2.20*

supports the theory that the DSL is anodically activated compared to the bulk; in this case the degree of activation appears to reach a maximum at 180°C.

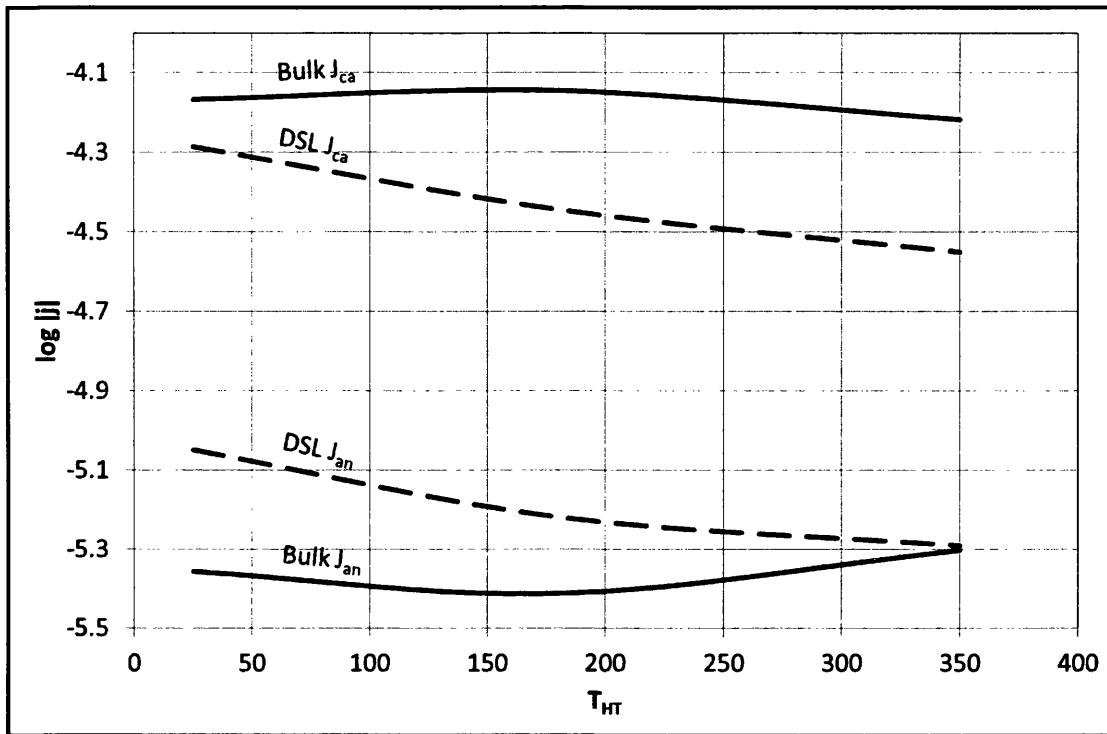


Figure 2.19 Cathodic (j_{ca}) and anodic (j_{an}) current densities plotted as a function of THT for DSL-bearing and bulk AA6111 samples with THT=25, THT=100 THT=180 and THT=350

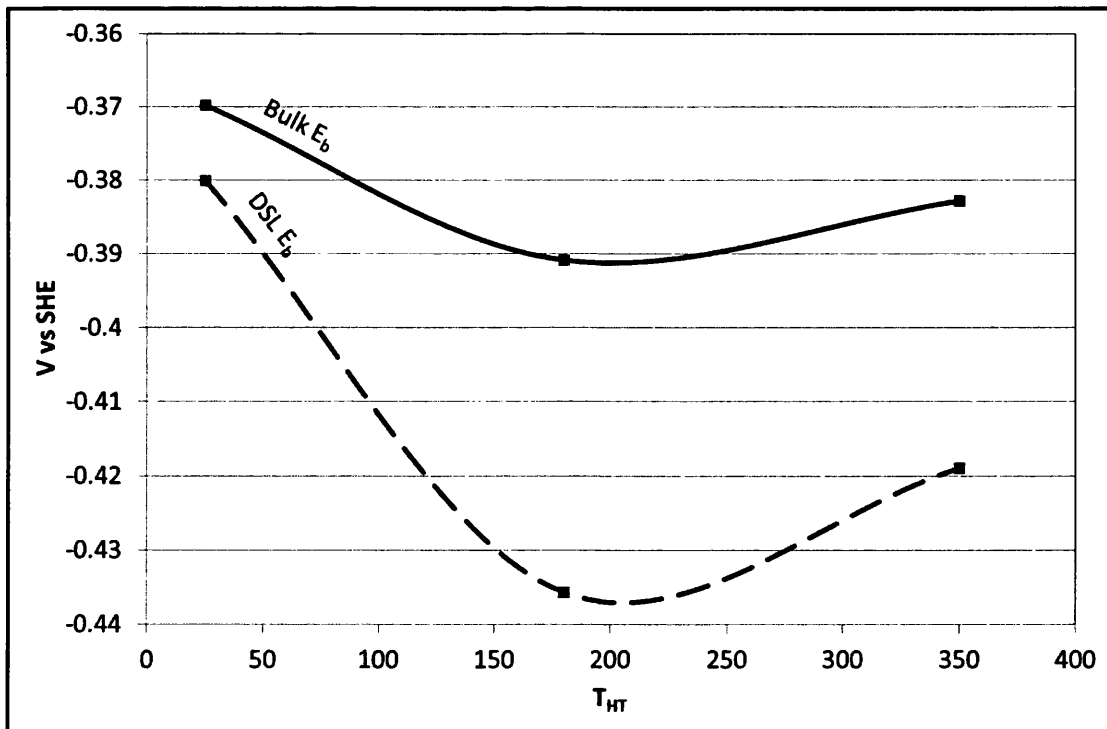


Figure 2.20 Anodic breakdown potentials (E_b) for DSL-bearing and bulk AA6111 samples with THT=25, THT=100 THT=180 and THT=350

2.3.4 SKP Potentiometry of FFC on DSL Bearing AA6111

After initiation, a rapid and superficial attack occurred on the DSL-bearing samples of AA6111 both in the solutionised and naturally aged T4 temper and after heat treatment at 100°C, 180°C and 350°C. This attack is consistent with that which has been termed 'surface active' FFC [101]. As such the metal dissolution was restricted to the depth of the abrasion-induced DSL [74]. All of the DSL-bearing samples tested also exhibited secondary filaments of the slower and more deeply penetrating 'successive pitting' form of FFC [76, 101].

The matrix of $\Delta\psi_{Pol}^{Ref}$ values which were obtained during each of the SKP scans was used in conjunction with Equation 2.1: to calculate the distribution of E_{corr} values at the AA6111 surface. SKP data obtained at different times (t) after initiation was used to visualise the dynamic evolution of E_{corr} associated with FFC propagation for samples in each temper ($T_{HT}=25^{\circ}\text{C}$, $T_{HT}=100^{\circ}\text{C}$, $T_{HT}=180^{\circ}\text{C}$ and $T_{HT}=350^{\circ}\text{C}$). E_{corr} maps measured at three times (a: t=7h, b: t=35h, c: final scan) for each temper are shown in Figure 2.21. Scanning was stopped when the FFC filaments were seen to have encroached approximately 4mm into the scan area. The final scan in each case coincides with the area within the white square marked on the photograph in Figure 2.22.

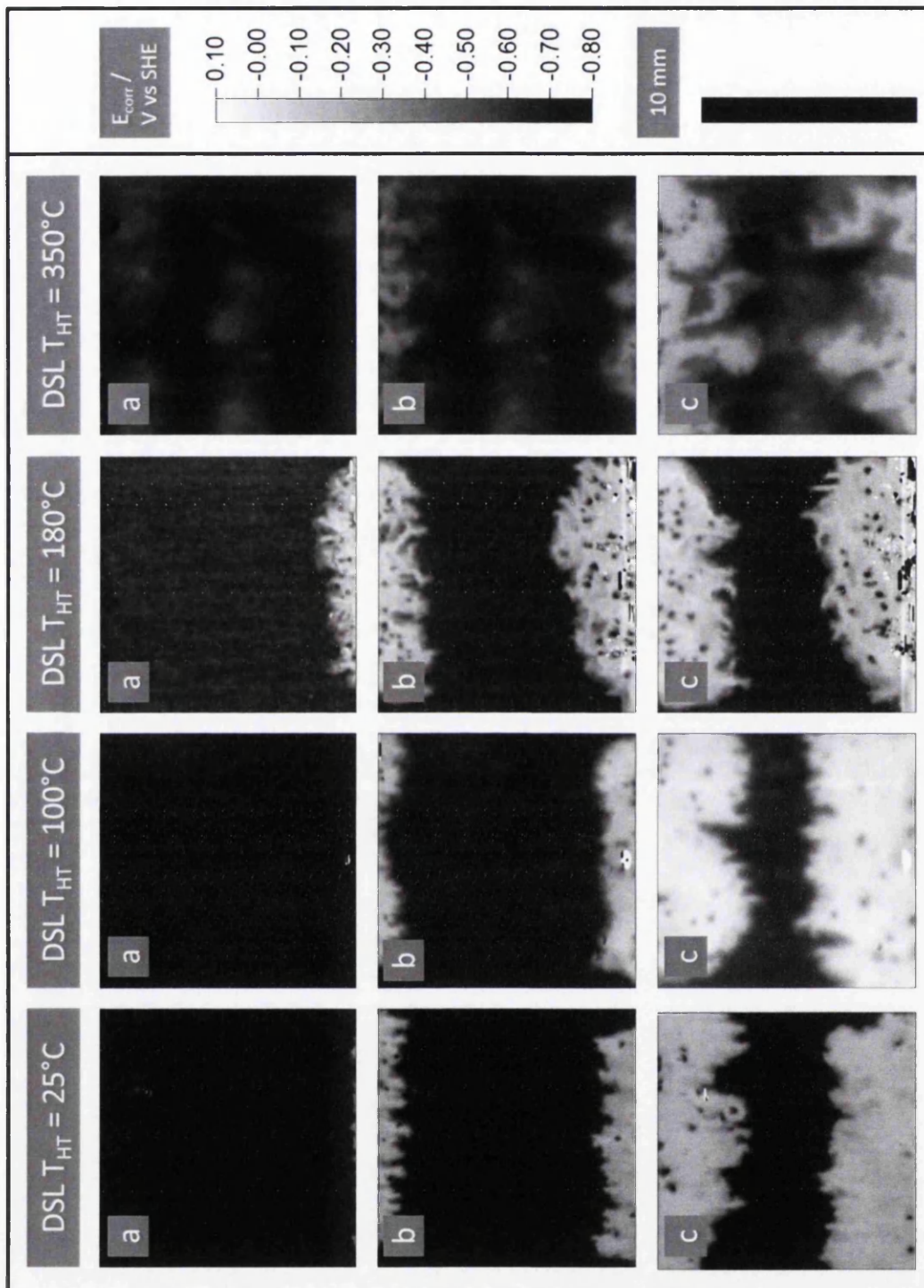


Figure 2.21 Interpolated grey scale maps showing the E_{corr} distribution measured over PVB coated, DSL-bearing AA6111 ($T_{HT}=25^{\circ}\text{C}$, 100°C , 180°C and 350°C) in air at 60% RH and 40°C . Key: (a) t = approx. 7h following FFC initiation, (b) t = approx. 35h, following FFC initiation (c) the final scan of the sample.

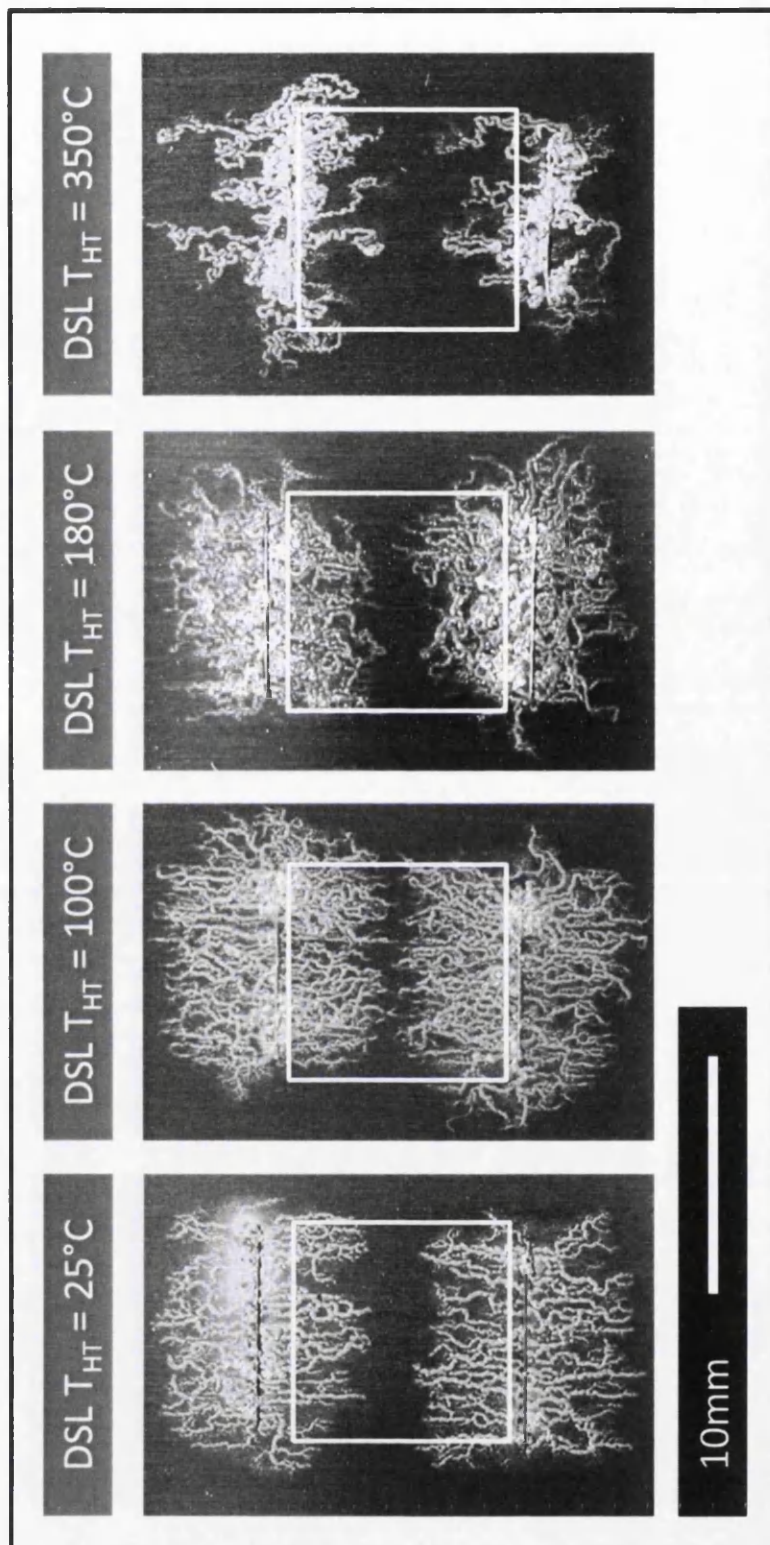


Figure 2.22 Photographs showing PVB coated, DSL-bearing AA6111 ($T_{HT}=25^{\circ}\text{C}$, 100°C , 180°C and 350°C) after FFC initiation and corrosion in air at 60% RH and 40°C . The SKP-scanned area is indicated on each photograph.

Figure 2.21 shows that the SKP is not able to resolve the individual FFC filaments. The surface-active FFC fronts propagate away from the coating defects and leave in their wake a region of increased potential (E_{corr} = approximately -0.3 V vs SHE) associated with the filament tails. The FFC front is made up of a line of filament heads which were not distinguishable from the tails on these E_{corr} maps. In a recent study of FFC on AA6016 [101] filiform heads could be partially resolved as a band of lower potential (approximately -0.8V vs SHE). It is likely that the difference between the potential of the heads and that of the adjoining regions on the AA6111 samples used here was not sufficiently large for them to be resolved.

The time dependence of the potentials associated with the advancing FFC filament head is illustrated in Figure 2.23 in which the potential measured along the axis of filament propagation is plotted for DSL-bearing AA6111 in the T4 condition at times between 7h and 54 hours since FFC initiation. Again the head region is not clearly distinguished; the profiles do not show any clear difference in potential where the FFC filament heads are located. The surface active FFC front appears to move at an approximately constant rate away from the defect.

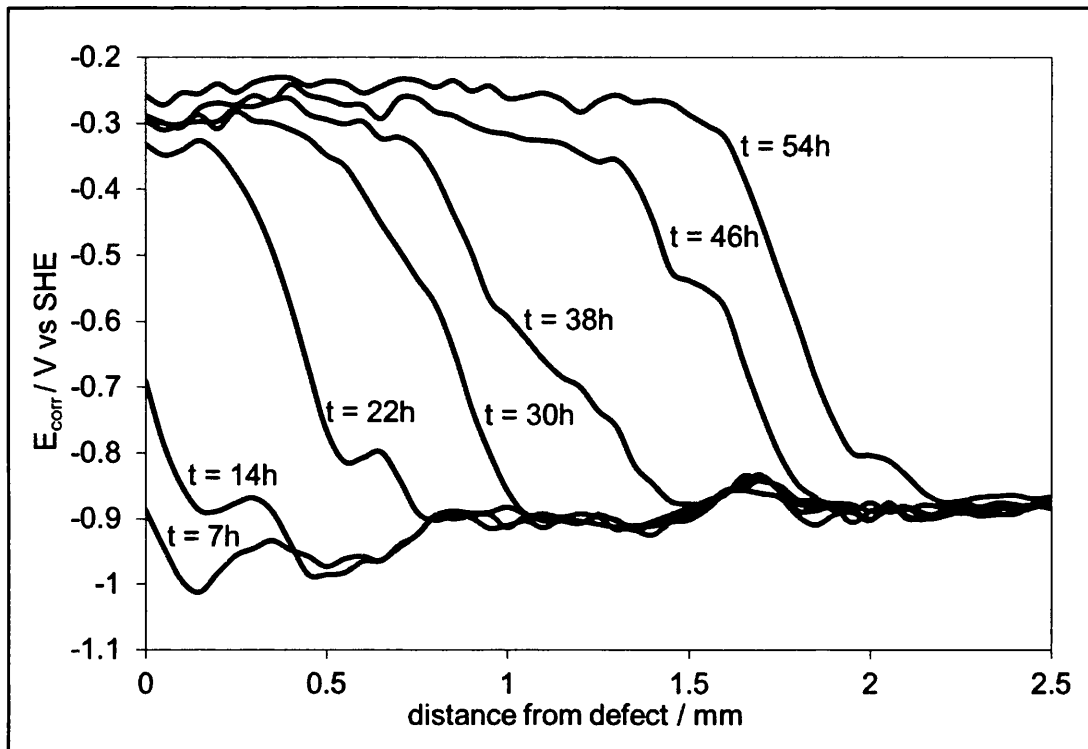


Figure 2.23 Profiles of E_{corr} as a function of distance from the defect plotted for surface-active FFC on PVB-coated, DSL-bearing AA6111-T4 ($T_{HT}=25^{\circ}\text{C}$). Each profile is labelled with the time (t) in hours since FFC initiation.

The photographs in Figure 2.22 show a whitish corrosion product which covers the partially coalesced filaments (of diameter 0.1mm to 0.2mm) in the regions which are seen to have increased potential on their respective potential maps (Figure 2.21). The FFC filament heads therefore co-locate with the front which is seen to move across the samples in Figure 2.21.

Figure 2.24 (a) shows an SEM micrograph obtained from the DSL-bearing sample ($T_{HT}=180^{\circ}\text{C}$) in the region of the surface-active FFC front. It can be seen that the corroded region (right) has a very fine porous structure which is consistent with intergranular corrosion of the sub-micrometer grains of the DSL. The scratch lines resulting from the abrasion of the sample can be seen on the uncorroded region of this micrograph (left). The depth of surface active FFC attack was estimated to be $>2\mu\text{m}$ by tilting this sample under the SEM. Figure 2.24 (b) shows a region of the same sample near the defect where secondary successive pitting FFC had also occurred. Here much deeper intergranular corrosion has taken place and this

micrograph shows the much larger bulk grains (diameter approximately $25\mu\text{m}$) which have been exposed. The depth of this attack appeared to be in the range $10\mu\text{m}$ to $50\mu\text{m}$. Similarly corroded surfaces were observed for successive pitting filiform heads on all AA6111 samples.

As described previously, the SKP potential maps in Figure 2.21 show that a front made up of surface-active FFC filament heads moves out from the defect and across the sample leaving behind it a region containing the filament tails which has an increased potential. Within this region another phenomenon is detected by the SKP; small circular regions of low potential which are approximately 0.2mm in diameter develop near the defect. Where $T_{\text{HT}}=25^\circ\text{C}$ and where $T_{\text{HT}}=100^\circ\text{C}$ there are relatively few of these low E_{corr} 'discs' and they are located well away from the surface active FFC front. When the sample has been heat treated at $T_{\text{HT}}=180^\circ\text{C}$ there are many more low E_{corr} discs and they propagate more widely over the high E_{corr} region which is in the wake of the surface active FFC front. These discs are thought to occur as a result of secondary FFC attack of the AA6111 substrate by successive pitting FFC where the DSL has already been substantially dissolved by surface active FFC.

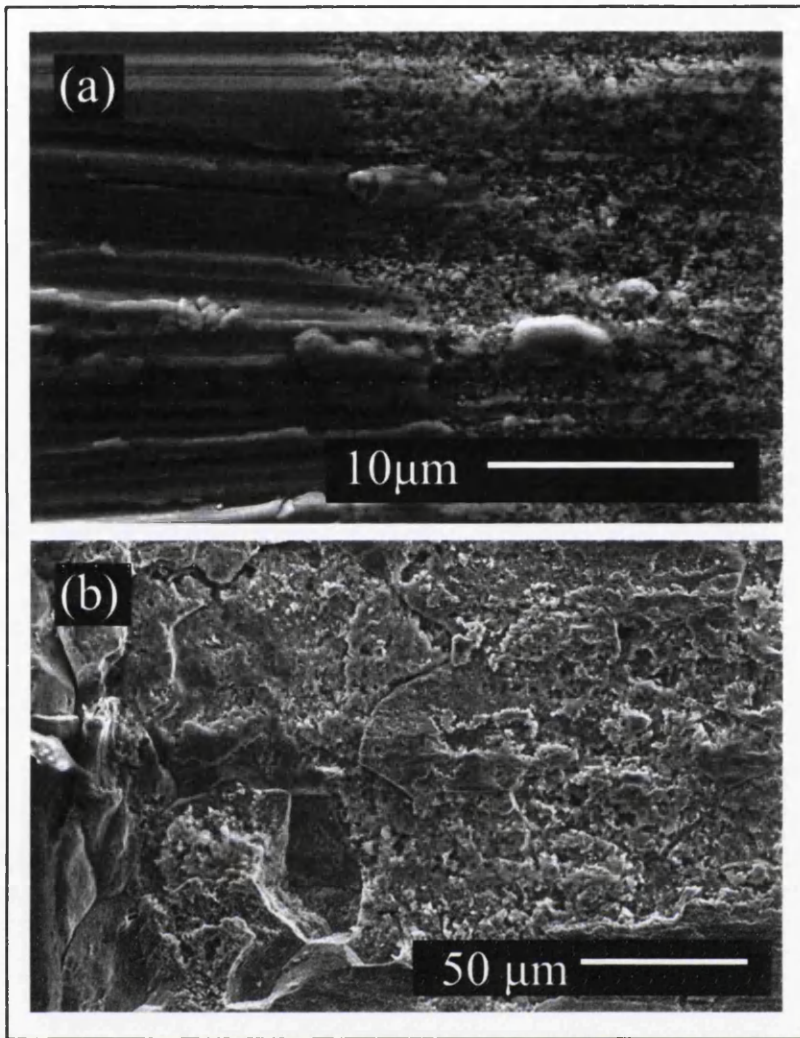


Figure 2.24 SEM images of corroded DSL-bearing AA6111 ($T_{HT}=180^{\circ}\text{C}$) surface after ethanol stripping of the PVB coated and the removal of corrosion products with chromate-inhibited phosphoric acid. (a) The surface-active FFC front. (b) A region near the coating defect where successive-pitting FFC has also occurred.

2.3.5 SKP Potentiometry of FFC on Bulk AA6111

Figure 2.21 shows successive pitting FFC propagating in regions of the sample where the DSL has been substantially removed by preceding surface active FFC. This finding shows that successive pitting FFC can occur without the presence of a DSL but does depend upon the temper of the bulk. The bulk samples were used to further investigate successive pitting FFC.

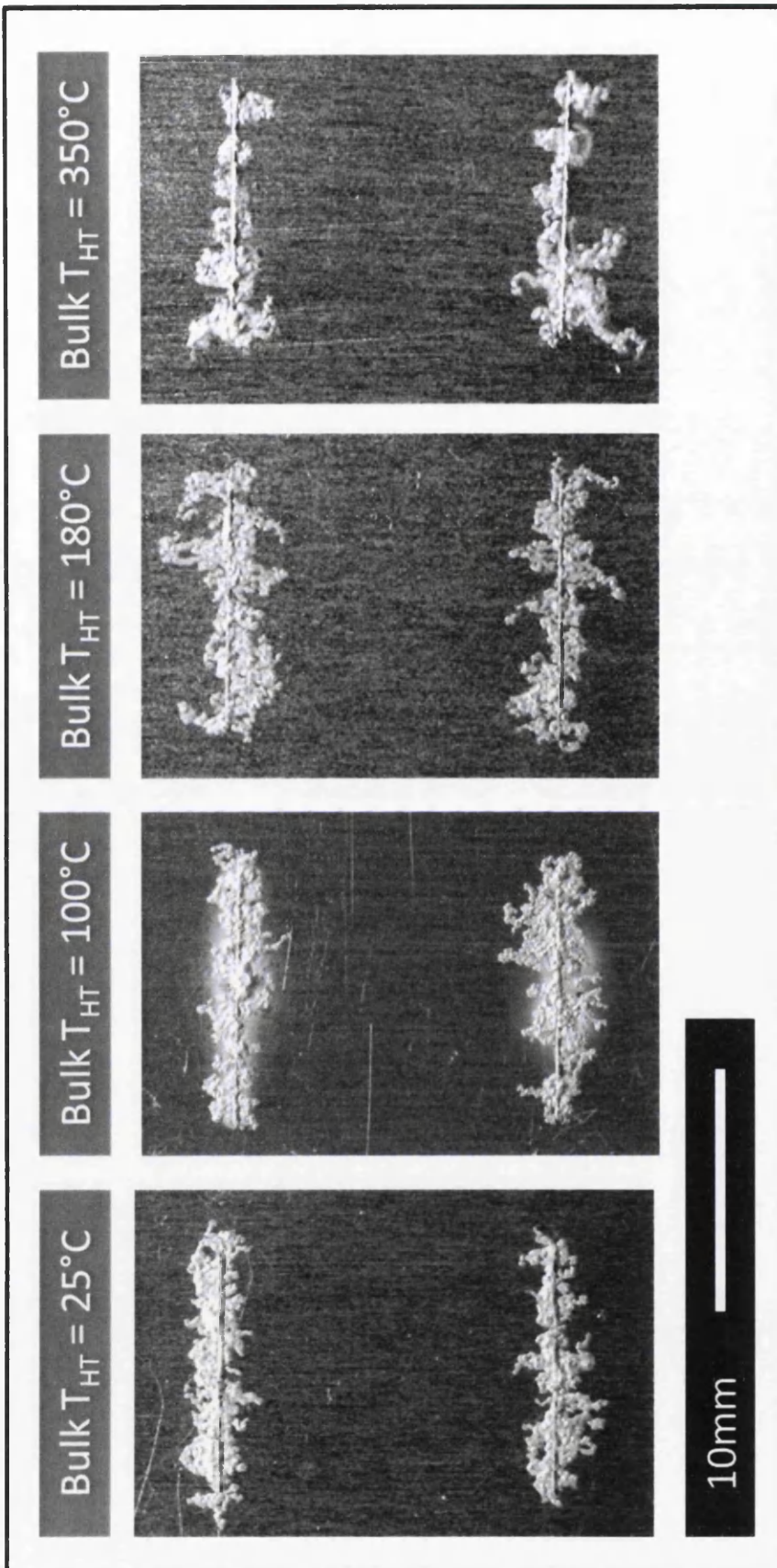


Figure 2.25 Photographs showing PVB coated, bulk AA6111 ($T_{HT}=25^{\circ}\text{C}$, 100°C , 180°C and 350°C) after FFC initiation and corrosion in air at 60% RH and 40°C .

As can be seen in Figure 2.25 AA6111, bulk samples in all four heat treatment conditions show corrosion with an appearance that is consistent with the successive pitting form of FFC. The E_{corr} distribution associated the successive pitting FFC on these samples is shown in **Figure 2.26**. As was the case behind the surface active FFC front on DSL bearing samples (Figure 2.21), the filament heads can be resolved as small dark regions indicating low E_{corr} . For these bulk samples a front of surface active FFC did not precede the successive pitting as occurred for DSL bearing samples. In the SKP maps of bulk samples (**Figure 2.26**) the tails can be resolved as light tracks. These were not apparent behind the surface active FFC front in the DSL bearing samples; this is likely to be because the 'background' potential is increased by the presence of the corrosion product left behind by the surface active FFC.

It is clear from the above evidence that neither a pre-existing DSL nor preceding surface active FFC is necessary for successive pitting FFC to occur.

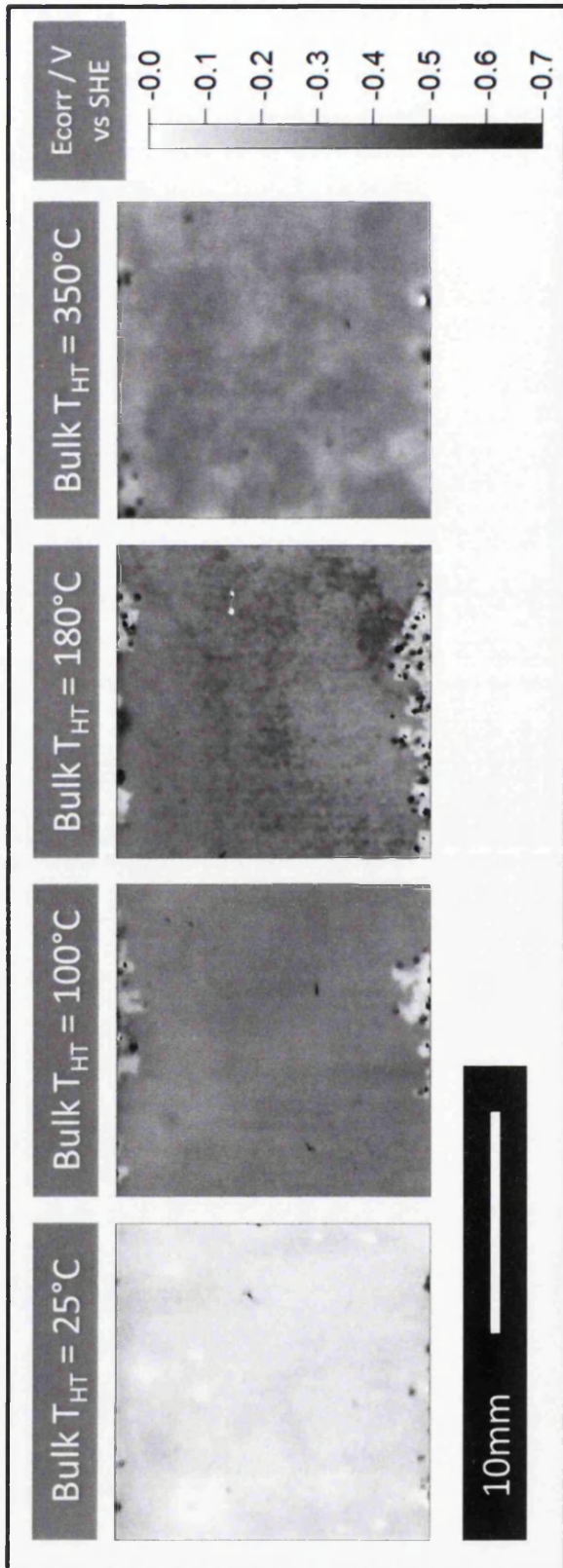


Figure 2.26 Interpolated grey scale maps showing the E_{corr} distribution measured over PVB coated, bulk AA6111 ($T_{HT}=25^{\circ}\text{C}$, 100°C , 180°C and 350°C) in air at 60% RH and 40°C .

The E_{corr} distributions associated with individual successive pitting filaments were studied for bulk samples $T_{HT}=25^{\circ}\text{C}$, 100°C , 180°C and 350°C and are shown in Figure 2.27 as E_{corr} -distance profiles. The E_{corr} values were taken along the axis of filament growth from within the tail near to the defect through the length of the tail and then the head to an intact region beyond. The successive pitting FFC filaments did not generally follow straight paths but the straightest filaments were selected to study here.

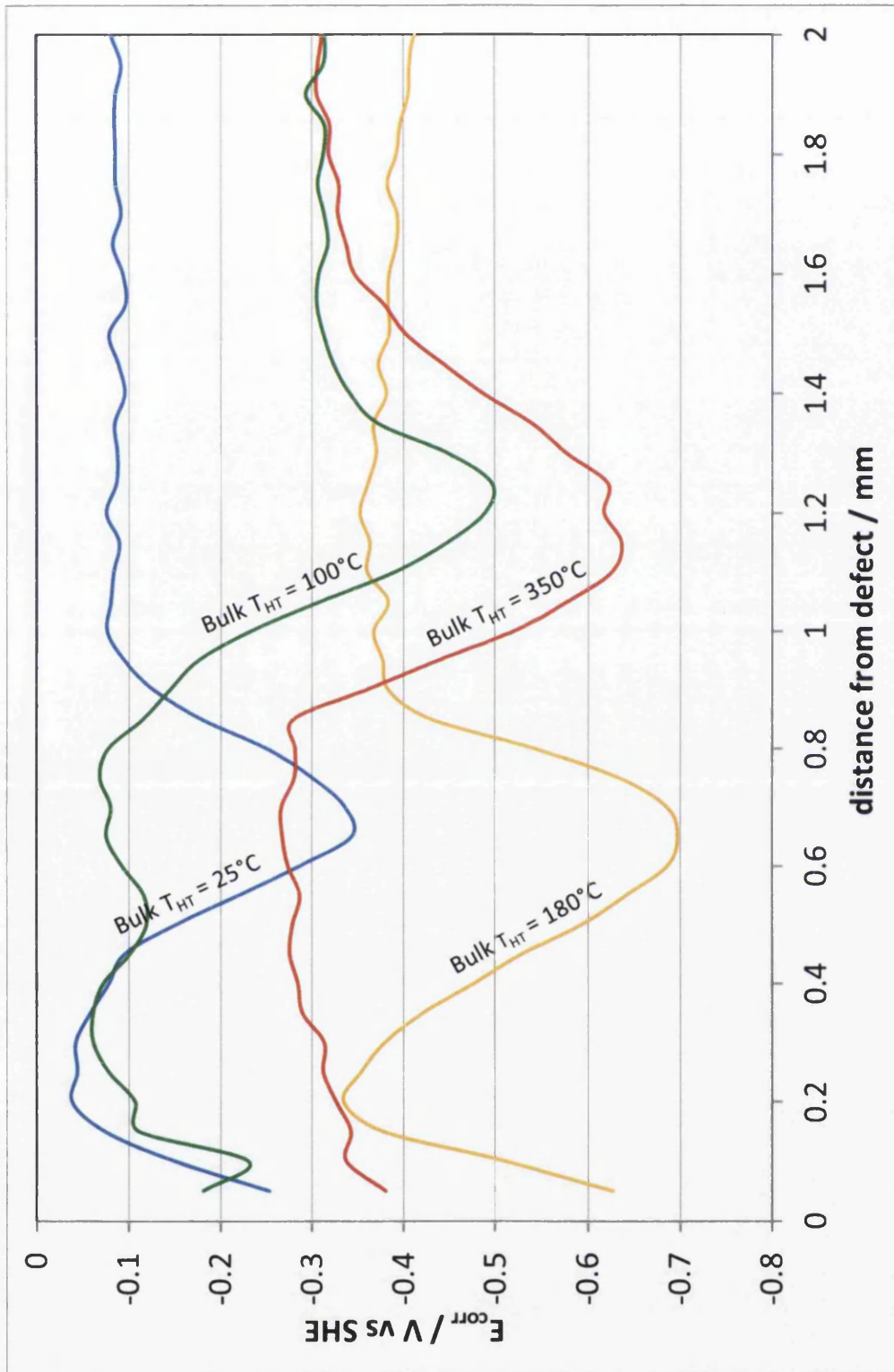


Figure 2.27 E_{corr} - distance profile for successive pitting FFC filaments on PVB coated bulk AA6111 ($T_{HT}=25^\circ\text{C}$, 100°C , 180°C and 350°C) taken along the axis of filament growth.

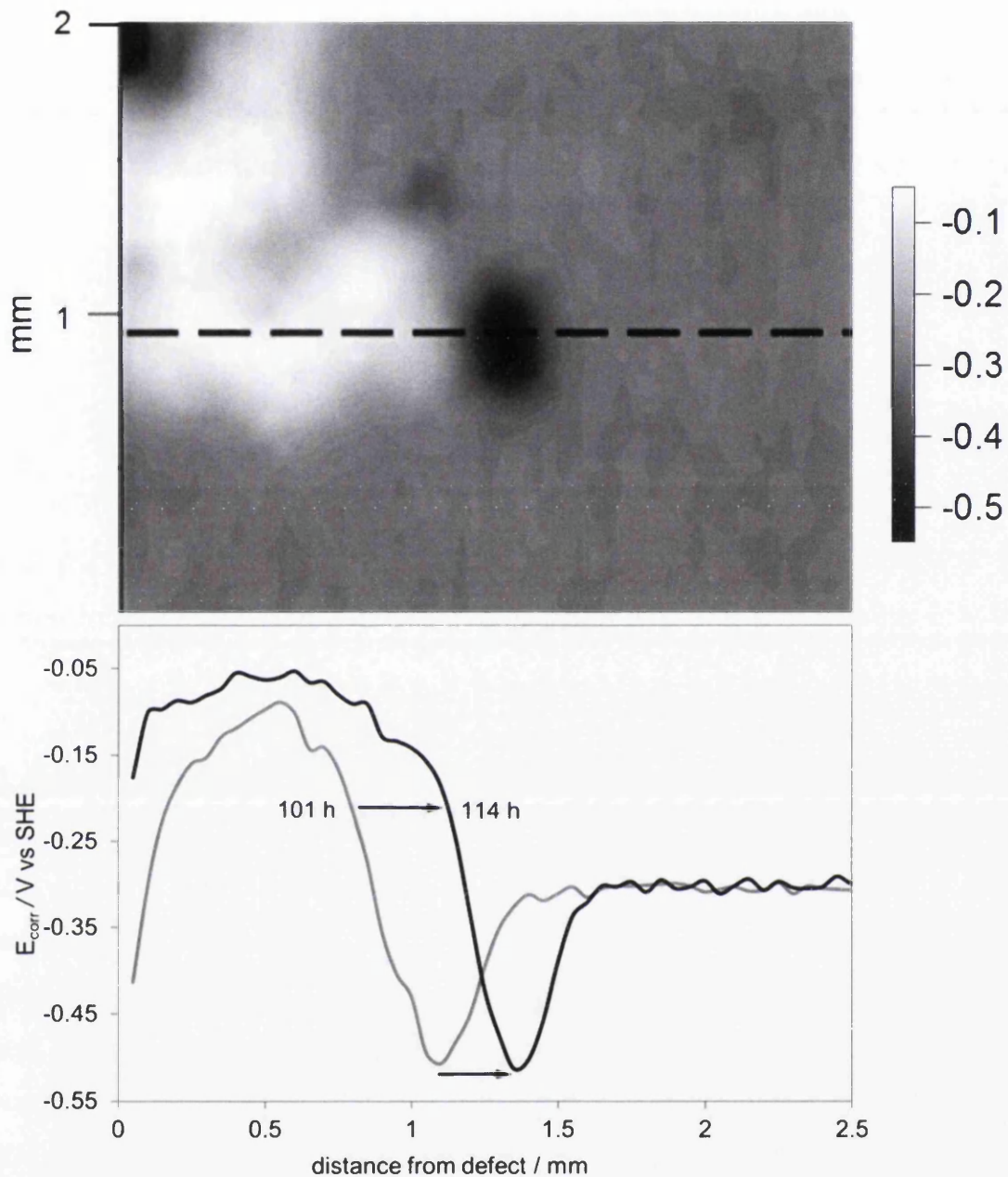


Figure 2.28 (a) Interpolated grey scale map showing E_{corr} distribution over a single successive pitting FFC filament on PVB coated bulk AA6111 ($T_{HT}=100^{\circ}\text{C}$) 114 hours after FFC initiation. (b) E_{corr} - distance profiles along the axis indicated by the dashed line in (a); the time in hours since FFC initiation is indicated.

A PVB coated bulk AA6111 sample with $T_{HT} = 100^{\circ}\text{C}$ was chosen for further examination. The successive pitting filaments were fewer and more easily separated in this condition. **Figure 2.28 (a)** shows a grey scale map of potential 114 hours after FFC initiation. In the corresponding E_{corr} profile (**Figure 2.28 (b)**) measured along the axis of filament propagation (shown as a dashed line in **Figure 2.28(a)**) it can be seen that the successive pitting filament head (the minimum value of E_{corr}) moves further from the defect. Behind it the E_{corr} values increase with time to form the tail. Similar E_{corr} profiles have been reported elsewhere for FFC on copper containing aluminium alloy AA2024 [37, 112].

2.3.6 Filiform Corrosion Kinetics

The propagation kinetics of surface-active FFC were followed by using SKP-derived E_{corr} maps to determine the surface-active filament length L_s . The value of L_s at any time (t) following FFC initiation was taken to be the mean distance (measured normal to the coating defect) between the defect and the advancing corrosion front visible in the corresponding E_{corr} map. **Figure 2.29** is a plot of L_s against time (t) since FFC initiation of PVB coated, DSL bearing AA6111 in the T4 temper and with heat treatments at 100°C , 180°C and 350°C . These filament growth curves were reasonably straight implying a relatively constant filament growth rate ($dL_s/dt = \text{constant}$) over the experimental period. Least squares analysis was used to calculate values of dL_s/dt for each sample and these values are plotted in **Figure 2.30**. It can be seen that the surface active FFC rate is slowest for the sample in the T4 or $T_{HT}=25^{\circ}\text{C}$ condition at 0.044mmh^{-1} but increases with heat treatment to a maximum rate $T_{HT}=180^{\circ}\text{C}$ when a rate of 0.070mmh^{-1} was observed. The sample heat treated at the highest temperature $T_{HT}=350^{\circ}\text{C}$ exhibited surface active FFC with an intermediate growth rate.

The propagation of successive-pitting filaments followed an apparently random path except that they were not observed to cross. There was no evidence that the filaments followed the rolling and grinding direction. This made the accurate

measurement of filament length more difficult. The rates of successive pitting FFC on bulk samples were estimated, very approximately, by determining the mean defect to head distance for the 3 longest filaments on each sample when $t=70\text{h}$ and dividing this distance by t . The successive pitting FFC rates for the bulk samples were plotted in **Figure 2.30** alongside the surface active FFC rates from DSL-bearing samples to allow comparison of the rates of these two modes of FFC attack throughout the range of heat treatments applied in this study. The rates of successive pitting FFC on bulk samples increase with heat treatment temperature up to $T_{HT}=180^\circ\text{C}$ and then decrease for $T_{HT}=350^\circ\text{C}$. In doing so, the successive pitting FFC rate follows the same trend with T_{HT} as do the surface active FFC rates on DSL-bearing AA6111 samples. However in all cases successive pitting rates on bulk samples (0.006-0.018mm/h) are much slower than the corresponding surface active FFC rates on DSL bearing samples (0.07-0.044mm/h).

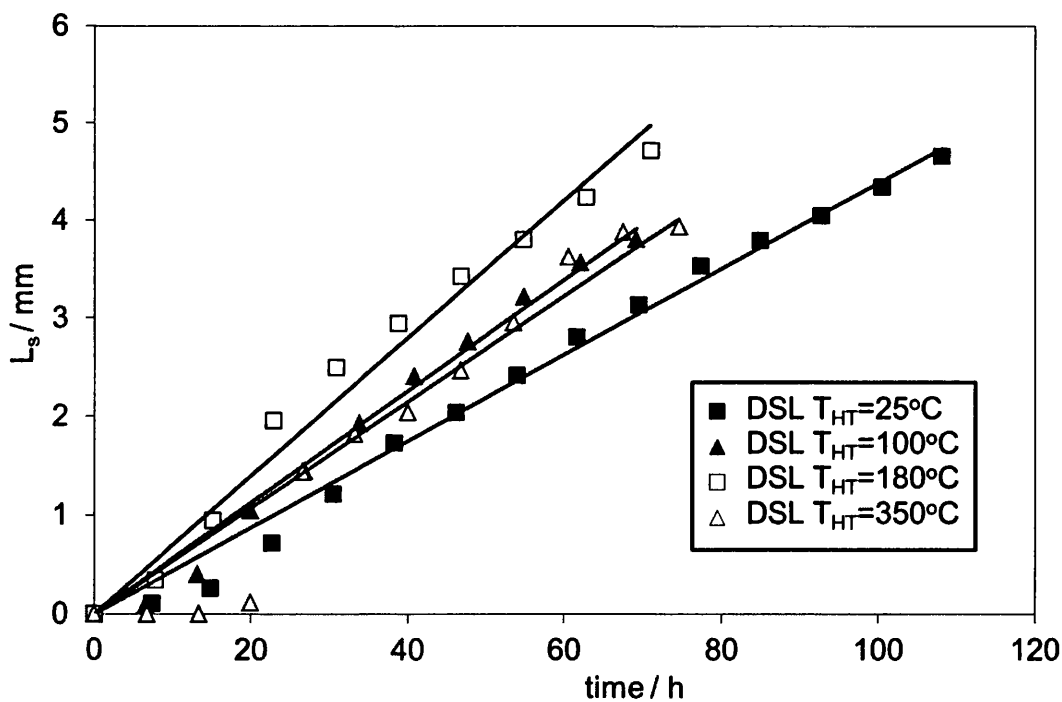


Figure 2.29 Plot of surface-active FFC filament length (L_s) vs time (t) since FFC initiation on PVB coated, DSL-bearing AA6111. The post-abrasion heat treatment temperature (T_{HT}) is as labelled ($T_{HT}=25^\circ\text{C}$ denotes the T4 temper).

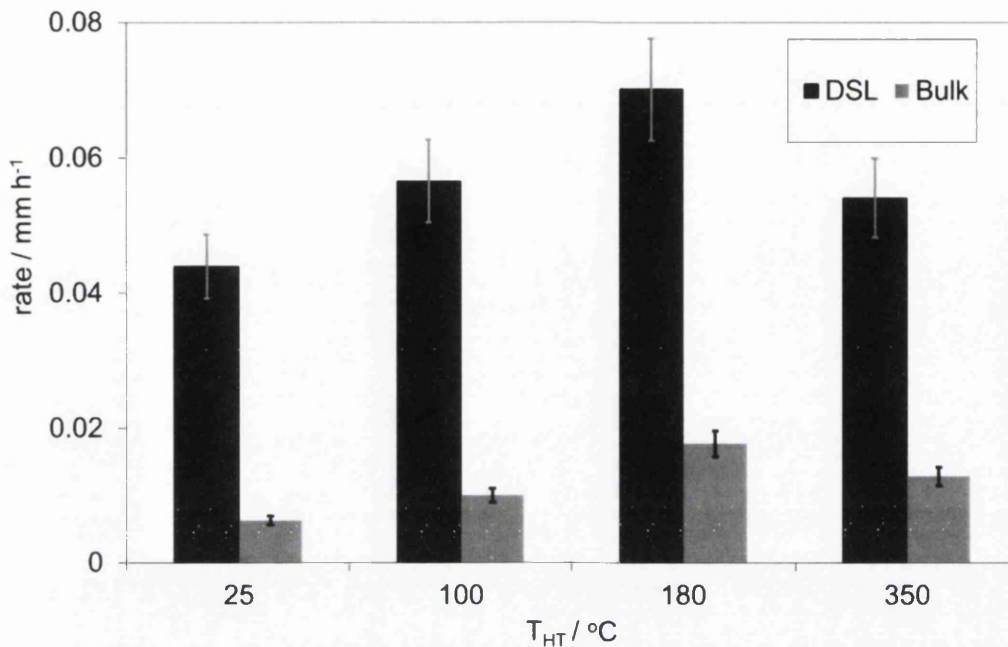


Figure 2.30 Summary of FFC propagation rates on PVB coated AA6111 for the four heat treatment temperatures. Bulk denotes successive-pitting FFC rates on caustic etched AA6111. DSL denotes surface-active FFC rates on DSL-bearing AA6111.

2.3.7 Mechanism of Surface Active FFC

It has been shown here that DSLs on AA6111 are anodically activated relative to the bulk and elsewhere [74] that the metal dissolution that occurs as a result of surface active FFC is effectively limited to the DSL. Figure 2.31 illustrates the proposed mechanism underlying surface active FFC. The lower portion of Figure 2.31 is a schematic representation of the characteristic surface active FFC E_{corr} - distance profiles typified in Figure 2.23. The schematic diagram of the surface active FFC filament corresponds with regions of the E_{corr} - distance profile. In region (i) ahead of the filament, the coating and DSL are still intact and the SKP registers E_{intact} . The filament head comprises aqueous HCl and partially hydrolysed aqueous $AlCl_3$. Region (ii) corresponds to the front of the filament head electrolyte droplet where it comes into contact with the DSL. The DSL undergoes dissolution as the principal anode of the surface active FFC corrosion cell. Here the corrosion potential is equal to that of region (i) so is not resolved using SKP potentiometry in this study. This

anodic attack is, at least initially, intergranular but the small grain size and the consequently high density of grain boundaries results in the DSL being almost completely consumed [74]. Region (iii) corresponds to the remainder of the filament head where the DSL has dissolved and the head electrolyte makes contact with bulk AA6111. Facile diffusion of gases through the filament tail into this region of the head makes it the primary site of cathodic oxygen reduction [32, 33]. In region (iv), the filament tail, Al^{3+} aquocations become fully hydrolysed precipitating solid Al(III) (hydr)oxide corrosion product. Here, no water soluble electrolyte is present and the corrosion product loses water through osmosis. It is this that makes it dry and porous, allowing rapid diffusion of atmospheric oxygen [32, 33].

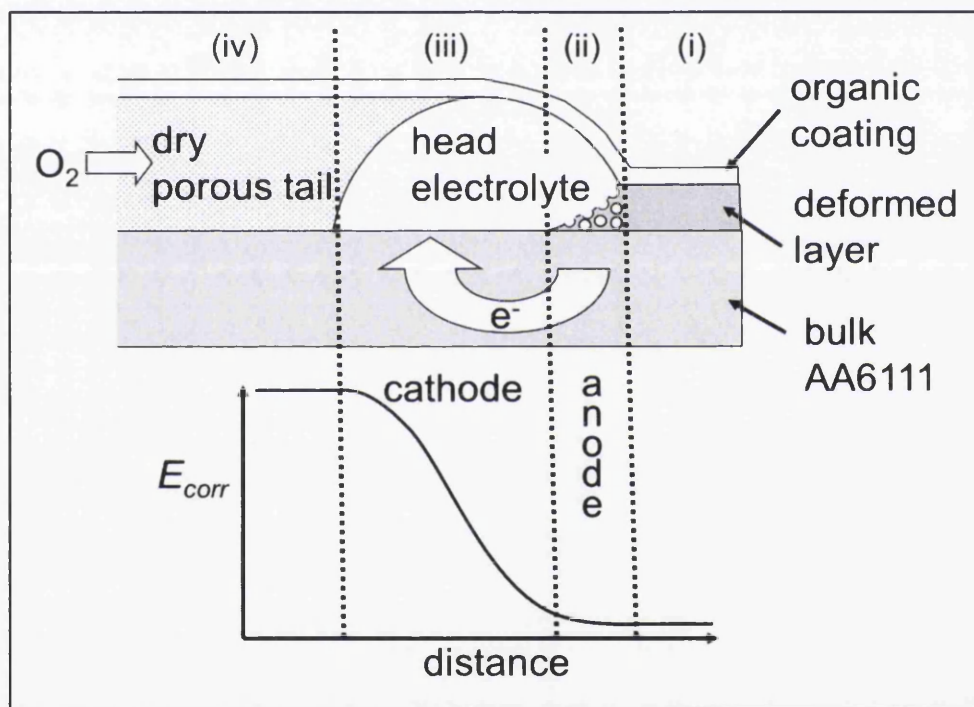


Figure 2.31 Schematic representation of proposed relationship between SKP measured E_{corr} - distance profiles and physical regions within the surface active FFC corrosion cell.

As in most forms of FFC, differential aeration is probably an important driving force underlying the mechanism shown in Figure 2.31. However, the mechanism proposed here includes an additional driving force provided by the anodic activation of the DSL relative to the bulk AA6111. The FFC cell potential includes a contribution arising from the dissimilar electrochemical characteristics of the DSL

still present at the front of the surface active FFC head and the bulk AA6111 at the back, which has been exposed by DSL dissolution. Experiments which produced surface active FFC on DSL bearing AA6111 did not produce this mode of attack on bulk samples. This suggests that the additional driving force described above is necessary for surface active FFC to occur. Figure 2.11 quantifies this additional contribution to the FFC corrosion cell potential as $\geq 0.3V$. In Figure 2.12 the potential difference between the DSL and bulk portions of the sample surface is approximately 0.2V. The superficial nature of surface active FFC attack can be explained on the basis of the DSL-bulk potential difference; the DSL is anodically activated relative to the bulk and so sacrificially protects the bulk even when it is exposed to the aggressive FFC head electrolyte. This cathodic protection relies on the galvanic coupling of the DSL with the bulk.

Dealloying of Q phase particles, which are thought to be present at grain boundaries within the DSL, results in magnesium loss and leaves behind copper rich residues. These cathodic copper rich residues couple microgalvanically with the adjacent aluminium matrix. Differential aeration between the front of the head (region (ii)) and the back (region (iii)) will cause the principal sites of cathodic and anodic activity to become separated by a distance approximately equal to the diameter of the filament head electrolyte droplet (Figure 2.31). The level of cathodic oxygen reduction towards the rear of the filament head where the DSL has been removed by preceding anodic dissolution will probably depend both on the extent of copper rich phase precipitation in the bulk alloy and on the quantity of copper left behind by the DSL dissolution. The values of E_{corr} marked 'tail' in Figure 2.11 are taken from the region of high E_{corr} behind the surface active FFC front on DSL bearing AA6111. As such, they eliminate the contribution of etching induced copper enrichment which affects the E_{intact} values shown for bulk AA6111.

Figure 2.21, Figure 2.22 and Figure 2.30 show evidence that AA6111 samples in the T4 condition ($T_{HT}=25^{\circ}C$) can corrode by rapid surface active FFC when they have been abraded to introduce a DSL. In previous work [74] on AA6111 discrete Q phase DSL grain boundary precipitates were not resolved in the absence of post abrasion heat treatment. These findings together suggest that microgalvanic

coupling between these Q phase precipitates and the adjacent aluminium matrix may not be necessary for surface active FFC to occur.

The galvanic component of the surface active FFC driving force arises from the difference between E_{intact} of the DSL and E_{corr} of the tail (Figure 2.11). This difference is shown to be approximately constant between $T_{HT}=25^{\circ}\text{C}$ (DSL Q phase not resolved) and $T_{HT}=350^{\circ}\text{C}$ and of magnitude $0.55\text{V}\pm 0.1$. Hence, this component of the driving force appears to be independent of discrete DSL grain boundary precipitation. The invariance of this additional galvanic component of the surface active FFC driving force with heat treatment temperature is consistent with the results shown in Figure 2.30. Here the difference between the surface active FFC rates for the DSL bearing AA6111 and for the bulk remains approximately constant across all heat treatments. This reflects the invariance with T_{HT} of the additional galvanic driving force associated with the DSL. It is thought that copper provides the main oxygen cathode [93]. Copper will become available through DSL dealloying of the DSL grain boundary Q phase precipitates where these are present. However, this is not essential for the provision of copper since Cu^{2+} cations are dissolved with the DSL and replated on the bulk surface and copper rich phases in the bulk are exposed following the DSL dissolution.

2.3.8 Mechanism of Successive Pitting FFC

Figure 2.32 illustrates the proposed mechanism for successive pitting FFC on AA6111. The lower part of the diagram shows the characteristic E_{corr} - distance profile for a successive pitting FFC filament as in Figure 2.26 and Figure 2.27. The upper part shows the corresponding physical regions within the successive pitting FFC cell. In region (i), which is the uncorroded area in front of the head, the PVB coating is intact. In region (ii) the filament head electrolyte makes contact with the bulk AA6111 surface beneath the PVB coating. Figure 2.24 (b) shows the morphology of the corroded bulk AA6111 surface and suggests that the mode of anodic attack in this region is intergranular. Cathodic oxygen reduction occurs

where bulk AA6111 has already been subject to anodic dissolution and so there is likely to be some degree of copper enrichment as a result of previous dealloying, replating etc [93]. The overall level of cathodic activity is likely to be dependent on the precipitation of copper rich grain boundary phases in the bulk alloy. Region (iii) is the successive pitting FFC tail, where Al^{3+} cations precipitate as Al(III) (hydr)oxide, which becomes progressively dehydrated through osmosis. The processes in the tail are similar to those in the case of surface active FFC.

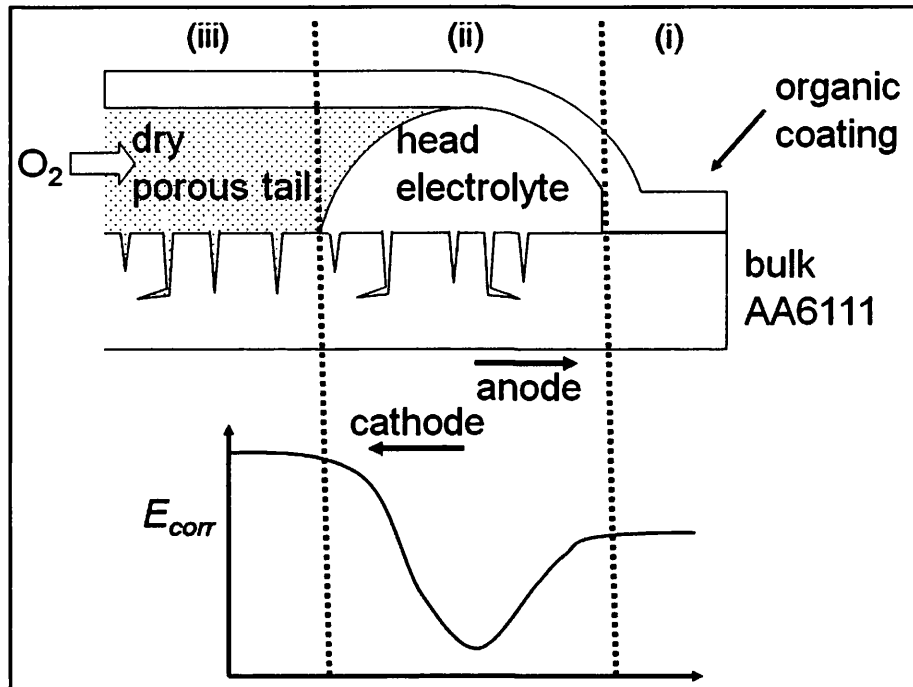


Figure 2.32 Schematic representation of proposed relationship between SKP measured E_{corr} - distance profiles and physical regions within the successive pitting FFC cell

As has been stated previously, it appears that the successive pitting FFC mechanism illustrated in Figure 2.32 can only take place when either there is no DSL or when the DSL has been removed by preceding surface active FFC (Figure 2.21 and Figure 2.26). This is because the anodically activated DSL cathodically protects the bulk AA6111. The main driving force for successive pitting FFC is likely to be differential aeration resulting from the facile diffusion of oxygen through the dry and porous filament tail [32, 33]. This forces net anodic activity towards the front of the filament head droplet.

2.3.9 Filiform Corrosion on Pure Aluminium

A sample of 99.999% purity aluminium was abraded and then coated and initiated by the standard procedure. The sample was then placed inside a desiccator within which the environment was maintained at 80% relative humidity and 25°C.

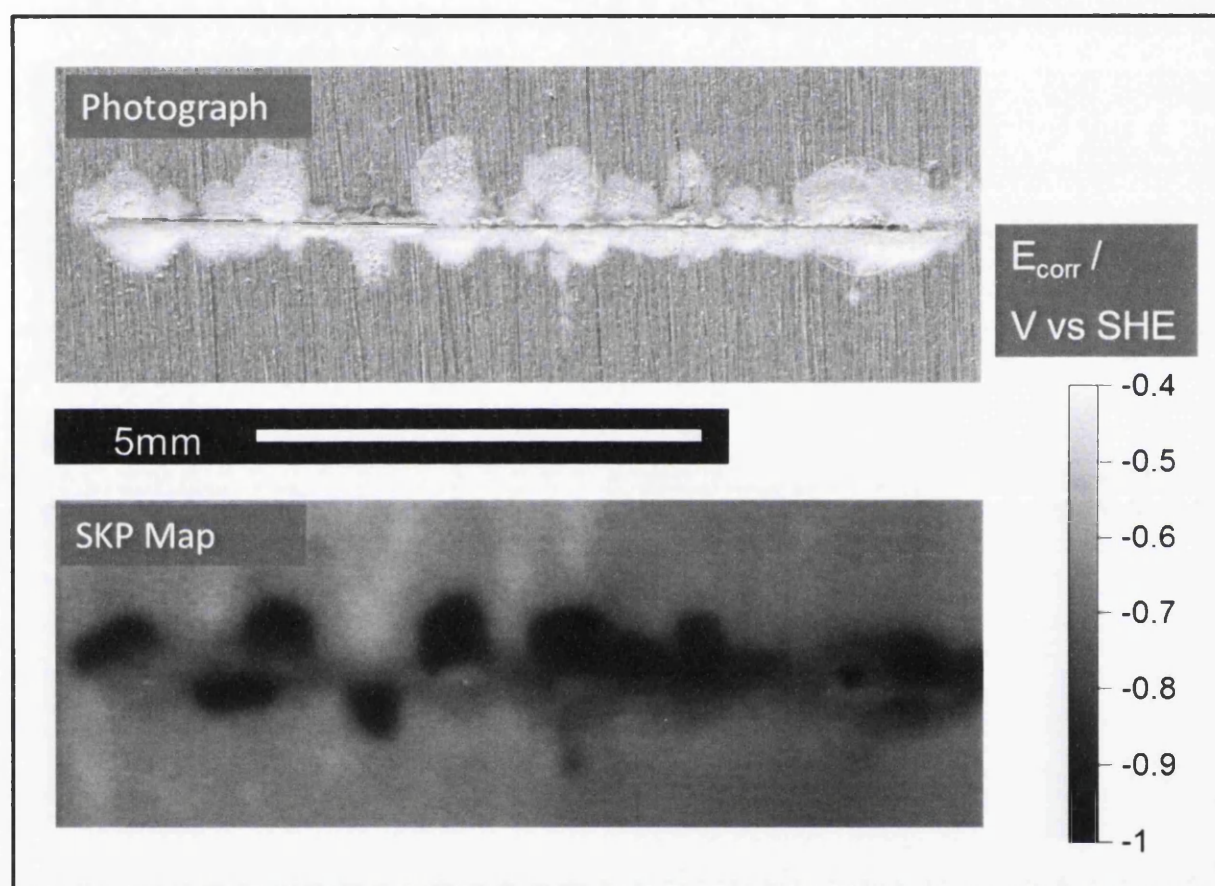


Figure 2.33 Photograph (top) and SKP E_{corr} map showing filiform corrosion on a sample of pure (99.999%) aluminium after four weeks in 80% relative humidity at 25°C.

After four weeks the sample showed a small amount of FFC (Figure 2.33). The FFC filaments were relatively thick (probably as a result of the high humidity) and did not propagate far from the defect. The finding that FFC occurred on a DSL-bearing pure aluminium sample coupled with the fact that it was found impossible to induce FFC on bulk pure aluminium samples [118] suggests that the DSL can be anodically activated by abrasion as was suggested by the result shown in Figure 2.14.

Alloys such as AA6111 contain metallic alloying additions which are capable of forming precipitates at grain boundaries. It is therefore reasonable to suggest that these intermetallics play an important role in developing the electrochemical characteristics of the DSL. However this is not the case for the pure aluminium sample for which the potential depression caused by abrasion must result from a difference in the intrinsic properties of the aluminium in the DSL. These intrinsic differences may relate to the high number of high angle grain boundaries and the high strain within DSL. Areas of higher strain have a tendency to become anodic.

In another study [118] it was shown that much more significant filament propagation can be induced on pure aluminium (prepared by a similar method) when a feasible cathode is present. A Cu^{2+} cation exchange pigment was incorporated into the coating which become re-plated as Cu to act as an oxygen cathode. Surface-active FFC was shown to propagate approximately 8mm away from the defect in a period of 1 week when held at a relative humidity of 93% at room temperature.

2.4 Conclusions

Scanning Kelvin Probe potentiometry has shown that AA6111 with an abrasion-induced deformed surface layer exhibits a significantly more negative potential than the bulk alloy. The potential difference between the deformed surface layer and the bulk is greater than 0.3 V irrespective of whether the material is in the T4 temper or has been heat treated for 2 hours at between 100°C and 350°C.

For PVB coated AA6111 samples, after an initiation procedure involving the application of a known quantity of dilute aqueous hydrochloric acid to a penetrative defect in the coating, filiform corrosion is observed for all tempers. The presence of a deformed surface layer results in a rapid and superficial FFC attack which appears to be limited to the depth of the DSL, this has been termed surface active FFC. In the absence of a DSL a much slower and more deeply penetrating form of FFC is

observed which we have termed successive pitting FFC. Successive pitting FFC occurs both on samples which have been chemically cleaned to remove the DSL and as a secondary attack on samples where preceding surface active FFC has substantially removed the DSL.

Heat treatment of AA6111 for 2 hours at temperatures between 100°C and 350°C increases the rates of both surface active and successive pitting FFC compared to the T4 temper. The rates of both forms of FFC reach a maximum for a heat treatment temperature of 180°C.

The appearances of surface active and successive pitting corroded AA6111 surfaces are consistent with intergranular attack. Where successive pitting FFC has occurred the localised corrosion features are separable on a scale similar to the grain size of the bulk alloy which is approximately 20µm. Where surface active FFC has occurred metal dissolution appears to be localised on a much smaller scale of 0.1µm to 1µm which is similar to the reported size for grains within the DSL of AA6111.

The lower potential and higher corrodibility of DSL bearing AA6111 surfaces indicate that the DSL is anodically activated relative to bulk AA6111. A mechanism for surface active FFC has been proposed whereby anodic activation to intergranular attack causes the DSL to react sacrificially to the bulk AA6111 beneath and contributes substantially to the driving force.

Surface active and successive pitting FFC rates show a similar dependence on the heat treatment temperature; this is consistent with the thermally promoted precipitation of copper rich intermetallic phases in both the DSL and the bulk providing sites for the primary cathodic reaction; the reduction of oxygen in the tail. Because the DSL is substantially removed during the anodic process of the surface active FFC attack, copper which is exposed or re-deposited on the surface of the bulk alloy is likely to provide the principal site of oxygen reduction in both surface active and successive pitting FFC.

Chapter 3: Accelerated Corrosion Testing of Coated Architectural Aluminium Products

3.1 Introduction

Architectural aluminium sheet is often used outdoors and so needs to have good corrosion resistance in order to live up to the warranty which is usually supplied with it. The corrosion resistance is dependent on the composition and temper of the alloy and on the pre-treatment and coating applied to it. New architectural aluminium sheet products are being developed all of the time and these all need to be tested to determine their level of corrosion resistance. This allows comparison with products already on the market as well as other newly developed products. The most accurate method of testing is to subject the product to in-service conditions but this is rarely practical, especially for a product which is not yet on the market. In order to model the in-service environment the samples are exposed at appropriate outdoor sites and can be subjected to some method of accelerating the corrosion such as regular spraying with salt solution. Accelerated laboratory tests can be more useful because they allow products to be evaluated and put on the market much more quickly. Accelerated laboratory tests often involve the use of a test cabinet which can control the environment the samples are exposed to. These can be programmed to vary factors such as temperature, humidity and electrolyte composition over time.

The difficulty lies in finding an accelerated test which can accurately predict the in-service corrosion behaviour of the product. Leth-Olsen [43, 95], Afseth [31] and Scamans [42] used the Lockheed method with a modification to the initiation step whereby the standard exposure to HCl vapour was replaced by immersion for 1 or 2 hours in aluminium chloride solution. This modification was designed to provide a less aggressive test which would be suitable for alloys with thin polymeric coatings.

Leth-Olsen [43] reported a good correlation between sample rankings for this modified Lockheed FFC test and outdoor exposure at Hoek van Holland in the Netherlands for coated AA3105 and AA8006 alloys subjected to various pre-treatments. Hoek van Holland is a relatively severe marine and industrial environment.

The purpose of this work is to develop a low cost accelerated filiform corrosion test which provides results which correlate well with outdoor exposure test data for a very varied range of architectural aluminium sheet products. The method chosen for investigation involved creating a small penetrative defect in the coating and directly applying a measured quantity of hydrochloric acid before incubating the sample in a warm and humid atmosphere. Other standard methods involve exposing the defect to an atmosphere containing the aggressive substance. The method of direct exposure to the acid used here has the advantage of greater controllability. The two test variables investigated were the molarity of the acid and the duration of the exposure. Half molar, one molar and two molar concentrations of hydrochloric acid were each used for tests with durations of 48 and 600 hours.

3.2 Experimental

3.2.1 Materials

New accelerated test methods were evaluated on a set of 37 architectural aluminium alloys supplied by Novelis. These samples varied widely in terms of their alloy composition, temper, pre-treatment and coating. The alloys were all of the AA3000 or AA5000 series of wrought aluminium alloys in a range of tempers which had been chemically pretreated and, in most cases, both a base coat and a top coat had been applied. Hydrochloric acid and ammonium sulphate were supplied by Sigma Aldrich.

3.2.2 Accelerated Applied Acid Test

This test is based on a method of initiation which has been used in previous work on filiform corrosion of coated iron and aluminium alloys [101, 119, 120] and is used in the 'Filiform Corrosion of AA6111' chapter in this thesis. The temperature and humidity conditions are based on those used in the standard Filiform corrosion or 'Lockheed' test [121].

The accelerated applied acid (AAA) test was evaluated for all 6 HCl molarity and exposure time combinations (0.5M-48hr, 1M-48hr, 2M-48hr, 0.5M-600hr, 1M-600hr, 2M-600hr). Sets of at least 10 preliminary samples were tested for each AAA test variant in order to determine the combination which gave the best agreement with the outdoor test results. The most successful AAA test variant was then subjected to further evaluation on the complete set of 37 samples.

The sample sheets were cut into 40mm by 40mm coupons. Two dots were marked 30mm apart on each coupon to enable subsequent calibration of distance on post-test photographs.

A scalpel was used to scribe two 10mm defects, 10mm apart, into one coupon from each sample. The defects penetrated the coating to expose the substrate beneath and were orientated perpendicular to the rolling direction. Figure 3.1 shows the positioning and dimensions of the defects on a coupon.

1 μ l of 2 Molar HCl was injected into a glass micro-capillary tube using a syringe. The acid was then applied to the defect to initiate corrosion. This was repeated for each defect.

After initiation the samples were placed in an airtight desiccator which contained a saturated ammonium sulphate solution to maintain the relative humidity at approximately 80%. The desiccator was placed within an air bath which maintained a temperature of approximately 40°C (Figure 3.2 and Figure 3.3). Samples were left for 48 or 600 hours before they were photographed.

After testing, the extent of corrosion was quantified by measuring the total filament length for the two defects. This was done using 'Sigma Scan' software which is produced by Systat Software Inc. The distance was calibrated from the photographs using the two dots which had been marked 30mm apart on the coupons. Lines were then drawn electronically following the path of each filament and the total length of these lines was determined by the programme.

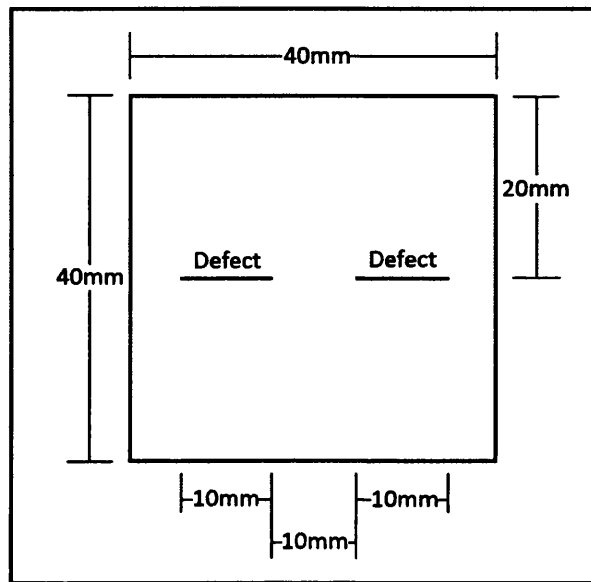


Figure 3.1 Standard sample for the accelerated applied acid test.

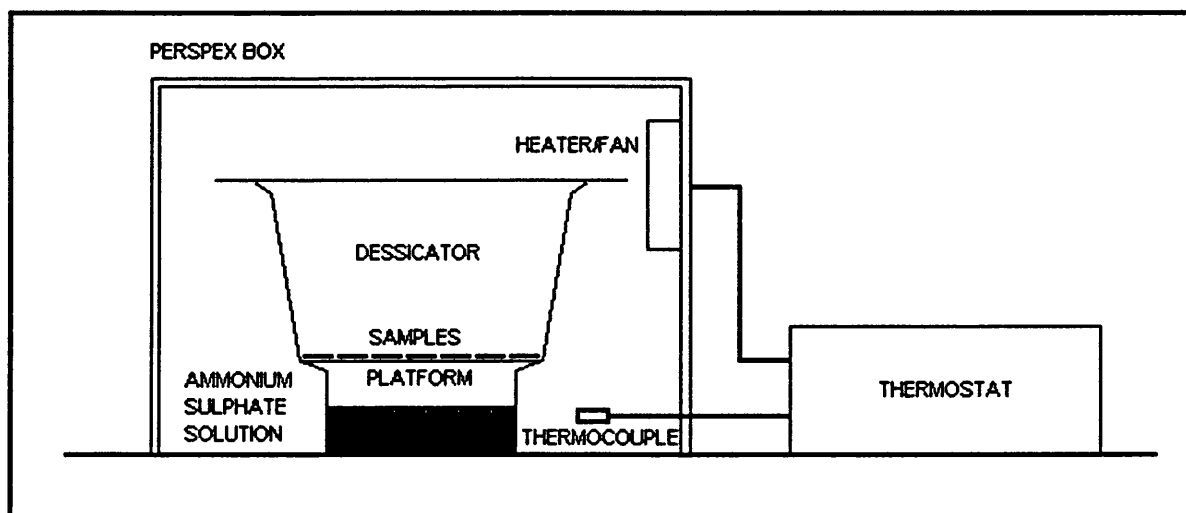


Figure 3.2 Accelerated applied acid test equipment setup.



Figure 3.3 Photographs showing the accelerated applied acid test humidity chamber and thermostatically controlled air bath equipment.

The above procedure was repeated using 1 Molar and 0.5 Molar HCl, except that, having established the extent of corrosion generated by the 2 Molar HCl it was found to be possible to introduce four, instead of two, defects onto each sample without restricting the space available for FFC growth unacceptably. 1 Molar HCl was applied to two of the defects and 0.5 Molar HCl was applied to the remaining two defects.

Once correlation coefficients had been calculated (**Equation 3.1**) the best-performing molarity/exposure time combination was identified and further testing was carried out. The samples which were omitted previously were tested and then repeat testing was carried out on all the samples. The method used was that described above for the 2 Molar HCl concentration. Averages of the two tests were calculated for each sample.

Novelis provided results from two other accelerated laboratory tests and from a field test in the severe marine environment on the south coast of Sweden. The laboratory tests were a cyclic TNO cabinet test and a standard Lockheed test. These

tests were carried out on a similar set of the 37 materials. Experimental methods for these tests are as follows:

3.2.3 Outdoor Field Test

In this test 170mm by 200mm samples of each material were prepared. Along one of the 200mm edges a conical bend of 0.5 to 6mm radius was formed in line with the rolling direction. Two scribe marks were made along the length of bottom 170mm edge, perpendicular to the rolling direction. The top scribe mark was used for the measurement of filiform corrosion and is the only feature relevant to this study. Other features were designed to test other aspects of corrosion susceptibility which are not covered here.

Samples were sited in Bohus Malmön which is a severe environment on the south coast of Sweden. Samples were exposed vertically and faced north. They were inspected after 1, 2, 3 and 5 years. FFC was quantified as a perpendicular distance from the scribe in mm.

3.2.4 Cyclic Cabinet Test

Sample preparation was as for the outdoor field test. A cabinet, manufactured by TNO, was used for this laboratory based accelerated test. The test comprised a 24 hour wet-dry cycle that included:

1. 14 hours @ 30°C and 75% RH
2. 3 hours @ 60°C and 50% RH
3. 2 hours 30 minutes @ 60°C and 50% RH
4. 7 hours @ 30°C and 96%RH including four 30 minute periods spraying a fog of artificial rainwater (this part of the test was designed to promote blister corrosion).

The artificial rainwater composition was based on Netherlands coastal region analysis with NaCl substantially increased to simulate salt accumulation on exposed

surfaces. 440ppm SO₂ was also added plus CO₂ to give constant 0.4% v/v concentration. Accumulated salts were removed by washing during inspection. The duration of this test was 1008 hours. FFC was quantified as a perpendicular distance from the scribe in mm.

3.2.5 Lockheed Test

Sample preparation was as for the outdoor field test. The panels are then exposed to a vapour of chloridric acid for one hour before being placed in a humidity chamber at approximately 82% relative humidity and approximately 38°C. The duration of this test was 1008 hours. FFC was quantified as a perpendicular distance from the scribe in mm.

3.3 Results and discussion

3.3.1 Preliminary Test Results

The accelerated applied acid (AAA) test was initially evaluated for 6 HCl molarity and exposure time combinations (0.5M-48hr, 1M-48hr, 2M-48hr, 0.5M-600hr, 1M-600hr, 2M-600hr). Sets of at least 10 preliminary samples were tested for each AAA test variant in order to determine the combination which gave the best agreement with the outdoor test results.

A quantitative measurement of the level of agreement between sets of test data is useful in selecting the test conditions which can most accurately predict outdoor corrosion behaviour. In this study Pearson's Product Moment Correlation Coefficient, r (Equation 3.1), is calculated for each set of accelerated test data when compared to the outdoor test data after both three and five years. All the r values calculated for the preliminary test data against the 3 and 5 year outdoor data are shown in Table 3.1 along with correlations for the cyclic and Lockheed tests on all 37 samples.

Equation 3.1:

$$r = \frac{\sum(x - \bar{x})(y - \bar{y})}{\sqrt{\sum(x - \bar{x})^2 \sum(y - \bar{y})^2}}$$

			Outdoor	
			3 year	5 year
Accelerated Applied Acid Test	2	48h	0.61	0.63
	Molar	600h	-0.01	0.00
	1	48h	0.19	0.27
	Molar	600h	0.35	0.35
	0.5	48h	0.84	0.83
	Molar	600h	0.68	0.68
Cyclic Cabinet			0.55	0.55
Lockheed			0.48	0.53

Table 3.1 Pearson's product moment correlation coefficients for preliminary results from three variants of the accelerated applied acid test, results from the cyclic TNO cabinet test and results for the standard Lockheed test all against both 3 and 5 year outdoor exposure data. Note: Cyclic cabinet and Lockheed correlations are for larger data sets than AAA.

The 0.5 Molar HCl, 48 hour data gives the best correlation with the outdoor field test data for both 3 and 5 year exposure ($r=0.84$ and $r=0.83$ respectively). The correlation is higher than that between the cyclic cabinet test data and the outdoor field test data ($r=0.55$ for both the 3 year and 5 year data) and it is also higher than the correlation between the Lockheed test data and the outdoor field test data ($r=0.48$ against 3 year outdoor data and $r=0.53$ against 5 year outdoor data).

The variant of the AAA test which used 0.5 Molar HCl for FFC initiation and a 48 hour exposure duration was selected as the most promising test and was therefore

applied to the complete set of 37 coated architectural aluminium alloy samples. Preliminary results are for only 10 samples so these correlations have relatively low statistical significance. Increasing the number of samples to 37 will give much greater certainty about the strength of any true correlation which may exist between results for the AAA and outdoor exposure tests. Unless otherwise stated it can now be assumed that 'AAA test' refers to this variant of the test.

3.3.2 Test Evaluation Criteria

Although Pearson's correlation coefficient has been used to evaluate the AAA test variants from the preliminary results there are number of methods which can be employed to evaluate accelerated laboratory corrosion tests. In all cases the accelerated test data will need to be compared to a corresponding set of data from either in-service or outdoor exposure testing. In this work comparisons are made against data from outdoor exposure testing in a severe marine environment in Sweden. It is important to realise that this data, which is taken as the standard against which other data sets are compared, will not necessarily accurately predict the performance of the set of materials when they are used by the customer. Locations can have very different atmospheres depending on their proximity to the coast and to different types of industry. The weather also has a large influence, particularly the levels of UV exposure and precipitation. The outdoor exposure site was chosen as a 'worst case scenario' because it is thought to be relatively aggressive and although this approach is useful when predicting the maximum extent of attack across a set of samples, individual samples are likely to perform differently at different locations.

Accelerated corrosion tests are used for a number of purposes and the evaluation of them depends on what are considered to be the most important corrosion performance characteristics for the product. For example, there might be a threshold level of corrosion which is thought to be acceptable in service and beyond which the product is said to have failed. If this is the case then the accelerated test

methods should be evaluated on their ability to predict in-service or outdoor exposure performance on a fail / no fail basis. In other circumstances it might be more important that the test can predict the amount of corrosion likely to occur on a given sample after a certain period of use in which case the correlation between the accelerated corrosion test data and the standard data set would be a much better measure of the suitability of the test. If an accelerated corrosion test was required only to determine the most resistant product then the tests should be evaluated on their ability to rank samples in the same order as the standard results and it might be advantageous to have a test which caused all of the samples to corrode so that there was differentiation between the most resistant samples.

A number of different criteria will be used to evaluate the performance of the accelerated corrosion tests included in this work. This will show what each test is most suitable for and will illustrate some interesting differences between the methods.

3.3.2.1 Corrosion Morphology

The photographs in Figure 3.4 show the corrosion on some of outdoor samples after 5 years of exposure (left) along with the corresponding AAA test samples (right). It is useful to study the morphology of the corrosion that occurs as a result of any kind of accelerated test and compare it to the corrosion on the in-service or outdoor exposure samples which are not accelerated. This is important because if the type of corrosion is different in the test then it is likely to be unreliable in predicting the behaviour of materials before they go into use.

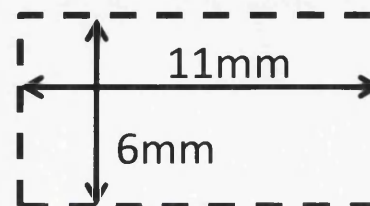
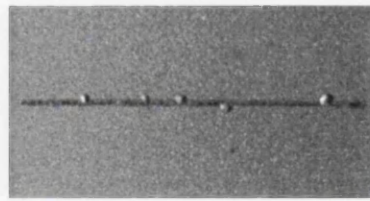
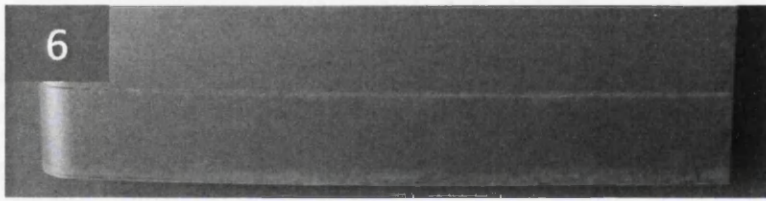
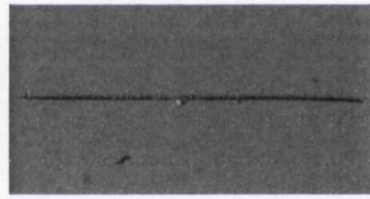
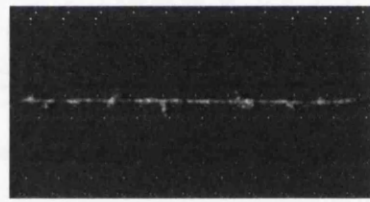
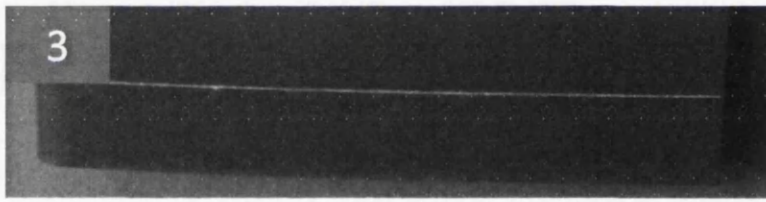
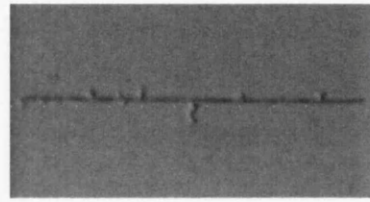
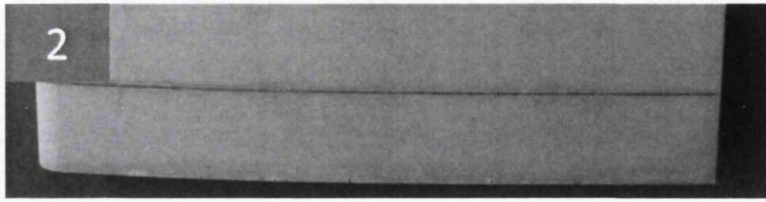
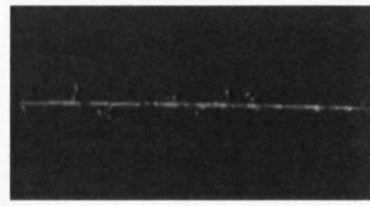
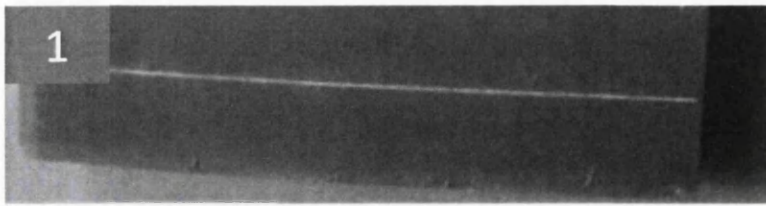
The post-test photographs of the AAA samples show that FFC was the dominant corrosion type, in fact no other forms of corrosion was identified on any of the samples tested. On some of these AAA-tested samples a number of relatively long filaments had been formed (for example samples 10, 31 and 32 as shown in

Figure 3.4). The corrosion on sample 10 after the AAA test has a similar morphology to that on the outdoor exposure tested sample but is more severe. On other AAA-tested samples the filaments formed but did not propagate far from the defect (samples 4, 6, 7, 8, 9 in Figure 3.4). It is possible that the longer filaments were of the surface-active FFC type formed as a result of the presence of a deformed surface layer on the aluminium substrate and that the more restricted FFC propagation was of the successive pitting type as a result of the absence of a deformed layer on those samples. In general the samples which formed short FFC filaments during the AAA test did not corrode at all in the outdoor exposure test. The highly accelerated and aggressive conditions in which the AAA samples were tested may have 'forced' successive pitting FFC which would not have otherwise occurred.

The two samples which corroded the most in outdoor exposure testing were samples 31 and 32 and these samples also performed poorly in the AAA test. The morphology of the corrosion on these samples after outdoor exposure was identified as FFC but was bordering on blistering as large areas of the coating became detached from the substrate. The morphology of corrosion on sample 31 and 32 after AAA testing was purely FFC. It is possible that this difference is the result of the outdoor samples being exposed to higher humidity conditions for part of the 5 year testing period which tends cause FFC susceptible samples to instead become susceptible to blistering. Another possibility is that the coating became degraded as a result of weathering in the outdoor conditions. However the detachment of the coating might simply result from more extensive corrosion on the outdoor exposure samples.

The AAA test method is designed specifically to accelerate the growth of filiform corrosion. The relative humidity of 80% and temperature of 40°C should be the most suitable for its rapid growth. The absence of blistering on the AAA-tested samples is therefore unsurprising. The Lockheed test is also designed to test for FFC and is performed at a similar humidity as the AAA test so would not be likely to cause any blistering either. The cyclic TNO cabinet test would be most suitable for predicting any blistering behaviour because it involves a phase in the cycle

specifically designed to promote blister formation. Indeed the supplied results for blistering show none on samples 31 and 32 for the Lockheed test and severe blistering on these samples for the cyclic test.



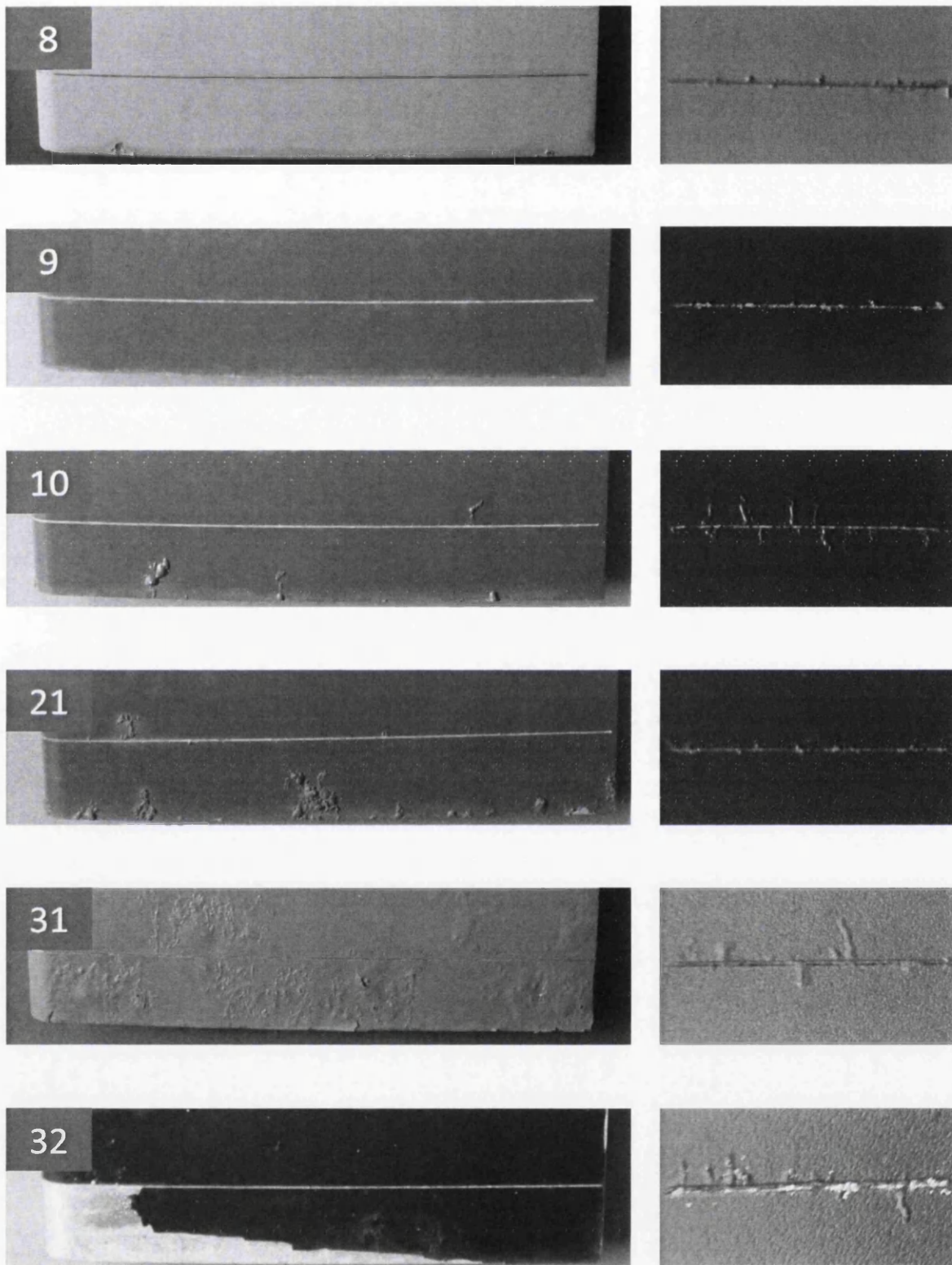


Figure 3.4 Photographs showing samples after the 5 year outdoor exposure test (left) and the 48 hour-0.5M HCl variant of the accelerated applied acid test (right). Sample numbers are shown in the grey boxes.

3.3.2.2 Pearson's Product Moment Correlation Coefficient

Where it is important to predict the quantity of corrosion that is likely to occur on different products in-service then the corrosion severity data taken from the accelerated tests need to have a consistent relationship with such data for outdoor exposure or in-service testing. Pearson's product moment correlation coefficient is a measure of the linear correlation between two sets of data. Negative 1 indicates a perfect inverse correlation, 0 indicates no correlation and positive 1 indicates a perfect positive relationship. Table 3.2 shows a complete set of correlation values for all combinations of the accelerated and outdoor corrosion tests. The correlation values have been updated for the 0.5 Molar, 48 hour variant of the AAA test as this was the test selected to apply to the full set of 37 samples. The correlations for this variant of the AAA test can be considered the most significant because the sets of data being compared are much larger.

		Accelerated Applied Acid Test						Cyclic Cabinet	Lockheed	Outdoor	
		2 Molar HCl		1 Molar HCl		0.5 Molar HCl				3 year	5 year
		48h	600h	48h	600h	48h	600h				
Accelerated Applied Acid Test	2 Molar	48h	0.70	0.64	0.87	0.75	0.76	0.81	0.67	0.61	0.63
		600h		0.65	0.98	0.31	0.87	0.49	0.35	-0.01	0.00
	1 Molar	48h			0.80	0.59	0.60	0.49	0.64	0.19	0.27
		600h				0.70	0.87	0.77	0.60	0.35	0.35
	0.5 Molar	48h					0.66	0.52	0.64	0.63	0.58
		600h						0.83	0.62	0.68	0.68
Cyclic Cabinet								0.56	0.55	0.55	
Lockheed									0.48	0.53	
Outdoor	3 yr									0.91	
	5 yr										

Table 3.2 Pearson's product moment correlation coefficients for all combinations of accelerated and outdoor test data

The additional data for the 0.5 Molar HCl, 48 hour accelerated applied acid test results in the correlation for this test against the outdoor test decreasing from 0.84 and 0.83 for the 3 year and 5 year durations respectively to $r=0.63$ and $r=0.58$. These correlations still exceed those for both the cyclic cabinet ($r=0.55, 0.55$) and Lockheed tests ($r=0.48, 0.53$). On the face of it the 'best test' is now the 0.5 Molar HCl, 600 hour Accelerated Applied Acid Test but this of course is based on less data and so the correlation has lower statistical significance associated with it. The 2 Molar HCl, 48 hour variant also gives good correlation values (0.61, 0.63) but this is also based on limited data. More extensive testing of these two methods may be worthwhile. The effect of the quantity of data is reflected in the significance levels which are shown in **Table 3.3** below.

		No. of samples	Correlation, r	Significance, P
AAA 0.5M 48hr	vs Outdoor 3yr	37	0.63	0.00003
	vs Outdoor 5yr	37	0.58	0.00017
AAA 0.5M 600hr	vs Outdoor 3yr	10	0.68	0.03050
	vs Outdoor 5yr	10	0.68	0.03050
AAA 2M 48hr	vs Outdoor 3yr	15	0.61	0.01575
	vs Outdoor 5yr	15	0.63	0.01183
Cyclic	vs Outdoor 3yr	37	0.55	0.00042
	vs Outdoor 5yr	37	0.55	0.00042
Lockheed	vs Outdoor 3yr	37	0.48	0.00264
	vs Outdoor 5yr	37	0.53	0.00264

Table 3.3 Statistical significance, P, for correlations against 5 year outdoor data for the three most successful AAA test variants, the cyclic TNO cabinet test and the standard Lockheed test.

The AAA test (0.5M 48hr variant) correlates much better with the Lockheed test ($r=0.64$) than the cyclic cabinet test ($r=0.52$). This is likely to result from the fact that the AAA test is based on the Lockheed test method in that they are performed in similar temperature and humidity conditions. Both tests are designed to test

filiform corrosion performance. In contrast, the cyclic cabinet test includes long phases in its cycle at much lower and much higher temperatures (30°C to 60°C) and at much lower and much higher humidity levels (50 % to 96 %). This test is designed to also evaluate the samples on their resistance to forms of corrosion other than FFC.

The effect of Molarity of HCl on the performance of the Accelerated Applied Acid Tests for the 600 hours variants is that performance increases with decreasing Molarity. The correlations are 0.00, 0.35 and 0.68 between the 5 year outdoor data and the 2 Molar, 1 Molar and 0.5 Molar concentrations respectively. This trend is not observed for the 48 hour tests where the 0.5 Molar and 2 Molar concentrations both give significantly better results than the 1 Molar.

The TNO institute compared their results from their cyclic cabinet test, from Lockheed tests and from salt fog tests to outdoor field tests at a number of sites in the Netherlands. They found that the correlation between the outdoor field tests at different sites was about 0.85. The cyclic cabinet and Lockheed tests gave correlations of around 0.80 [122]. These high levels of correlation were not achieved by the cyclic cabinet and Lockheed tests used in this study.

3.3.2.3 Spearman's Rank

Another method of evaluating the accelerated corrosion test methods is to measure their ability to rank the corrosion resistance of the samples in terms of their predicted outdoor performance. A test which was successful under these criteria would be useful where the magnitude of the difference between samples is irrelevant. For example, if you needed to select the best product from a range of options.

The Spearman's rank values are calculated by ordering the samples by their corrosion susceptibility measurement values and then numbering them accordingly (ties are given the same ranking number). Pearson's correlation coefficients

(Equation 3.1) are then calculated using these ranking numbers instead of the raw data sets.

The Spearman's rank correlation values for all combinations of accelerated laboratory and outdoor corrosion tests are shown in Table 3.4. When the ranks are compared, the correlation between 0.5 Molar HCl 48 hours Accelerated Applied Acid Test and the outdoor test was further reduced (to 0.46 and 0.45 against the 3 year and 5 year outdoor data respectively) and the accelerated test was shown to be performing less well, in this respect, than the cyclic cabinet test (0.59 against each outdoor test). The 2 Molar HCl 48 hour (0.59, 0.61) and the 0.5 Molar HCl 600 hour tests (0.59 against both tests) were shown to be performing relatively well in terms of rank.

		Accelerated Applied Acid Test						Cyclic Cabinet	Lockheed	Outdoor	
		2 Molar HCl		1 Molar HCl		0.5 Molar HCl				3 year	5 year
		48h	600h	48h	600h	48h	600h				
Accelerated Applied Acid Test	2 Molar	48h	0.73	0.48	0.77	0.53	0.73	0.78	0.51	0.59	0.61
		600h		0.70	0.89	0.51	0.92	0.57	0.55	0.16	0.25
	1 Molar	48h			0.67	0.51	0.63	0.42	0.58	0.23	0.31
		600h				0.40	0.92	0.77	0.45	0.46	0.46
	0.5 Molar	48h					0.54	0.46	0.58	0.46	0.45
		600h						0.77	0.52	0.59	0.59
Cyclic Cabinet								0.52	0.47	0.54	
Lockheed									0.36	0.44	
Outdoor	3 yr									0.89	
	5 yr										

Table 3.4 Spearman's rank values for all combinations of accelerated and outdoor test data

3.3.2.4 Threshold of Acceptable Corrosion

Sometimes products are considered to have failed if, after a specific amount of time in service, they have corroded beyond a certain limit and to have passed if they have not corroded, or their degree of corrosion is within this limit or threshold. This would be the case where the product needs to meet certain corrosion resistance specifications. In this situation an accelerated corrosion test is required which can successfully identify the products which are likely to fail, and those which are likely to succeed in fulfilling these specifications.

Here, the data for each corrosion test has been standardised so that the total corrosion severity for each test equals 100. The standardised corrosion severity value for the 10th most susceptible of the 5 year outdoor exposure tested sample (2.6) is taken to be the threshold value. This means that 10 of the outdoor exposure tested samples have failed and the rest have passed. The percentage of samples which the accelerated corrosion tests correctly identify as either passing or failing according to the same threshold can then be taken to be a measure of the effectiveness of the test. These percentages are shown in Table 3.5 below.

Threshold	AAA	Cyclic cabinet	Lockheed	Outdoor 3 yr
Correct predictions / %				
Pass < 2.6 <= Fail	81	76	65	89
Pass = 0 < Fail	43	68	41	95

Table 3.5 Percentage of correct predictions according to zero and 2.6 corrosion threshold levels for accelerated and 3 year outdoor corrosion tests.

By this method of evaluation the AAA test is the most successful of the laboratory tests, correctly predicting whether or not samples would fail in outdoor exposure testing 81% of the time. The reason the AAA test performed much better in this evaluation than the others is that many of the samples which were shown to be

completely corrosion resistant in the outdoor exposure testing corroded during the AAA test. Most of these errors are eliminated by this method of evaluation. This is because if the amount of corrosion is low enough the test is considered to have successfully predicted that the sample would 'pass' in outdoor testing.

If the threshold is set at zero, that is, no corrosion is acceptable, then the AAA test performs badly, making correct predictions only 43% of the time (Table 3.5). The reason for this is that in the AAA test initiation occurs in virtually all cases. In the outdoor exposure situation the conditions for initiation will not necessarily occur. The AAA test cannot predict the likelihood of initiation of FFC, only its rate of propagation.

Almost all of the samples tested using the AAA method corroded as they did in the similar Lockheed test. Figure 3.5 shows that the only accelerated corrosion test to cause corrosion to occur in a similar percentage of samples to that in 5 years of outdoor exposure testing was the cyclic cabinet test.

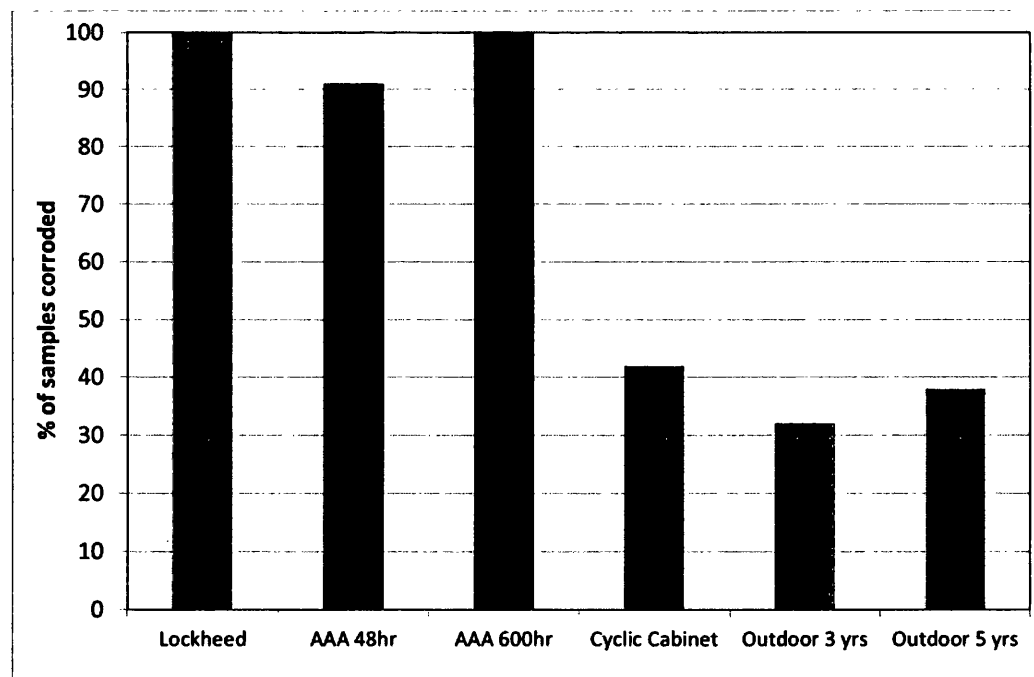


Figure 3.5 The percentage of the samples tested which corroded for the standard Lockheed, the accelerated applied acid test (0.5 Molar HCl - 48 hour and 600 hour test variants), the cyclic TNO cabinet test and the 3 and 5 year outdoor tests.

Leth-Olsen [43] used a modified Lockheed-type FFC test and this resulted in corrosion of some substrates which did not corrode in outdoor testing. The initiation method used in this study was to dip the samples in an aluminium chloride solution. It was suggested that the corrosion of these otherwise resistant samples may have been as a result of the accelerated test creating the aggressive conditions necessary for successive pitting FFC. It is possible that the samples in the present study which corroded a small amount in the AAA test but were completely resistant in the outdoor exposure test had become susceptible to successive pitting FFC as a result of the aggressive HCl initiation procedure. This would explain the discrepancy in the percentage of samples corroded shown in figure **Figure 3.5**. Further reducing the concentration of the HCl applied to the defects might prevent successive pitting from occurring on these samples and improve the ability of the AAA test to predict in-service behaviour of samples.

3.3.2.5 Standardised Corrosion Test Results

The results of the 5 year outdoor exposure test on all 37 samples are shown in Figure 3.6 along with the results of the AAA, Lockheed and cyclic cabinet accelerated tests. The data is sorted in descending order of the severity of corrosion in the outdoor test. Each set of data was standardised to total 100. Nine out of the 10 worst performing samples in the 5 year outdoor exposure test (31, 32, 35, 23, 1, 20, 29, 12, 28) developed a relatively large amount of corrosion during the AAA test. Sample 21, which was shown to be the 4th most susceptible by the outdoor exposure test, did not corrode very much in the AAA test and so this could be seen as a sign of a poor correlation between these two tests. The reverse occurred for samples 10, 14 and 24; these samples were shown to be relatively susceptible by the applied acid test but relatively resistant by the outdoor exposure test. This difference was particularly significant in the case of samples 14 and 24 because no corrosion occurred on these samples in the outdoor exposure test. Three of these four very 'wrong' AAA test results appeared to be backed up by the results of at least one of the other accelerated tests.

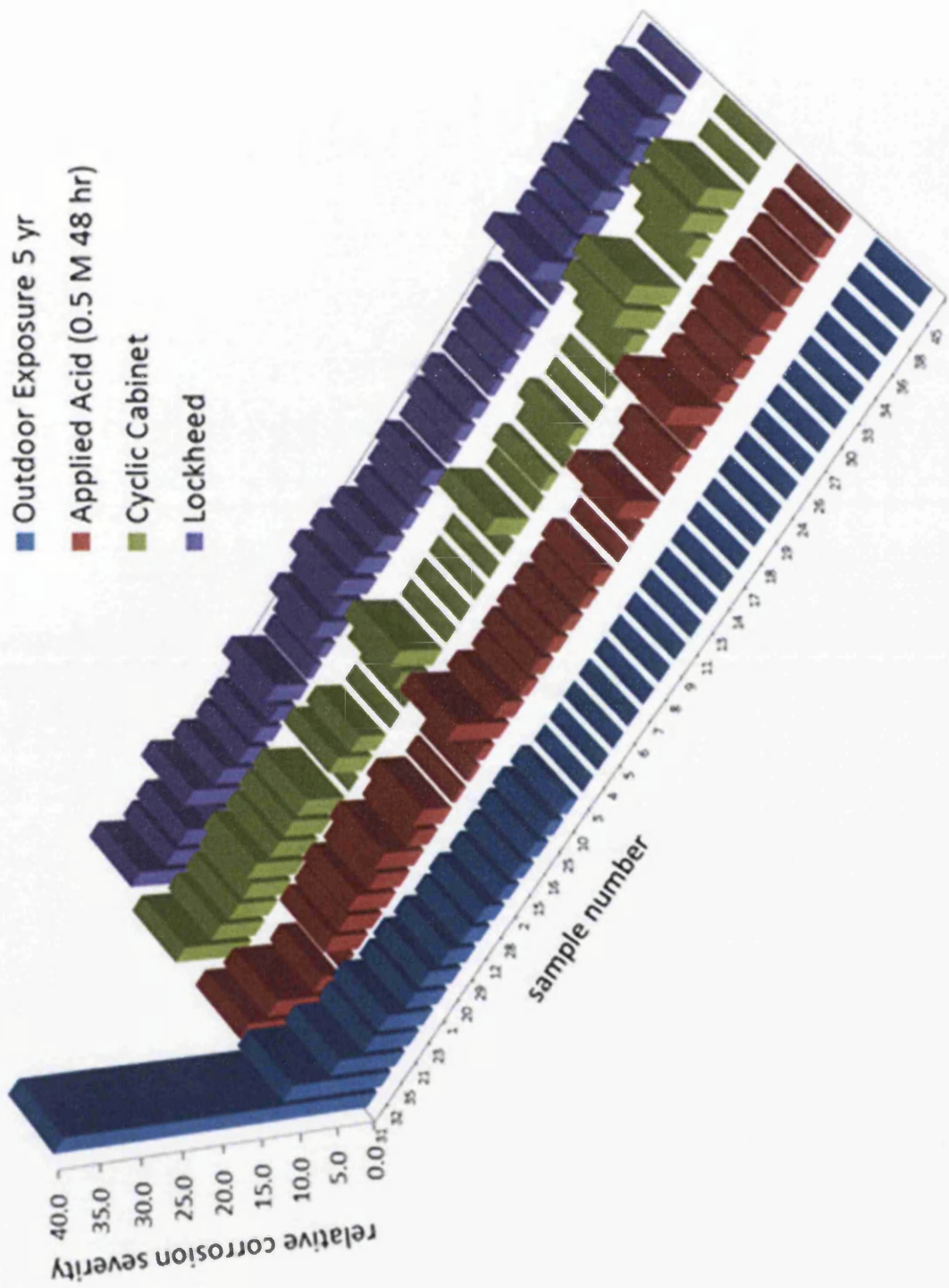


Figure 3.6 Standardised corrosion severity results for 37 coated architectural aluminium samples after outdoor exposure, an accelerated applied acid (AAA) test, a cyclic TNO cabinet test and the standard Lockheed test.

3.3.2.6 Level of Corrosion Acceleration

The measures which are taken to accelerate the corrosion during laboratory corrosion tests can prevent them from accurately predicting the outdoor corrosion behaviour. It has been suggested [123] that gross variations of accelerating factors can alter the kinetics of several intermediate corrosion reactions leading to spurious results. The TNO Institute [122] found that the Lockheed method of corrosion initiation by means of hydrochloric acid can be too aggressive for some types of aluminium. The poor results achieved by the 2 Molar HCl, 600 hour test, combining the most aggressive acid and the longer exposure time, could be explained on this basis.

An estimation of the acceleration factor for each of the accelerated corrosion tests was determined by calculating the FFC filament length in mm per mm of defect per 24 hours and comparing these values to the equivalent rate for the outdoor exposure tested samples. The corrosion rates for the cyclic cabinet and Lockheed sets of samples were an order of magnitude higher than the outdoor exposure rate. Outdoor exposure data was provided for 1, 2, 3, and 5 years and from this the total corrosion rate of the complete set of samples can be plotted. **Figure 3.7** shows that the rate is approximately constant over the 5 year test period. The rate for the AAA test was 2 orders of magnitude higher than the cyclic cabinet and Lockheed corrosion rate. This extreme acceleration of the corrosion can be seen as an advantage in terms of the speed with which samples can be evaluated but it is also likely to be the cause of many of the shortcomings of this test method and a much less aggressive version of the AAA might be more successful.

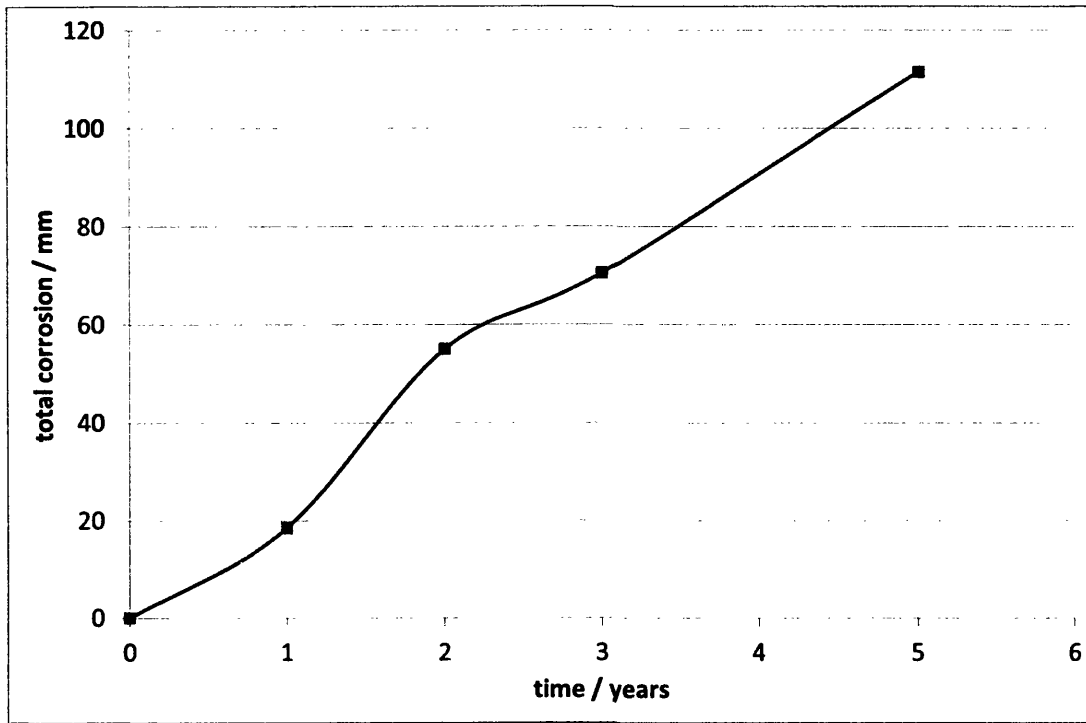


Figure 3.7 Total corrosion as a function of time for the set of 37 outdoor exposure tested architectural aluminium samples

3.4 Conclusions

The AAA test predicted outdoor test performance reasonably well in terms of direct correlation of corrosion data (with a high level of statistical significance) but performed less well when evaluating its ability to predict the correct performance ranking of samples.

The AAA test fails to predict whether or not corrosion will be initiated in outdoor conditions. The reason for this is that the AAA test includes an initiation procedure which involves the application of hydrochloric acid to a penetrative coating defect. This means that the acidification of the electrolyte by a corrosion process, which would normally be necessary for FFC to occur in outdoor conditions is bypassed in the AAA test. In cases where FFC does occur in outdoor conditions the AAA test provides a good measure of propagation.

The comparison of photographs of the samples after AAA testing and after outdoor exposure for 5 years showed that generally the same type of corrosion was occurring, namely filiform corrosion. However, in a few cases the outdoor exposure samples also blistered.

The exposure time of only 48 hours is significantly faster than other accelerated tests developed for this purpose but there appears to be scope for improvement by increasing the duration while decreasing the aggressiveness of the test.

The AAA test is extremely low cost, requiring no specialist equipment.

Although the results of this work suggest that the 0.5 Molar HCl, 48 hour variant of the AAA test has the potential to be comparable to some standard accelerated test methods, further work is needed to refine the method with a view to achieving correlations with outdoor exposure in excess 0.8 for large quantities of data.

Chapter 4: Localised Corrosion of Aluminium

Alloy AA6111

4.1 Introduction

The scanning vibrating electrode technique (SVET) was used to map the dynamic evolution of localised anodic and cathodic current density associated with pitting corrosion and intergranular corrosion (IGC) activity on AA6111. One aim of this work is to establish whether or not SVET is a suitable method of quantifying the corrosion susceptibility of AA6111 in various tempers.

The AA6111 used in this study contained 0.77wt% copper and was obtained in the T4 solutionised and naturally aged temper. Coupons of the material were heated at 185°C for varying periods up to 56 hours to produce samples in the underaged, peak-aged and overaged conditions - as confirmed by hardness measurement. Post heat treatment samples were ground and polished. On immersion in dilute (1% w/w) neutral aqueous sodium chloride solution the SVET was used to map the dynamic evolution of localised anodic and cathodic currents associated with pitting and IGC corrosion activity.

Time-resolved current density data was recorded at 2500 points on the 10mm by 10mm scan area of each of the 10 heat treatment variants of AA6111. Area integration of the SVET data allowed an estimate of the instantaneous (localised) corrosion rate and its time dependence to be determined. Integration with respect to time gave the overall current and the use of Faraday's Law then allowed estimation of the total metal loss over the experimental period (24 hours).

The large quantity of data was processed by a number of methods to allow a detailed investigation of the kinetics and localisation of the pitting and intergranular corrosion on the material and the influence of the ageing on these factors.

AA6111 is an Al-Mg-Si-Cu alloy and as is the case for all AA6000 series alloys it undergoes a complex precipitation sequence when it is aged. There are numerous

possible intermediate phases depending on the amount of copper in the alloy and also the ratio of magnesium to silicon (as discussed in greater detail in the literature review). Initially clusters of silicon, magnesium or a combination of silicon and magnesium form, with further heating and diffusion these clusters develop into GP zones. At peak ageing β'' (Mg_2Si) is the dominant intermediate phase and this coexists with metastable versions of the Q phase ($Cu_2Mg_8Si_7Al_4$). When overaged the equilibrium incoherent Q phase forms [74]. The ageing condition of the samples was identified by means of hardness testing. Precipitation hardening occurs as a result of the changes in the size, spacing and coherence of the precipitates with heat treatment and is related to the ease with which dislocations can move through or around them.

The AA6000 series alloys are known to be relatively corrosion resistant but second phase precipitation can increase susceptibility to intergranular corrosion [16, 24-26]. In AA6111 aged at 180°C for between 0.5 and 11 hours there are two precipitating phases which coexist, monoclinic β'' and hexagonal Q [74]. Copper rich grain boundary precipitates are believed to act as local cathodes and couple microgalvanically with adjacent Cu and Si depleted zones increasing IGC susceptibility [16, 25, 26]. It has recently been demonstrated that in the under-aged condition produced by paint bake simulation, a nearly continuous Cu-enriched film forms along grain boundaries and IGC susceptibility is maximised. On further ageing this film breaks up producing discrete Q phase particles and IGC susceptibility is reduced [24, 61].

4.2 Experimental

4.2.1 Materials

AA6111 sheet of 1.1mm thickness was provided by Innoval in the solutionised (at 620°C) and naturally aged T4 temper (composition by weight Al, Mg 0.76%, Fe 0.24%, Si 0.64%, Cu 0.77%, Mn 0.20%). The AA6111 sheet had been hot and cold rolled and alkali cleaned on-line to remove any resulting deformed surface layer. As received AA6111-T4 was cut into 40mm by 40mm coupons and degreased using acetone. When not in use the coupons were stored at -18°C to prevent any unwanted natural ageing.

4.2.2 Heat Treatments

The samples were heated in air at 185°C for times up to 96 hours (0, 0.17, 0.28, 0.57, 1.38, 2.55, 5.56, 11.11, 25.00, 55.56, 96.00 hours) and naturally cooled in air at room temperature.

4.2.3 Grinding and Polishing

In order to provide a clean and uniform surface for SVET experiments and to remove any thick oxide that may have formed during heat treatment, all surfaces were ground and polished. Grinding was performed by hand using silicon carbide paper and then a polishing wheel with 1µm diamond paste.

4.2.4 Hardness Measurements

Vickers hardness measurements were carried out before and after heat treatment to measure the precipitation hardening effect and to identify the underaged, peak aged and overaged samples. All samples were hardness tested a third time, 1000 hours after they were heat treated, to confirm that the material had not aged further during storage. Each measurement was repeated and the stated value is the

mean of three measurements all taken using 1kg of force. The hardness of the samples used in the filiform corrosion work was also measured using this method. These samples had a different range of heat treatments applied to them but hardness measurements were used to indicate their degree of ageing. This allowed the ageing dependence of pitting corrosion to be directly compared with the previous results for the ageing dependence of filiform corrosion.

4.2.5 Scanning Vibrating Electrode Technique

The theoretical principles behind the scanning vibrating electrode technique (SVET) are discussed in the literature review. More practical aspects of its operation are described here with reference to Figure 4.1. The motor stage controls the movement of the SVET head in the x, y and z directions. The motors move in steps of a minimum size of 2.5 μm . The motor stage is controlled by the computer. The audio amplifier provides the probe vibration signal input to the SVET head. The data signal travels from the SVET tip to the lockin where it is processed before being sent to the computer.

4.2.5.1 Construction

Detail of the SVET probe and head assembly is shown in Figure 4.2. A reference electrode is attached to the body of the head and is in contact with the electrolyte throughout the test. The top section of the probe consists of a mu-metal box containing a small loudspeaker. A glass push rod is attached to the cone of the speaker and is attached to the SVET tip by a Teflon holder. The platinum wire from the tip exits from the Teflon holder and is soldered onto the signal wire. The diameter of the wire is 125 μm .

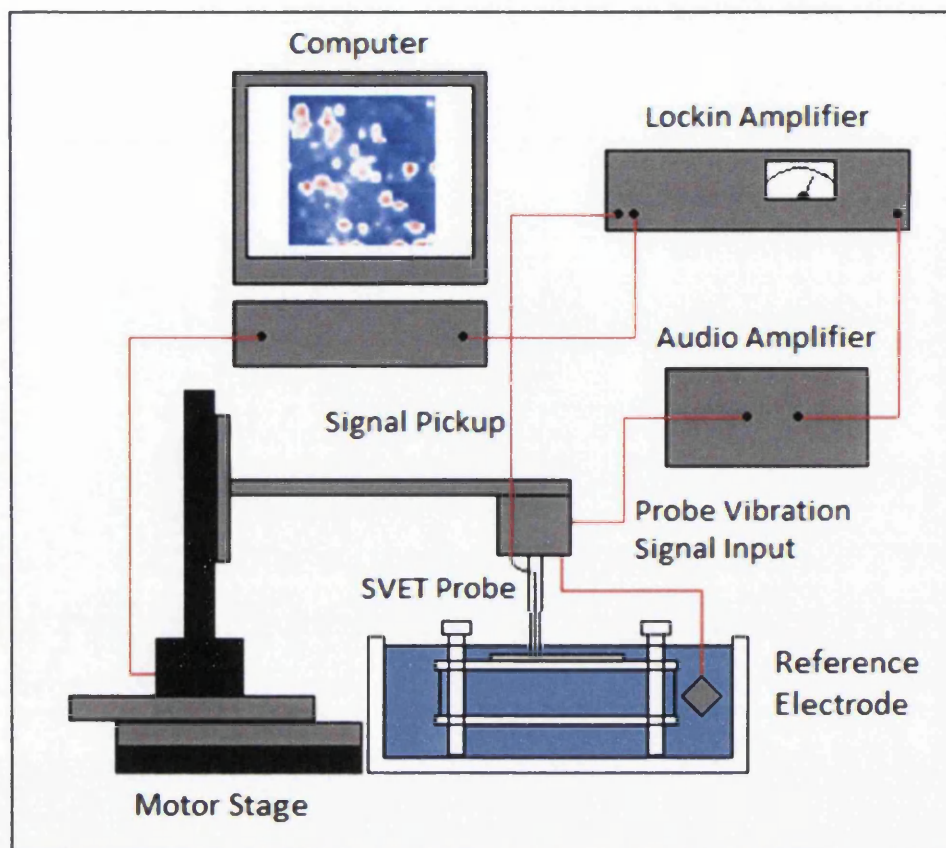


Figure 4.1 Schematic representation of the SVET equipment.

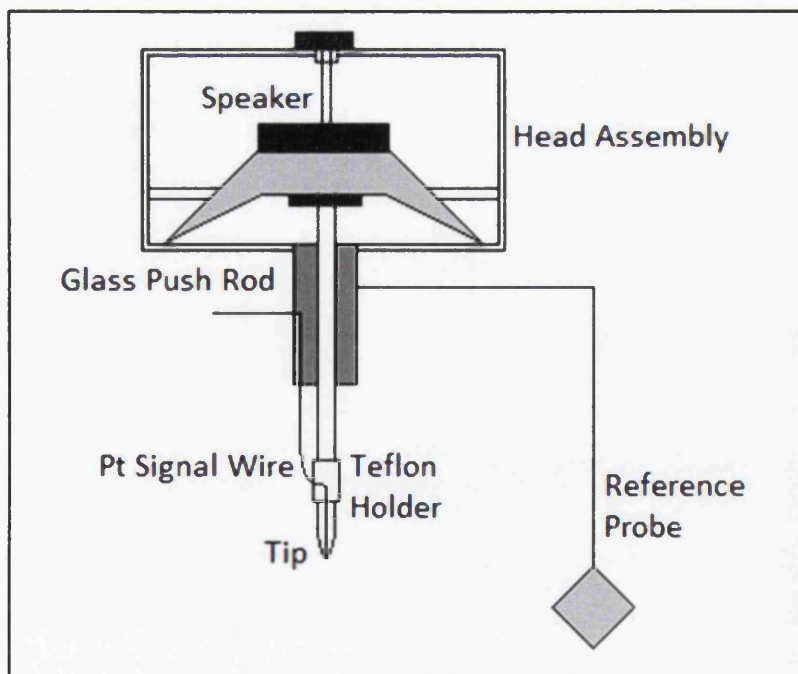


Figure 4.2 Schematic representation of the SVET probe and head assembly.

4.2.5.2 Calibration

The SVET equipment must be calibrated to allow measured voltage data to be represented in terms of current density. This is done by comparison with controlled applied current densities using a 'teapot' calibration cell (Figure 4.3). The electrodes are connected to a galvanostat; a positive electrode is placed in the 'spout' of the 'teapot' cell and the negative electrode is placed in the bulk electrolyte thus creating a circuit of ionic current flow. The electrolyte in the 'teapot' calibration cell is separated from the bulk electrolyte other than through the 'spout', which has a known cross sectional area. This allows the current density to be controlled in the vicinity of the probe tip. The SVET tip is vibrated in this controlled current density and the voltage response recorded. The SVET must be set in phase so that anodes are recorded as positive and cathodes as negative voltages. A range of currents are applied by the galvanostat and corresponding voltages are recorded from the lockin amplifier. When zero current is reached the corresponding voltage is again recorded and then the electrode connections on the galvanostat are switched so that the positive electrode is in the bulk electrolyte and the negative electrode is in the 'teapot' cell. The calibration process is then repeated to ensure that there is no constant residual signal that may affect the results. Values of current density (Am^{-2}) are plotted against voltage so that the calibration factor is given by the gradient of the line. The calibration factor was measured regularly and was found to vary by no more than $\pm 6\%$.

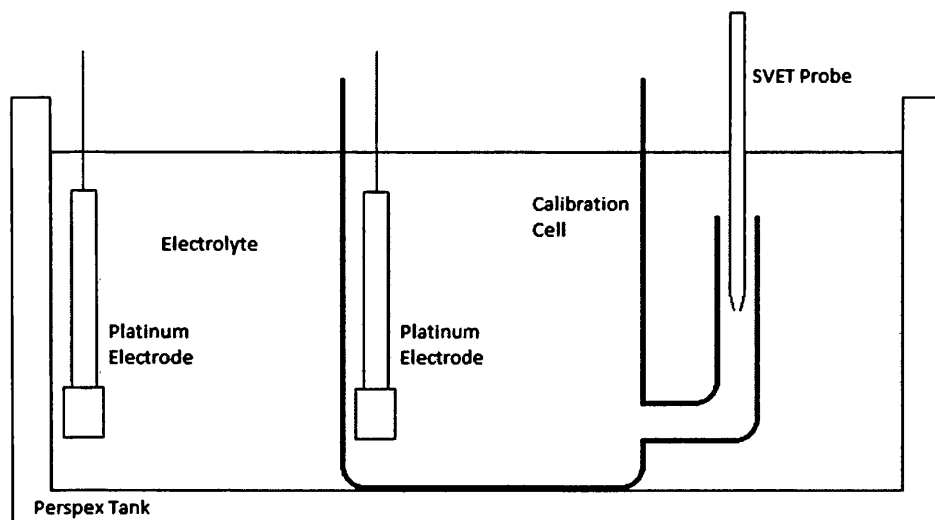


Figure 4.3 Diagram showing SVET calibration apparatus.

4.2.6 SVET Experiments

The SVET probe was set to vibrate at a frequency of 140Hz with a peak to peak vibration amplitude of $30 \pm 5 \mu\text{m}$. The probe was scanned $100 \mu\text{m}$ above the sample. Scans over the 10mm by 10mm area were carried out every 30 minutes for 24 hours. In these experiments the step size was set at 0.2mm to give a good balance between the number of data points and the time for each scan

Teflon tape was used to mask off all but a 10mm by 10mm square on the polished side of each sample. Samples were then attached to a Perspex stage and immersed in an electrolyte of 1% w/w sodium chloride in distilled water. The SVET was used to determine current density distributions as a function of time over the surface of the samples. This method made it possible to study the kinetics of propagation of stable pits. The SVET takes approximately 20 minutes to carry out a complete scan of the 1cm^2 exposed scan area and consequently metastable pits are unlikely to be detected.

4.2.7 SVET Current Flux Detection

The appearance of the samples after the corrosion experiment (Figure 4.6) and the corresponding current density maps (Figure 4.7) suggest that pitting corrosion occurred. The anode-cathode distances appear to be significantly greater than the probe height which was 100 μm . Consequently it is expected that the current flux between these anodes and cathodes will be detected by the SVET probe as shown in Figure 4.4(a) [124]. Any current flux arising from microgalvanic couples with an anode to cathode distance less than the probe height would not be detected as shown in Figure 4.4(b).

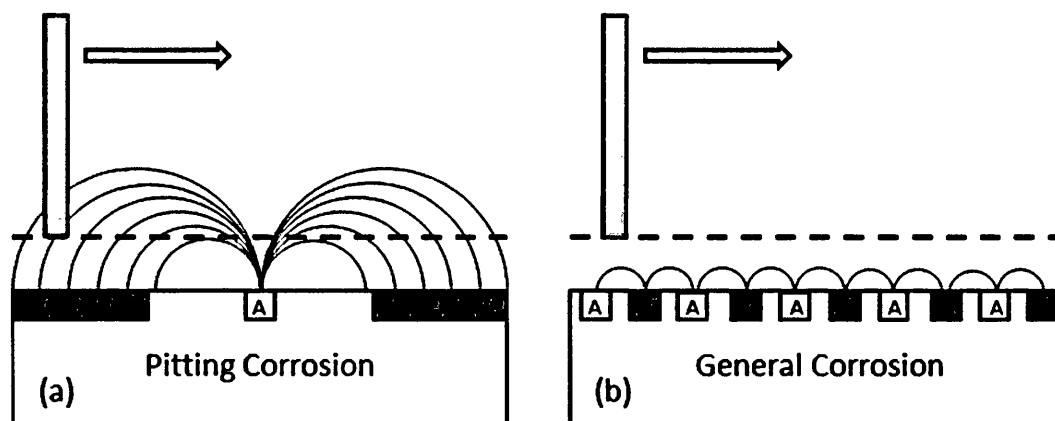


Figure 4.4 Schematic diagram showing SVET current flux detection in the case of (a) an anode to cathode distance which is greater than the probe height and (b) an anode to cathode distance which is less than the probe height.

4.2.8 Total Equivalent Aluminium Loss Calculation

The SVET output consisted of current density distributions for each half-hourly scan. The total time dependent current, I_{anodic} is obtained by numerical integration of the area-averaged anodic current densities (j_z) over the scan area:

Equation 4.1

$$I_{anodic} = \int_0^y \int_0^x [j_{z(x,y)} > 0] dx dy$$

Here x and y are the SVET scan area dimensions.

The charge is given by:

Equation 4.2

$$Q = \int_0^{1800} \frac{I_a}{A} dt$$

where Q is the charge in Cm^{-2} and A is the scan area in m^2 .

The total equivalent aluminium loss is given by:

$$L = \frac{26.98Q}{3F}$$

where L is the total equivalent aluminium loss in gm^{-2} and F is the Faraday constant (96485 Amps per mole).

The corrosion currents and consequently the calculated total equivalent aluminium loss derived from the SVET data will be underestimates as explained in section 4.2.7.

4.3 Results and discussion

4.3.1 SVET Output Analysis

It was apparent that, for most scans, the total cathodic current was significantly greater than the total anodic current. An adjustment was made to each measurement to balance the total cathodic and anodic currents. Figure 4.5 shows the result of applying the appropriate adjustment to each scan of AA6111 in the T4 (0h @ 185°C), underaged (0.57h @ 185°C), peak aged (5.56h @ 185°C) and overaged (55.56h @ 185°C) conditions. It can be seen from Figure 4.5 that the average anodic current density values are more reliable than the cathodic ones and this supports the choice of the anodic values for quantitative analysis in this study. The adjustment needed for each measurement was of the order of 0.001 Am^{-2} to 0.01 Am^{-2} for the T4 sample and 0.01 Am^{-2} to 0.06 Am^{-2} for the other samples.

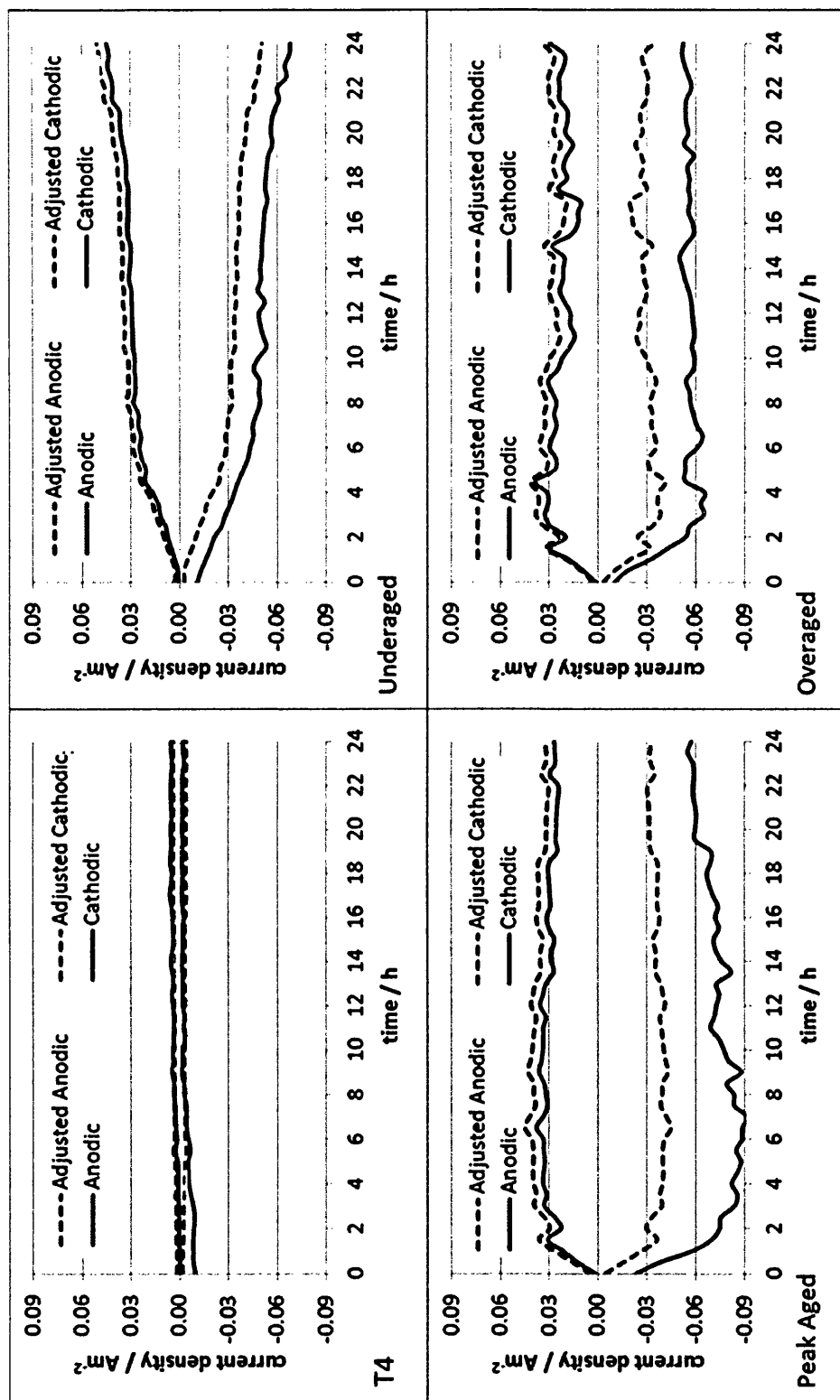


Figure 4.5 Area averaged SVET current density plotted against time for AA6111 in the T4 (0h @ 185°C), underaged (0.57h @ 185°C), peak aged (5.56h @ 185°C) and overaged (55.56h @ 185°C) conditions; the graphs also show values of average current density which have been adjusted to balance anodic and cathodic current.

4.3.2 Hardness

Hardness measurements showed that the initial hardness of the AA6111 used in the study in the solutionised and naturally aged T4 temper is 83HV1 and that heat treatment of the material at 185°C increases hardness for times up to 5.56 hours when a peak hardness of 121HV1 was obtained. Longer heat treatments at this temperature cause the material to become overaged and hardness gradually and steadily falls in the period up to 96 hours - the longest heat treatment time tested. The complete age hardening curve is shown in Figure 4.12.

4.3.3 Corrosion Morphology

Spots and rings of corrosion product with a range of sizes and shapes gradually appeared on all samples; the appearance of the attack was consistent with pitting corrosion. Figure 4.6 is a group of photographs of samples in the T4 (0h at 185°C), underaged (0.57 hours at 185°C), peak aged (5.56 hours at 185°C) and overaged (55.56 hours at 185°C) tempers after 24 hours of immersion in the electrolyte. On looking at these and the other corroded samples, it was not apparent that there was any systematic change in their appearance as a result of the degree of ageing.

SVET current density maps in Figure 4.7 indicate that the spots and rings of corrosion product were formed in regions of localised anodic activity. There is a clear correspondence between these regions of anodic activity and the pattern of corrosion products seen on the samples after immersion. Comparing the photographs with the SVET current density maps also shows that the larger and more irregularly shaped areas of corrosion product are the result of multiple anodes in that area. The current density maps also show that the majority of the surface exposed to the electrolyte acted as a cathode with a relatively homogeneous current density. The photographs in Figure 4.6 show that the areas which are cathodic in the final SVET maps (Figure 4.7) are almost completely free of corrosion product.

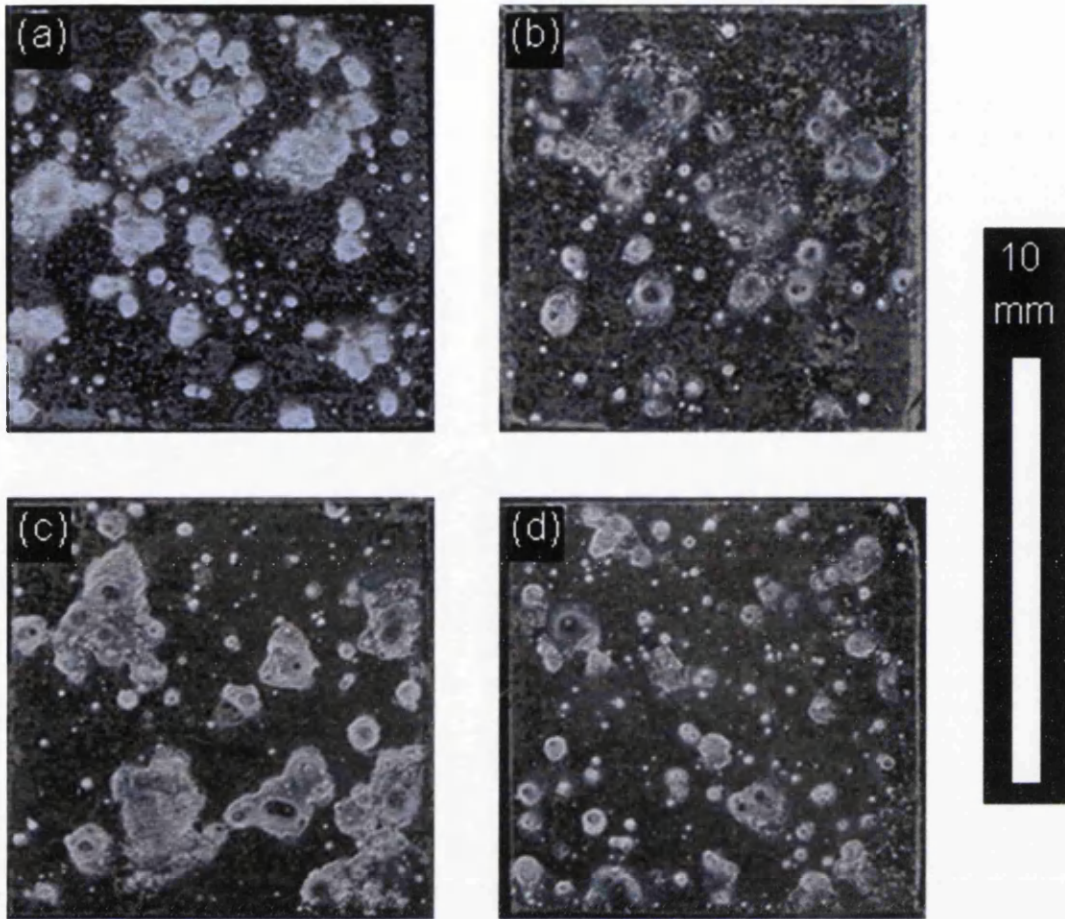


Figure 4.6 Photographs of 10mm by 10mm exposed area of samples in the T4 (0h @ 185°C), underaged (0.57h @ 185°C), peak aged (5.56h @ 185°C) and overaged (55.56h @ 185°C) conditions after 24h immersion in 1% w/w aqueous NaCl solution.

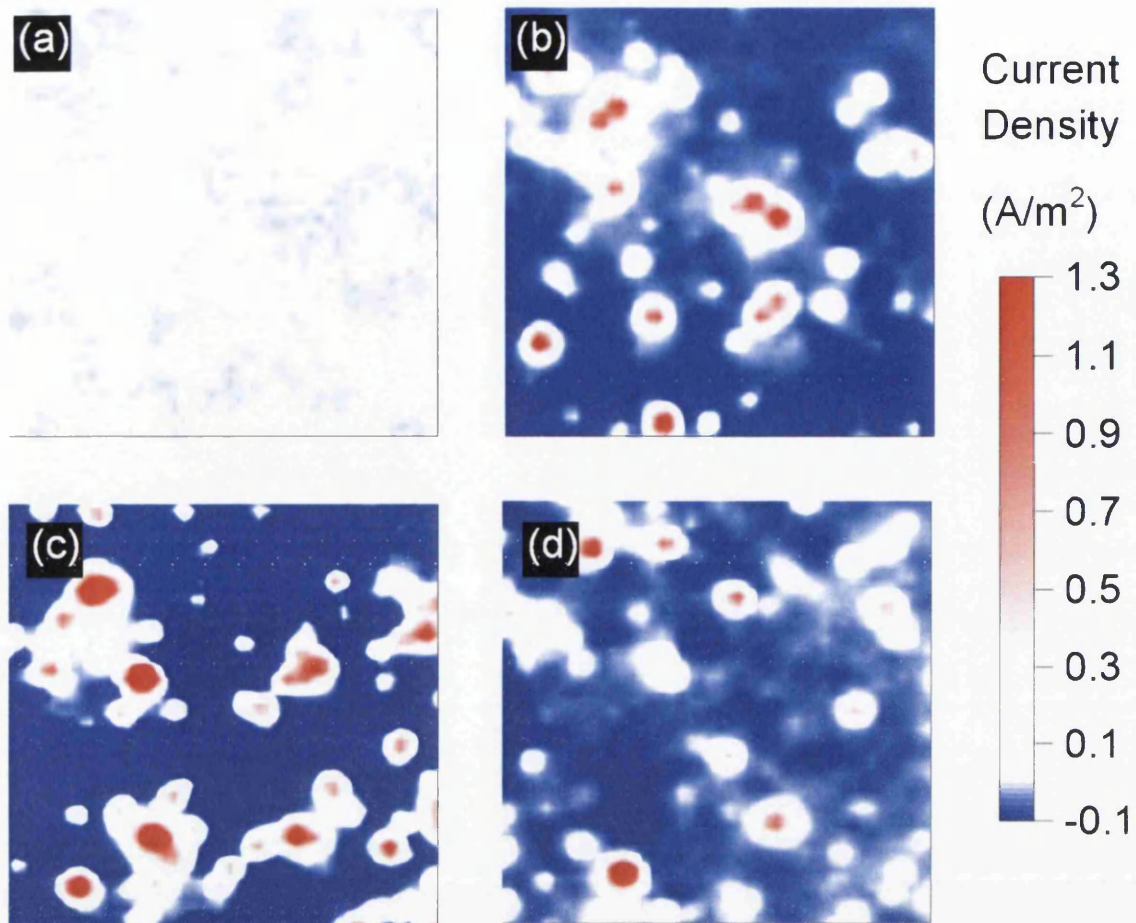


Figure 4.7 SVET current density maps of 10mm by 10mm exposed area of samples in the T4 (0h @ 185°C), underaged (0.57h @ 185°C), peak aged (5.56h @ 185°C) and overaged (55.56h @ 185°C) conditions after 24h immersion in 1% w/w aqueous NaCl solution.

4.3.4 Corrosion Kinetics

Figure 4.8 shows SVET maps of current density across 1cm^2 scan areas on AA6111 in the T4, underaged, peak aged and overaged conditions after 1, 6, 12 and 24 hours immersion in the electrolyte. The current density maps for all samples show that, throughout the experiment, anodic activity is highly localised with the rest of the area acting as the cathode with a relatively consistent current density. The initial SVET scans for each sample show that some local anodic activity takes place within the first 30 minutes indicating that localised corrosion occurs soon after immersion in the electrolyte.

It can be seen that very little activity develops on the T4 sample. After 1 hour there are a few anodes with very low current density; by 6 hours the number of anodes and their intensity has increased; longer immersion results in slight increases in intensity but the number of anodes (20 to 30) is fairly constant between 6 and 24 hours. None of the anodes reaches a current density of more than 0.3 Am^{-2} .

The underaged sample has a small number of anodes of low current density after 1 hour of immersion. By 6 hours there are approximately 30 significant anodes with current density values up to 2 Am^{-2} . The number and intensity of these anodes remained similar for the rest of the test.

For the peak aged sample considerably more activity took place in the first hour both in terms of the number of anodes and their intensity. Throughout the latter part of the test a small number of high current density anodes seemed to dominate. The total number of anodes was smaller than for the underaged sample. The maximum current density value recorded was in excess of 7 Am^{-2} .

There was also significant early activity in the overaged sample. After 6 hours the number of anodes had increased to between 30 and 40 and the number remained at this level for the rest of the test. A number of strong anodes appeared throughout the test but did not maintain these high current densities. The highest current density achieved at an anode was approximately 6.5 Am^{-2} for this sample.

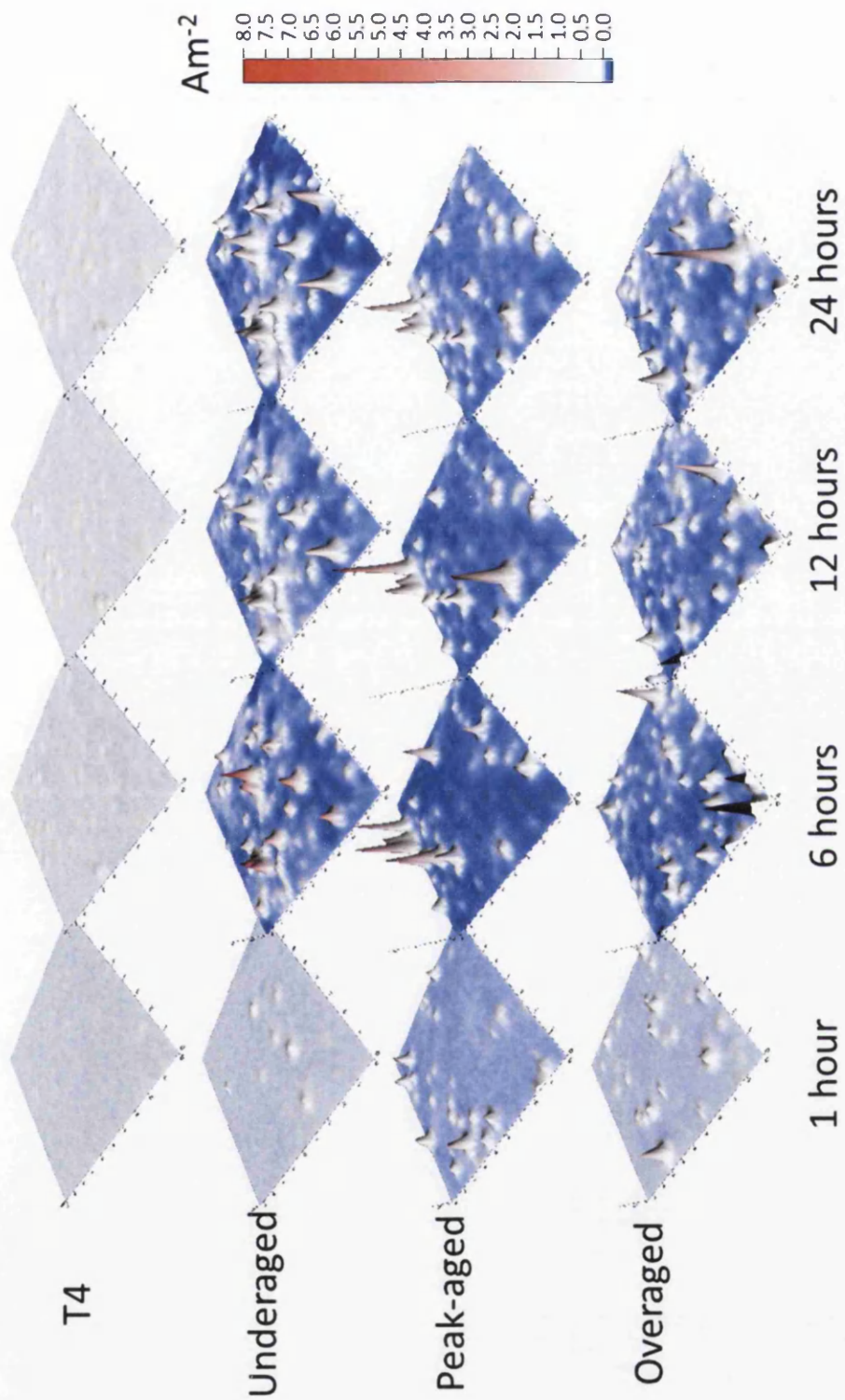


Figure 4.8 SVET maps showing current density across 1cm^2 scan areas on AA6111 in the T4 (0h @ 185°C), underaged (0.57h @ 185°C), peak aged (5.56h @ 185°C) and overaged (55.56h @ 185°C) conditions after 1, 6, 12 and 24 hours immersion in 1% w/w aqueous NaCl solution.

In order to more closely examine the behaviour of the dominant anodes, the maximum current density value, across time, for each sample was established for each point. These maximum current density values were then represented by a colour scale on a grid for each sample in Figure 4.9.

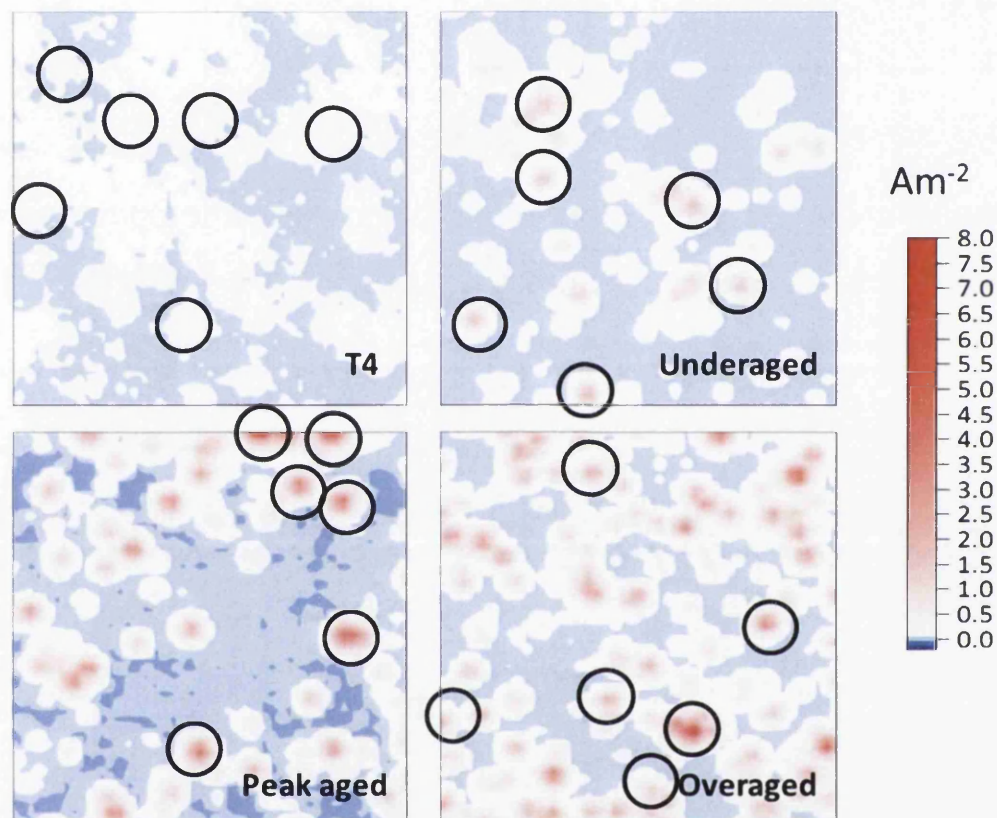


Figure 4.9 Maps showing maximum current density achieved during the test for AA6111 samples in the T4 (0h @ 185°C), underaged (0.57h @ 185°C), peak aged (5.56h @ 185°C) and overaged (55.56h @ 185°C) conditions resulting from 24 hours immersion 1% w/w aqueous sodium chloride solution. The circles mark the six highest maximum current densities achieved for each sample.

The maximum current density maps in Figure 4.9 are useful in showing the location and shape of anodes which have been active at any time during the 24 hours of immersion. Anodes are generally distributed in such a way that the distance between their centres and the nearest available cathodic area is less than 1mm. On the other hand there is a tendency for new anodes to develop in the vicinity of

previous anode sites. Figure 4.9 also shows that on each sample some of the surface remained cathodic throughout the test.

For each of the 10 samples the locations of the six highest maximum current densities achieved during the 24 hour experiment were identified. A graph of the current density at each of these locations was plotted against time. The graphs for four of the samples are shown in Figure 4.10.

For each sample, on average, the six 'maximum' anodes, between them, contribute 46% of the total anodic current. Their behaviour therefore accounts for a large proportion of the corrosion that occurs. The anodic activity is minimal for the T4 sample. The anodes in the five underaged samples follow a broadly similar pattern in that they generally reach their maxima within the first seven hours before the current density falls slightly and plateaus. From peak ageing onwards the maximum values of current density reached are higher and there is a tendency for them to be separated in time. This separation is particularly clear for the samples which had been aged for the longest (Figure 4.10 and Figure 4.11). For all except the T4 sample, once the maximum values have been reached the current densities generally decrease to significantly anodic values up to approximately 2Am^{-2} .

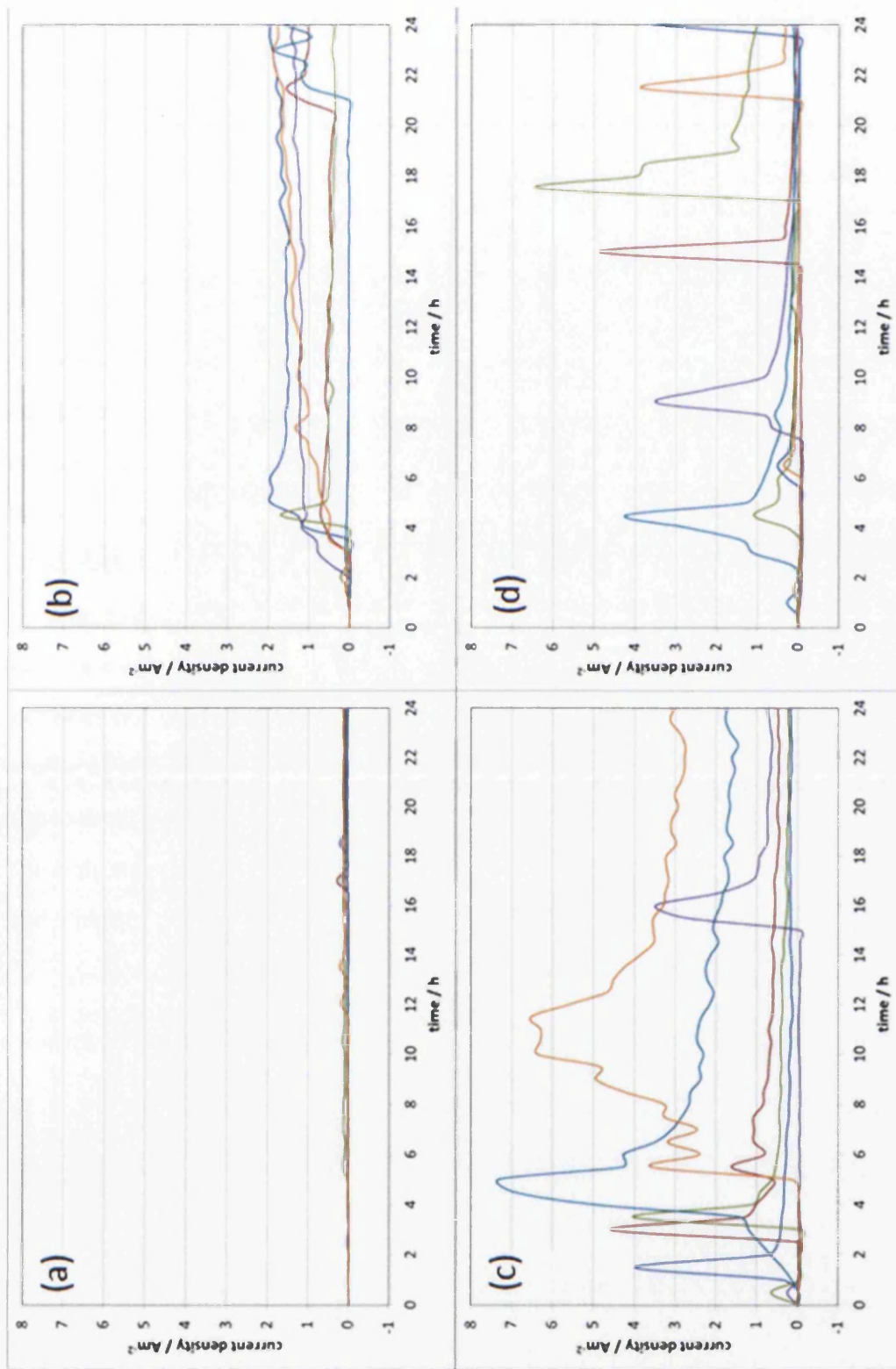


Figure 4.10 Evolution of current density values at the locations of the 6 highest maxima for each of the (a) T4 (0h @ 185°C), (b) underaged (0.57h @ 185°C), (c) peak aged (5.56h @ 185°C) and (d) overaged (55.56h @ 185°C) samples.

Anodic activity becomes established relatively quickly in all except the T4 sample. The area averaged anodic current density reaches near to its highest value within 6.5 hours in all artificially aged samples. In two of the samples a slightly higher average current density value is reached at the end of the experiment.

Figure 4.11 shows the time dependence of current density at the sites of the 6 highest maxima for one of the overaged samples (25 hours at 185°C). As mentioned previously the 'maximum' anodes for overaged samples have a tendency to spread out through time; the 6 peaks of current density do not overlap at all for this sample. Anodes appear to develop and recede in succession. Also shown in this figure are the colour scale SVET current density maps at the time that each of the peaks reaches its maximum value. The relevant anode is circled in each case. It can be seen that the third, fifth and sixth anodes form in very similar, but not identical, locations to one another. This supports the idea that new anodes preferentially locate in the vicinity of sites of previous intense anodic activity. The current density profile of the six anodes are very similar with a rapid increase in current density to approximately 5 Am^{-2} followed by a rapid fall and plateau at approximately 1 Am^{-2} . The only significantly different profile is for the fifth anode which has a double peak and a higher plateau current density value.

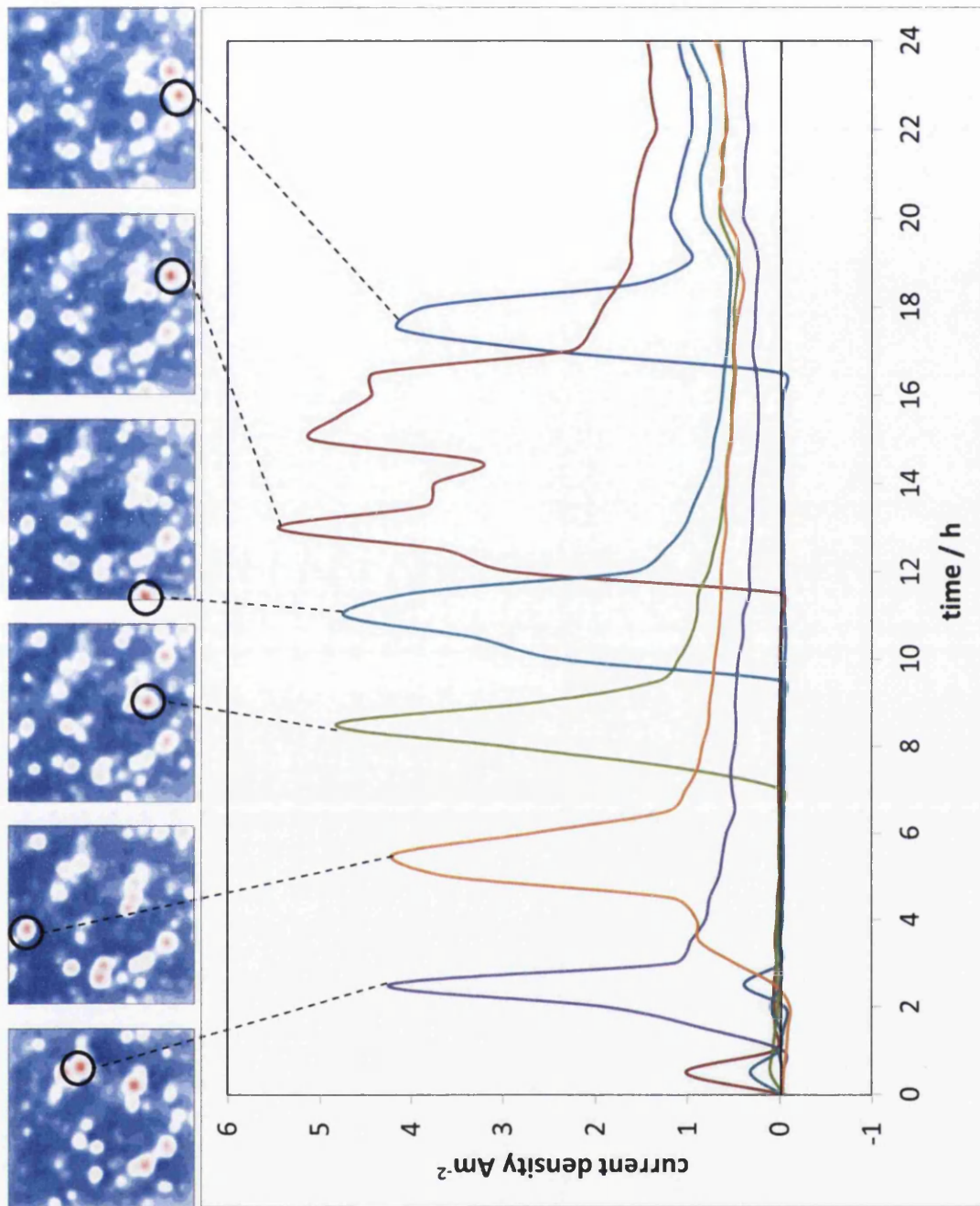


Figure 4.11 Current density histories for the six most intense anodes for overaged (25h @ 185°C) AA6111 matched with the corresponding SVET current maps.

4.3.5 Influence of ageing on susceptibility

The results reported in the 'Filiform Corrosion of AA6111' chapter show that the filiform corrosion susceptibility of the samples increases with hardness in the underaged condition but decreases when overaged. AA6111 samples for the FFC work were tested in the T4 condition, and after 2 hour heat treatments at a range of temperatures. Hardness measurements for these samples were 84HV1 in the T4 condition, 87HV1 at heat treatment at 100°C, 104HV1 after heat treatment at 180°C (underaged), and 50HV1 after heat treatment at 350°C (heavily overaged). Filiform corrosion susceptibility of these samples was previously shown to be at a minimum in the T4 condition and then increase with heat treatment temperature up to 180°C (which has now been shown to be underaged). Susceptibility then decreased for the sample heat treated at 350°C, hardness measurement showed this sample to be more heavily overaged than any of the samples prepared for this SVET work. In order to test whether a similar corrosion susceptibility dependence on ageing exists for AA611 under immersion conditions a calculation of the mass loss was calculated from the SVET current density data for each of the 10 samples over the 24 hour experiment. Figure 4.12 shows calculated mass loss against heat treatment time (at 185°C). The hardness curve is also plotted on this graph. Heat treatment time is plotted on a log scale.

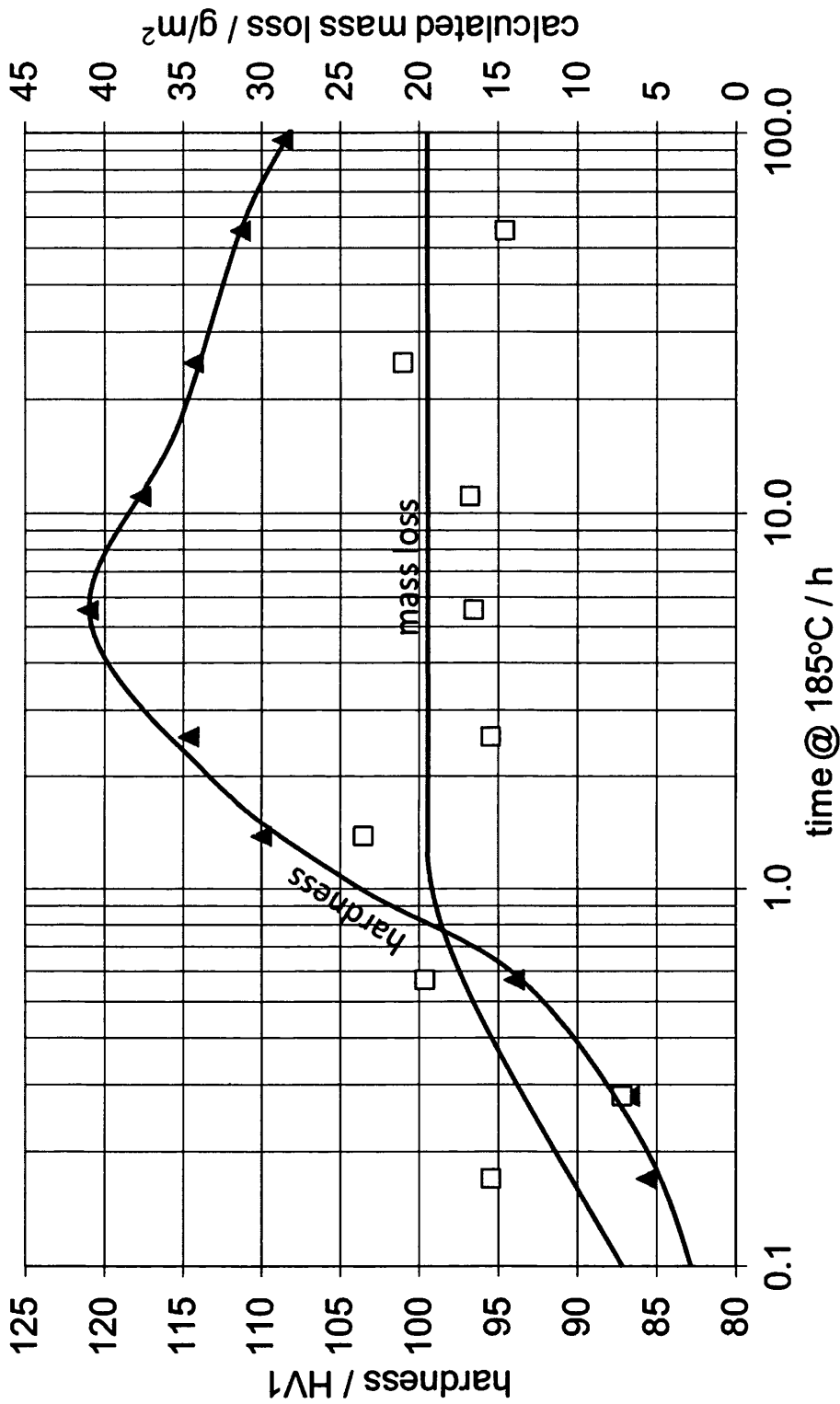


Figure 4.12 Calculated aluminium metal loss values against heat treatment time for AA6111 during immersion in aqueous 1% w/w sodium chloride solution for 24 hours.

The calculated mass loss value for the T4 sample was 3gm^{-2} , this is by far the lowest mass loss value for the set of samples. The heat treatment time was zero for the T4 sample and so it could not be plotted on the log scale. The maximum calculated mass loss value was 24gm^{-2} . There is a lot of scatter in the calculated mass loss values (shown by hollow markers) but the overall pattern suggests that corrosion susceptibility initially increases with ageing but is then relatively constant for ageing times over one hour.

The relationship between corrosion susceptibility and ageing appears to be similar in both atmospheric (filiform corrosion) and immersion conditions. In a previous study on AA6111 [24] the same heat treatment temperature (185°C) was used and samples were heat treated for a similar range of times as in this work. However the samples differed in that they were extruded at a sufficient temperature to solutionise them (die exit temperature: $575\text{-}580^{\circ}\text{C}$) and were then cooled in air. These samples were not, therefore, in the T4 condition prior to ageing heat treatment. The results of this work showed the material to be susceptible to IGC in the unaged condition and to become less susceptible with increasing heat treatment time until it was made effectively corrosion resistant at approximately peak hardness. Overageing was found to introduce pitting susceptibility. Comparing the results of this previous work with the results in Figure 4.12 suggests that the relationship between ageing time and corrosion susceptibility can be inverted as a result of a slow post-solutionising cooling rate. A number of other studies have found the IGC susceptibility of AA6000 series alloys to increase as a result of ageing and to reach a maximum when in the peak hardness (T6) condition [64-66, 69].

It is likely that the corrosion susceptibility of AA6111 in 1 wt% sodium chloride solution is determined by the cathodic process. In this case the cathodic reaction will be the reduction of oxygen. The AA6111 alloy used in this work contains 0.77 wt% copper and can form copper rich intermetallic particles which act as sites for the oxygen reduction on its surface. These copper rich cathodic particles would not be present when AA6111 is in the T4 condition and this would explain the low level of corrosion activity detected by the SVET for this sample. As the heat treatment time is increased, the alloy will precipitate copper rich particles which act as

discrete cathodes at the surface. The corrosion rate is controlled by the availability of cathodic sites so the corrosion rate increases as the copper rich particles become available at the surface. This explains the increase in the rate of corrosion as a result of heat treatments of up to an hour.

As the heat treatment time is increased further the rate of corrosion as measured by the SVET doesn't continue to increase. This can be explained on the basis of diffusion of oxygen through the Nernst diffusion layer. Once there is enough precipitation of cathodic intermetallic precipitates for the distance between exposed cathodes on the surface to be less than the thickness of the Nernst diffusion layer, the oxygen diffusion pathways are effectively the same length as if the surface was all cathodic. This means that further increases in precipitation of cathodic intermetallics as a result of longer heat treatments, which is likely to decrease the distance between available cathode sites on the surface, would not further increase the rate of corrosion. This explanation only holds true if there is a significant Nernst diffusion layer thickness. As the SVET experiments were carried out in an unstirred electrolyte it is likely that it is relatively thick and so this is a likely explanation for the relationship between heat treatment time and calculated mass loss shown in Figure 4.12.

4.3.6 Microscopy

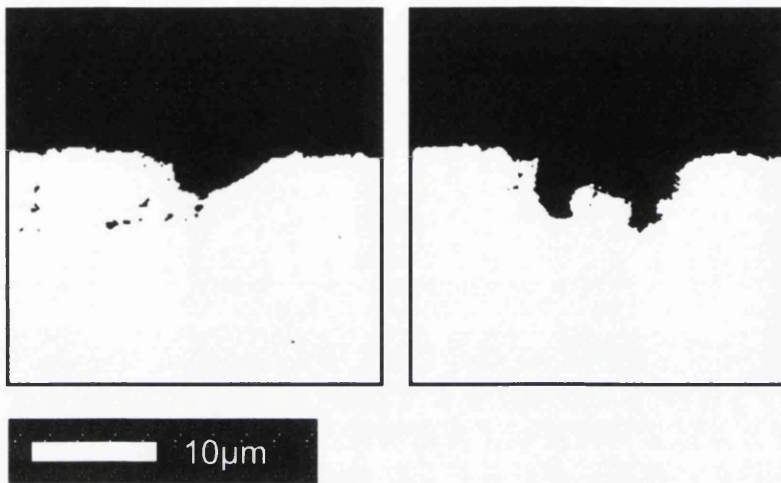


Figure 4.13 Cross sectional optical micrographs of AA6111 in the underaged (0.57h @ 185°C) condition after 24h immersion in 1% w/w aqueous NaCl solution.

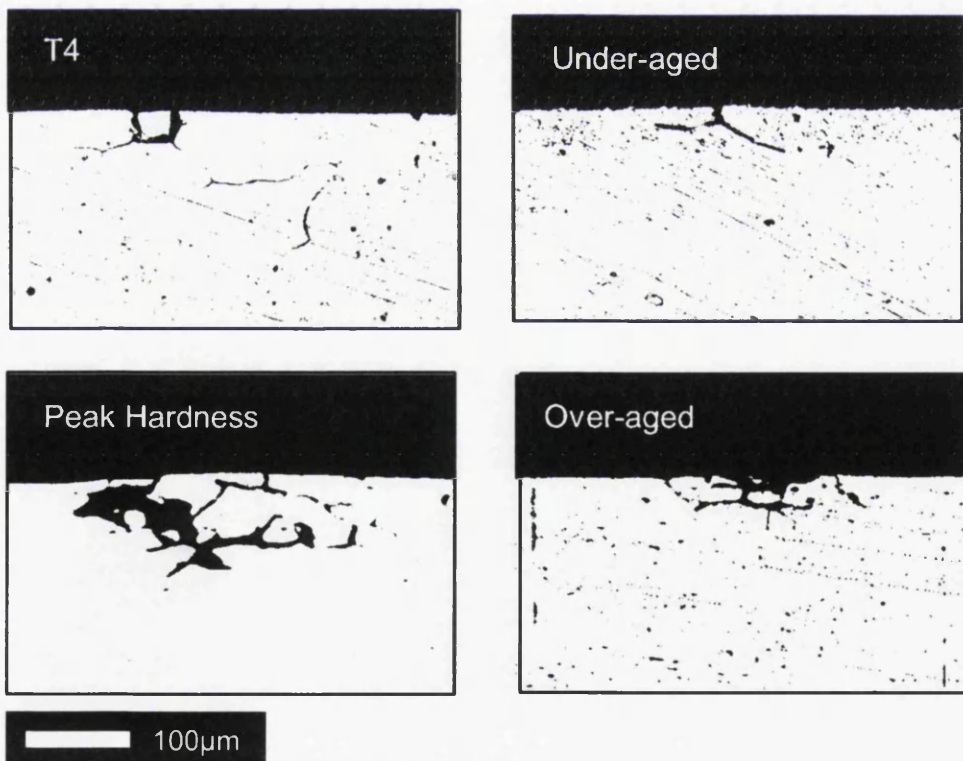


Figure 4.14 Cross sectional optical micrographs of AA6111 in the T4 (no artificial ageing), underaged (0.57h @ 185°C), peak aged (5.56h @ 185°C) and overaged (55.56h @ 185°C) conditions after 24h immersion in 1% w/w aqueous NaCl solution.

Shallow, smooth pits as shown in Figure 4.13 were present on samples in all ageing conditions in addition to the deeper intergranular pits in Figure 4.14. In some cases the intermetallic particle can be seen within the pit, presumably they are cathodic relative to the matrix and are therefore causing the anodic dissolution of the adjacent aluminium. This is shown schematically in Figure 4.15.

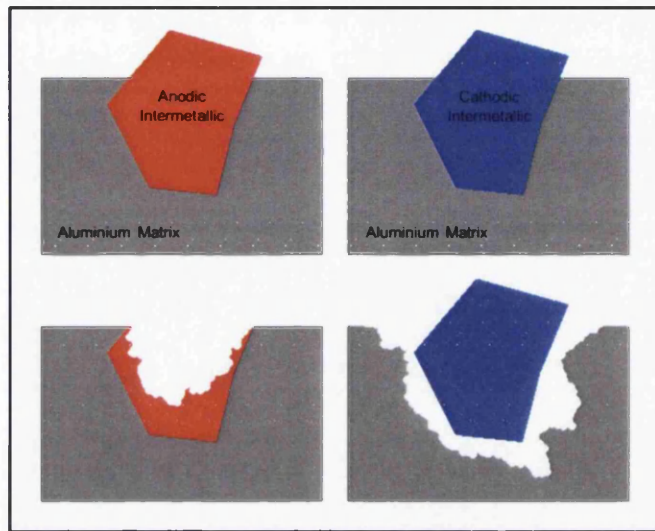


Figure 4.15 Schematic showing pitting resulting from the presence of anodic and cathodic intermetallic particles on the surface of an aluminium alloy.

In Aluminium alloys pit initiation begins by the breakdown of the passive oxide film. Pitting is influenced by intermetallic particles which exhibit different surface film characteristics to the matrix and may be relatively anodic or cathodic. Anodic particles may be dissolved leaving the matrix intact. Where there are cathodic particles, localised galvanic attack can occur around them because the aluminium matrix surrounding the particle becomes the anode.

In AA6111 the major precipitates are Q phase and β phase which can exhibit more complex behaviour; Q phase is initially anodic relative to the aluminium matrix but selective dissolution of magnesium results in precipitates switching to cathodic behaviour. β phase intermetallics tend not to take part in electrochemical or microgalvanic processes because selective dissolution of magnesium results in the formation of an insulating SiO_2 layer.

4.4 Conclusions

The hardness of the AA6111 alloy used in this work was 83HV1 in the as-received T4 condition. Heat treatment of AA6111 at 185°C leads to gradual age hardening. For this heat treatment temperature, peak hardness is achieved after approximately 5.5 hours. Further heat treatment leads to overageing and a very gradual decrease in hardness.

Immersion of AA6111 in an aqueous 1% sodium chloride solution results in pitting corrosion. This occurs when the material is in the T4 condition and for heat treatments of between 0.17 hours and 56 hours at 185°C. The appearance of corrosion product on corroded AA6111 samples matched well with areas of anodic activity shown by the SVET maps.

Analysis of the SVET output indicates that the anodic current density measurements are robust. The presence of a uniform offset introduces more error in cathodic than anodic current density measurements. Total anodic charge was calculated by the integration of anodic current density data with respect to both time and area, the application of Faraday's law allowed the total equivalent aluminium mass loss during each 24 hour SVET experiment to be estimated.

Calculated total equivalent aluminium loss values showed AA6111 to be relatively resistant to localised corrosion in the T4 temper. Susceptibility increased as a result of heat treatment for up to one hour at 185°C but did not increase further as a result of longer heat treatment. The lack of sites for oxygen reduction on the surface of AA6111 in the T4 condition is proposed to be the reason for its relative resistance to corrosion. The copper present in this alloy is likely to precipitate as copper rich particles when heat treated which increases the availability of sites for the cathodic process of oxygen reduction and thus the rate of localised corrosion increases (assuming the corrosion rate to be controlled by the mass transport of oxygen in this case). If, after approximately one hour of heat treatment at 185°C the distance between copper particles is less than the thickness of the Nernst diffusion layer, then further precipitation of copper rich precipitates will not increase the

corrosion rate. It is proposed that increasing the heat treatment time, which may increase the number of copper rich precipitates on the surface, does not increase the corrosion rate further because the diffusion pathways of oxygen through the Nernst diffusion layer are not significantly changed.

Because the SVET data is resolved in terms of both time and area, detailed analysis of the current density history of individual anodes could be carried out. It was shown that current densities at the centre of the most significant anodes of underaged AA6111 tend to reach their peak within 7 hours of immersion in the electrolyte. From peak ageing onwards the peak current densities for the individual anodes tend to be higher and more evenly spaced throughout the 24 hour experiment. The anodes which develop on the two most heavily overaged samples develop, peak and recede in succession.

References

- [1] www.world-aluminium.org, Accessed: 28/05/07
- [2] J. R. Davis, 'Corrosion of Aluminium and Aluminium Alloys', (1999)
- [3] G. Scamans, Innoval Technology, Technical summary
- [4] www.gamry.com, Accessed: 22/11/10
- [5] J. E. Hatch, 'Aluminum, Properties and Physical Metallurgy', (1984)
- [6] K. R. Trethewey and J. Chamberlain, 'Corrosion for Science and Engineering', (1995)
- [7] www.alfed.org.uk, Accessed: 06/12/10
- [8] J. L. Murray, Int'l. Met. Rev., 30 (1985) 211
- [9] Aluminium and aluminium alloys. Wrought products. Temper designations, BSI, (1993)
- [10] G. B. Burger, et al., Materials Characterization, 35 (1995) 23
- [11] W. S. Miller, et al., Materials Science and Engineering A, 280 (2000) 37
- [12] O. Engler and J. Hirsch, Materials Science and Engineering A, 336 (2002) 249
- [13] http://www.alufoil.org/upload/media/achenbach_extract.pdf, Accessed: 13/01/11
- [14] T. Inaba, Kobelco Technology Review, (2005)
- [15] K. Shibata, ALUTOPIA, 35 (2005) 9
- [16] G. Svenningsen, et al., Corrosion Science, 48 (2006) 226
- [17] Y. Birol, Materials Science and Engineering, 391 (2005) 175
- [18] L. L. Shreir, 'Corrosion', (1983)
- [19] C. Wagner and W. Traud, Z. Electrochem., 44 (1938) 391
- [20] J. Tafel, Z. Physik. Chem., 50 (1905) 641
- [21] D. A. Porter and K. E. Easterling, 'Phase Transformations in Metals and Alloys', (1988)
- [22] H. Kaesche, 'Localized Corrosion', (1974)
- [23] E. H. Dix, Trans. AIME, 137 (1940) 11
- [24] G. Svenningsen, et al., Corrosion Science, 48 (2006) 1528

- [25] G. Svenningsen, et al., Corrosion Science, 48 (2006) 258
- [26] G. Svenningsen, et al., Corrosion Science, 48 (2006) 3969
- [27] A. Shi, B. A. Shaw and E. Sikora, Corrosion, 61 (2005) 534
- [28] Z. A. Foroulis and M. J. Thubrikar, J. Electrochem. Soc., 122 (1975) 1296
- [29] T. P. Hoar, 'Electrode Processes', (1961)
- [30] C. F. Sharman, Nature, 153 (1944) 621
- [31] A. Afseth, PhD Thesis - 'Metallurgical control of filiform corrosion of aluminium alloys' (1999) Norwegian University of Science and Technology
- [32] A. Bautista, Progress in Organic Coatings, 28 (1996) 49
- [33] R. T. Ruggeri and T. R. Beck, Corrosion, 392 (1983) 452
- [34] G. M. Scamans, et al., Mater. Sci. Forum, 519-521 (2006) 647
- [35] H. Kaesche, Werks. Korros., 11 (1959) 668
- [36] M. Huisert, PhD Thesis - 'Electrochemical characterisation of filiform corrosion on aluminium rolled products' (2001) Delft university of technology
- [37] G. Williams, et al., PhysChemComm, 6 (2001) 1
- [38] G. Williams and H. N. McMurray, 150 (2003) B380
- [39] W. H. Slabaugh, et al., J. Paint. Techn., 44 (1972) 76
- [40] G. M. Hoch, 'Localized Corrosion', (1974)
- [41] H. Leidheiser Jr., Corrosion, 38 (1982) 374
- [42] G. M. Scamans, et al., Proceedings of ASST, (1997) 229
- [43] H. Leth-Olsen, PhD Thesis - NTNU, (1996)
- [44] K. Nisancioglu, 3rd Int. Conf. on Aluminium Alloys, Trondheim, Norway, (1992)
- [45] A. Afseth, et al., Corrosion Science, 44 (2002) 2529
- [46] A. Afseth, et al., Corrosion Science, 44 (2002) 2543
- [47] B. W. Lifka, 'Corrosion of Aluminium and Aluminium Alloys', (1996)
- [48] G. Thomas, J. Inst. Met., 90 (1961) 57
- [49] A. Kelly and R. B. Nicholson, Progress in material science, 10 (1963) 3
- [50] H. K. Hardy and T. J. Heal, Progress in Metal Physics, 5 (1954) 143

- [51] D. J. Chakrabarti and D. E. Laughlin, *Progress in Materials Science*, 49 (2004) 389
- [52] G. A. Edwards, et al., *Acta Materialia*, 46 (1998) 3893
- [53] E. H. Dix, G. F. Sager and B. P. Sager, *Trans. Amer. Inst. Min. Met. Eng.*, 99 (1932) 119
- [54] A. Perovic, et al., *Scripta Materialia*, 41 (1999) 703
- [55] L. Arnberg and B. Aurivillius, *Acta. Chem. Scand.*, 34 (1980) 1
- [56] W. F. Miao and D. E. Laughlin, *Metallurgical and Materials Transactions a-Physical Metallurgy and Materials Science*, 31 (2000) 361
- [57] W. F. Miao and D. E. Laughlin, *Journal of Materials Science Letters*, 19 (2000) 201
- [58] A. Gaber, et al., *Journal of Alloys and Compounds*, 429 (2007) 167
- [59] M. Pourbaix, 'Atlas of Electrochemical Equilibria in Aqueous Solutions', (1974)
- [60] F. Eckermann, et al., *Electrochimica Acta*, 54 (2008) 844
- [61] M. H. Larsen, et al., *Journal of the Electrochemical Society*, 155 (2008) C550
- [62] Corrosion of metals and alloys - Determination of resistance to intergranular corrosion of solution heat-treatable aluminium alloys, B. Standard, BN EN ISO 11846 (2008)
- [63] L.-Z. He, et al., *Corros. Sci. Protect. Technol.*, 16 (2004) 129
- [64] H. P. Godard, et al., 'The Corrosion of Light Metals', (1967)
- [65] K. Yamaguchi and K. Tohma, ICAA6, Tokyo, (1998)
- [66] V. Guillaumin and G. Mankowski, *Corrosion*, 56 (2000) 12
- [67] D. O. Sprowls and R. H. Brown, *Fundamental Aspects of Stress Corrosion Cracking, Ohio*, (1967)
- [68] R. Dif, et al., ICAA6, Tokyo, (1998)
- [69] R. Dif, et al., *Mater. Sci. Forum*, (2000)
- [70] A. K. Bhattamishra and K. Lal, *Z. Metallkd*, 89 (1998) 793
- [71] T. D. Burleigh, E. Ludwiczak and R. A. Petri, *Corrosion*, 51 (1995) 51
- [72] T. D. Burleigh, ICAA3, Trondheim, (1992)
- [73] G. Scamans, Innoval Technology, Technical Paper
- [74] Y. Liu, et al., *Acta Materialia*, 55 (2007) 353

- [75] H. Leth-Olsen, J. H. Nordlien and K. Nisancioglu, Proceedings of the Symposium on Passivity and Its Breakdown, 97 (1998) 584
- [76] A. Afseth, et al., Corrosion Science, 43 (2001) 2093
- [77] M. Fishkis and J. C. Lin, Wear, 206 (1997) 156
- [78] A. Afseth, et al., Corrosion Science, 44 (2002) 2491
- [79] A. Afseth, et al., Corrosion Science, 43 (2001) 2359
- [80] H. Leth-Olsen, J. H. Nordlien and K. Nisancioglu, Corrosion Science, 40 (1998) 2051
- [81] R. Ambat, et al., Journal of the Electrochemical Society, 151 (2004) B53
- [82] Y. Liu, et al., EMAG-NANO 2005: Imaging, Analysis and Fabrication on the Nanoscale, 26 (2006) 103
- [83] Standard guide for testing filiform corrosion resistance of organic coatings on metal, ASTM, (2009)
- [84] Filiform corrosion test of coatings on aluminium, DIN, (1989)
- [85] Corrosion tests in artificial atmospheres, ISO 9227, (2006)
- [86] M. Rohwerder and F. Turcu, Electrochimica Acta, 53 (2007) 290
- [87] H. S. Isaacs, Corrosion, 43 (1987) 594
- [88] H. S. Isaacs and Y. Ishikawa, International Congress on Metallic Corrosion, 2 (1984) 150
- [89] M. Stratmann and H. Streckel, Corrosion Science, 30 (1990) 681
- [90] M. Stratmann and H. Streckel, Corrosion Science, 30 (1990) 697
- [91] G. Grundmeier, W. Schmidt and M. Stratmann, Electrochimica Acta, 45 (2000) 2515
- [92] B. S. Tanem, G. Svenningsen and J. Mårdalen, Corrosion Science, 47 (2005) 1506
- [93] D. A. Little, M. A. Jakab and J. R. Scully, Corrosion, 62 (2006) 300
- [94] O. Schneider, et al., Journal of the Electrochemical Society, 154 (2007) C397
- [95] H. Leth-Olsen and K. Nisancioglu, Corrosion Science, 40 (1998) 1179
- [96] G. M. Scamans, et al., Mater. Sci. Forum, 396-402 (2002) 146
- [97] A. Afseth, et al., Corros. Sci., 43 (2001) 2093
- [98] A. Afseth, et al., Corros. Sci., 44 (2002) 145
- [99] A. Afseth, et al., Corros. Sci., 44 (2002) 2491

- [100] S. M. Hirth, et al., *Materials Science and Engineering a-Structural Materials Properties Microstructure and Processing*, 319 (2001) 452
- [101] H. N. McMurray, et al., *Journal of the Electrochemical Society*, 154 (2007) C339
- [102] H. Leth-Olsen, Phd Thesis - NTNU, (1996)
- [103] G. Svenningsen, et al., *9th International Conference on Aluminium Alloys and their Physical and Mechanical Properties*, (2004) 818
- [104] H. N. McMurray, et al., *Mater. Sci. Forum*, 519-521 (2006) 679
- [105] British Standard, (2004)
- [106] M. Stratmann, *Corrosion*, 61 (2005) 1115
- [107] G. Grundmeier and M. Stratmann, *Annu. Rev. Mater. Res.*, 35 (2005) 571
- [108] H. N. McMurray and G. Williams, *Journal of Applied Physics*, 91 (2002) 1673
- [109] A. Leng, H. Streckel and M. Stratmann, *Corrosion Science*, 41 (1998) 547
- [110] N. Le Bozec, et al., *J. Electrochem. Soc.*, 149 (2002) B403
- [111] N. Le Bozec, D. Persson and D. Thierry, *J. Electrochem. Soc.*, 151 (2004) B440
- [112] W. Schmidt and M. Stratmann, *Corrosion Science*, 40 (1998) 1441
- [113] G. Williams, et al., *PhysChemComm*, 4 (2001) 26
- [114] G. Williams and H. N. McMurray, *Electrochemical and Solid State Letters*, 7 (2004) B13
- [115] H. N. McMurray, G. Williams and S. O'Driscoll, *Journal of the Electrochemical Society*, 151 (2004) B406
- [116] W. H. Slabaugh, *Industrial and Engineering Chemistry*, 46 (1954) 1014
- [117] S. Garcia-Vergara, et al., *J. Electrochem. Soc.*, 151 (2004) B16
- [118] H. N. McMurray, et al., *12th International Conference on Aluminium Alloys, Yokohama*, (2010)
- [119] A. J. Coleman, Phd Thesis - Swansea University, (2007)
- [120] H. N. McMurray, et al., *Electrochimica Acta*, 55 (2010) 7843
- [121] Filiform corrosion test, DIN, 65472 (1989)
- [122] <http://www.tno.nl/werkenbij/>, Accessed: 12/07/10
- [123] J. Guthrie, B. Battat and C. Grethleine, *AMPTIAC Quarterly*, 6 11

[124] G. Williams, A. J. Coleman and H. N. McMurray, *Electrochimica Acta*, 55 (2010) 5947